Structural Investigations of Highly Strictive Materials

Jianjun Yao

Dissertation submitted to the faculty of the Virginia Polytechnic Institute and State University in partial fulfillment of the requirements for the degree of

Doctor of Philosophy

In

Department of Materials Science and Engineering

Dwight Viehland, Committee Chair

Jie-Fang Li

William T. Reynolds

Chenggang Tao

Blacksburg, VA 24061

April 25th 2012

Keywords: lead-free ferroelectics, Fe-Ga alloys, piezoresponse force microscopy, transmission electron microscopy, ferroelectric domain

Structural Investigations of Highly Strictive Materials

Jianjun Yao

ABSTRACT

Ferroelectric (piezoelectric) and ferromagnetic materials have extensively permeated in modern industry. $(Na_{1/2}Bi_{1/2})TiO_3$-$BaTiO_3$ (NBT-x%BT) single crystals and $K_{1/2}Na_{1/2}NbO_3$ (KNN) textured ceramics are top environment-friendly candidates which have potential to replace the commercial lead zirconate titanate or PZT. High magnetostrictive strain (up to 400 ppm) of Fe-xat.%Ga makes this alloys promising alternatives to existing magnetostrictive materials, which commonly either contain costly rare-earth elements or have undesirable mechanical properties for device applications. These systems have common characteristics: compositional/thermal/ electrical dependent structural heterogeneity and chemical disorder on sub-micron or nano scale, resulting in diverse local structures and different physical properties. In this work, I have investigated domain and local structures of NBT-x%BT crystals, KNN ceramics and Fe-xat.%Ga alloys under various conditions, mainly by scanning probe and electron transmission techniques.

In NBT-x%BT single crystals, polarized light, piezo-response force (PFM) and transmission electron (TEM) microscopies were used to study domain structures and oxygen octahedral tiltings. Hierarchical domain structures were found in NBT: a high-temperature tetragonal ferroelastic domain structure is elastically inherited into a lower temperature rhombohedral ferroelectric phase. Nanoscale domain engineering mechanism was found to still work in NBT-x%BT system and a modified phase diagram was proposed based on domain observations. An increased intensity of octahedral in-phase tilted reflections and a decrease in the anti-phase ones was observed, with increasing x as the morphotropic phase boundary (MPB) is approached. It was also found that Mn substituents favor the formation of long range ordered micro-sized ferroelectric domains and octahedral in-phase tilted regions near the MPB. Nano-size heterogeneous regions were observed within submicron domain structure, indicating that the nanoscale polarization dynamics are not confined by domain boundaries, and the high

piezoelectricity of NBT-x%BT is due to a polarization dynamics with high sensitivity to electric field and a broadened relaxation time distribution.

In KNN textured ceramics, an aging effect was found to exist in the orthorhombic single phase field, not only in the orthorhombic and tetragonal two-phase field as previously reported. No variation of phase structure was revealed between before and after aging states. However, pronounced changes in domain morphology were observed by both PFM and TEM: more uniform and finer domain structures were then found with aging. These changes were even more pronounced after poling the aged state. A large number of sub-micron lamellar domains within micron-domains were observed: suggesting a domain origin for improved piezoelectric properties.

In Fe-xat.%Ga alloys, an underlying inhomogeneity from Ga atoms embedded into the α-Fe matrix was believed to be the origin of giant magneostrictive properties. I have systematically investigated the phase structure and nano-size heterogeneity of Fe-xat.%Ga alloys subjected to different thermal treatments using standard TEM and high resolution TEM for $10<x<30$. Nano-precipitates were observed in all specimens studied: A2, $D0_3$ and B2 phases were found depending on x. Nano-precipitates of $D0_3$ were observed to be dominant for compositions near the magnetostriction peaks in the phase diagram. Quenching was found to increase the volume fraction of nanoprecipitates for x=19, near the first magnetostriction peak. With increasing x to 22.5, nanoprecipitates were observed to undergo a $D0_3 \rightarrow$B2 transformation. A high density of $D0_3$ precipitates of nanoscale size was found to be the critical factor for the first maximum in the magnetostriction.

Acknowledgements

I would like to express my sincere gratitude to my advisors, Professor Dwight Viehland and Professor Jiefang Li, for their faith, guidance, and support throughout the course of my doctoral study.

I have tremendous respect for Professor Dwight Viehland for his knowledge, wisdom, and passion for research. He is of unfailing help in navigating my research and I am indebted to him for his guidance in every aspect and step during my doctoral study. When I prepared for papers, proposals and thesis and contacted him to help me get untangled, he responded with patience and an exceedingly sharp pen. All of these help extend beyond language to express here and I deeply appreciate all these invaluable help.

Equally important, Professor Jiefang Li has provided me great help in almost all equipment and facilities setup. She has generously shared her knowledge and experience in experimental techniques. Her profound understanding and solid theory in materials science lead me to a high standard in research habits.

I would like to give my thanks to Professor William Reynolds and Professor Chenggang Tao for serving in my committee and taking time out of their busy schedule to evaluate my work. And thanks for their many valuable discussions and suggestions on my dissertation.

Great thanks should give to Professor Haosu Luo and Dr. Qinghui Zhang for providing lots of high quality NBT-BT single crystals. I also would like to thanks Professor Gary Messing and Dr.Yunfei Chang to send us KNN textured ceramics. Appreciation needs to give to Professor Zhengkui Xu for many suggestions of TEM study on ferroelectric domains. I also need to thank Dr. Sergei Kalinin, Dr. Stephen Jesse, Dr. Yunseok Kim and Dr. Amit Kumar for their giant experimental assistance during my stay at Oak Ridge National Lab.

I want to show my thanks to Professor M. Murayama, Dr. Niven Monsegue, William Wu and John McIntosh for technical support on TEM experiments. Thanks for their training and assistance in the TEM and HRTEM of NCFL at ICTAS, which makes important part in my research.

I especially thank Dr. Hu Cao for x-ray guidance and helping me accomplish my first paper at VT. Many thanks are given to Dr. Wenwei Ge for collaboration on lead-free project and many stimulative discussions. My gratitude also extends to other colleagues and friends including Dr. Feiming Bai, Dr. Zengping Xing, Dr. Junyi Zhai, Dr. Li Yan, Dr. Yaodong Yang, Dr. Yaojin Wang, Dr. Ravi Viswan, Liang Luo, Zhiguang Wang, Junqi Gao, Yanxi Li, Menghui Li, Ying Shen, Chengtao Luo, Tongan Jin, Kewei Xiao, Tyler Horseman, Katia Rodriguez, Chris DeVreugd for their valuable comments and suggestions through discussion and it will be always a good memory to get along with them in the past four years.

Partial financial support from China Scholar Council is sincerely acknowledged.

The most important acknowledgement is saved for my family. I would like to express my gratitude to my parents, Shaoqing Yao and Jianqiong Luo, for their constant faith, encouragement, and support during my doctoral study, to my wife, Le Yang, for her continually support in every detail of my life and giant selfless sacrifice for my work here. I thank my daughter, Vera Yao, who gives me the strength and courage to keep going with my work especially when I feel frustrated and tired. I thank my mother-in-law, Jinhua Zhao, for taking care of my daughter and wife.

Table of Contents

List of Figures

Chapter 1 Introduction

1.1 Development of electro/magneto strictive materials

Electronic and magnetic materials have permeated every aspect of modern industry. For example, the vast amount of data generated by consumer electronics products is often stored as regions of opposite magnetization in ferromagnets (a magnetic field can reverse its spontaneous magnetic polarization).[1] The sensor industry relies heavily on a related class of materials known as ferroelectrics (materials with a spontaneous electric polarization that can be switched by an electric field). Ferroelectrics are also piezoelectric: a change in their electric polarization is accompanied by a change in volume. As a result, they are used to convert sound waves into electrical signals in sonar detectors, and convert electrical signal into motion in actuators.[1] A similarity for both ferromagnets and ferroelectrics is illustrated in Figure 1.1, which is the hysteresis loop.

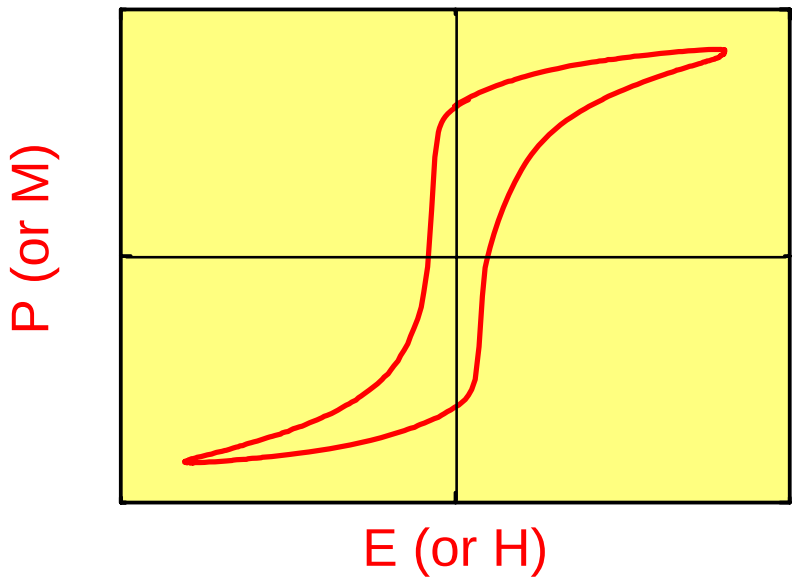

Figure 1.1 Schematic illustration of hysteresis loops for electric/magnetic field induced polarization/magnetization.

1.2 Development of high performance lead-free ferroelectric materials

Individually, ferroelectric (piezoelectric) materials are widely used in modern industry to transform electrical signals to mechanical strain and vice versa. For applications, the piezoelectric strain coefficient and its temperature dependence are the critical performance metrics.

Currently, piezoelectric materials in commercial use are based on lead zirconate titanate or PZT. PZT has superior dielectric and piezoelectric properties near a morphotropic phase boundary (MPB) between tetragonal and rhombohedral phases [2]. Piezoelectric coefficients (d_{33}) of 779 pC/N have been reported for modified PZT [3] with Curie temperatures (T_c) in the range of 300-400 °C. Enhanced properties and high T_c near the MPB enable an excellent thermal stability and allow for operational temperature ranges of up to175 °C. [4]

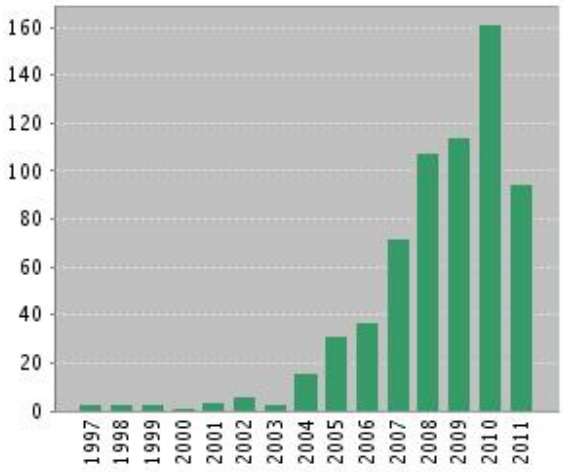

Figure 1.2 Publications on lead-free ferroelectric found in refereed journals.

However, with health and environmental concern arising, the commercial manufacture/applications of PZT would be affected. The development of alternative lead-free piezoelectric materials is becoming increasingly important, in order to reduce environmental contamination by lead-based systems.[4] Figure 1.2 shows the number of published literature found in the "web of science" database using keywords of "lead-free", "ferroelectric" and "piezoelectric". It is readily apparent that the research on lead-free ferroelectrics has dramatically increased since 2004. The goal of developing lead-free materials to replace PZT, requires both

high d_{33} values and good thermal stability. Amongst all the possible candidates, $Na_{0.5}Bi_{0.5}TiO_3$-$BaTiO_3$ (NBT-BT) and $K_{0.5}Na_{0.5}NbO_3$-based (KNN) solid solutions are the most promising.

1.2.1 Development of NBT-BT single crystals and KNN textured ceramics

Traditionally, the enhancement of the electromechanical response in ferroelectrics materials was achieved by compositional modification. Following this approach, the composition is optimized to bring the material into proximity with a structural instability such as the MPB or polymorphic phase boundary (PPB).[5-7] Relatively little temperature dependence of piezoelectric properties and broad usage temperatures are typical features for MPB-based ferroelectrics. However, PPB-based ferroelectrics generally exhibit large temperature dependence of piezoelectric coefficients close to the PPB temperature. Recent major progresses on the development of lead-free materials was the growth of NBT-BT single crystals and the fabrication of high textured KNN ceramics, [8-11] which belong to MPB and PPB-based system, respectively.

NBT-BT single crystals were grown by spontaneous nucleation from slowly cooled oxide melts, formulated to contain an excess of alkaline and bismuth oxide as the flux. The piezoelectric constant d_{33} of NBT-BT single crystals has been reported to be as high as 280 pC/N.[12] Later, Mn-modified NBT-BT single crystals were grown by top-seeded solution growth (TSSG), which exhibited superior piezoelectric and ferroelectric properties of d_{33} as high as 483 pC/N, close to the widely used PZT ceramics. [11]

Beside NBT-BT crystals, the other important family is KNN system, first reported by the Toyota Central Research Laboratory in 2004.[8] Li, Ta, and Sb modified KNN have values of d_{33}=416 pC/N, which is comparable to that of PZT near room temperature. This report triggered many subsequent activities in search of high lead-free piezoelectrics: through compositional modifications and shifting of the PPB.

However, no work of KNN after that achieved the same high value of d_{33} as reported: generally below 250 pC/N. Although single crystals of KNN are expected to own better properties compared to their ceramics counterparts, the effort to grow high quality KNN single crystals has failed due to inevitable cracks formed during the growth process. <001>-textured KNN-based ferroelectric ceramics by templated grain growth (TGG) displays enhanced and

repeatable piezoelectric properties.[14] The <001>-oriented KNN ceramics with a narrow orientation distribution were produced by TGG using $NaNbO_3$ templates. Excellent electromechanical properties were obtained from -70 °C to the PPB at 160 °C. Textured KNN ceramics show very high electromechanical coupling factors k_p=0.64 and k_{31}=0.37, high value of d_{33}=208-218 pC/N, and modest strain hysteresis 6.3% near room temperature. [14]

1.2.2 Origin of strong ferroelectricity in Pb-based solid solutions

The structure of extensively studied ferroelectric materials (both lead and lead-free based) is perovskite, having a general formula of ABO_3, where A represents a divalent or trivalent cation and B is typically a tetravalent or trivalent cation. A ions occupy the corner of the cube, while B ions sit on the body center positions inside an oxygen octahedron, which are at the face center positions. B-site ions can move relative freely inside the oxygen octahedron with relative small restoring force.[15] The images in Figure 1.3 illustrate the unit cell of the perovskite structure (PZT) with two different states.[16] When the temperature is above the Curie temperature, the unit cell is cubic, and the B cation (Ti^{4+}/ Zr^{4+}) locates at the center, and A cations (Pb^{2+}) site at the face center positions. When below the Curie temperature, the unit cell distorts. For PZT, the structure would change into tetragonal, where the B cation (Ti^{4+} or Zr^{4+}) moves along the {100} direction and the O^{2-} moves in the opposite direction: a spontaneous polarization then forms as a consequence. Recent progress on high resolution TEM enables to observe such displacements.[17] The following lattice image in Figure 1.4 was obtained by the abbration corrected HRTEM, which shows the small displacement of the PZT lattice.

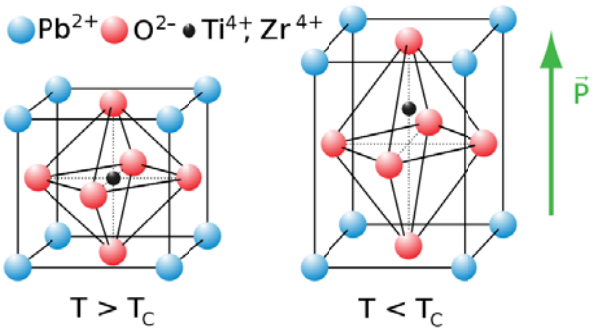

Figure 1.3 Unit cell of perovskite oxide (PZT) above and below Curie temperature.[16]

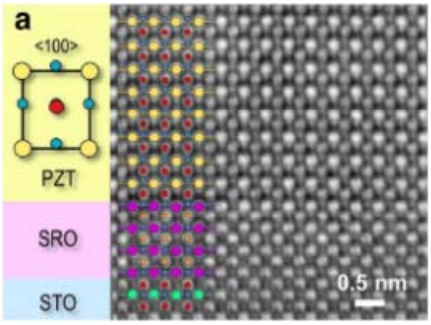

Figure 1.4 (a) Direct observation of the displacement of Ti^{4+}/ Zr^{4+} cation by aberration corrector HRTEM. Reprint with permission from [17]. Copyright [2010], American Physical Society.

For ferroelectric materials, while spontaneous polarization exists, the macro-polarization is zero due to the offset of individual spontaneous polarization regions of unordered dipole moments: commonly known as domains. Consequently, samples must be poled by a strong electric field to exhibit macro-polarization and piezoelectricity. There are three important points which help us understand the electric-field induced high strain in lead-based system: (i) polarization rotation path under an electric field, emphasized by Fu and Cohen,[18] which has revealed large shape changes. (ii) experimental discovery of a monoclinic phase in PZT [6] close to the MPB, which is a nearly vertical boundary between rhombohedral and tetragonal phases. (iii) domain engineered states with intense nano-domain structures observed near the MPB.[19]

Take PZN-8%PT for example, which has a rhombohedral structure with a polarization along the <111> direction. When an electric field is applied along <001>, it responds mechanically in three steps as shown in Figure 1.5 (marked as A, B and C).[20] Steps A and B are featured by a pronounced increase of strain under a small field. Step C has a very flat strain & field slope, with almost no hysteresis. PZN-PT at step C is determined to have an average tetragonal symmetry.[20] The two most likely explanations for the giant piezoelectric response are: (i) reorientation of polar nano-domains by an applied field; and (ii) polarization rotation associated with phase transitions, in which the large response does not depend in an essential way on the mesoscopic structure or ordering.[18] The proposed polarization rotation paths are illustrated in Figure 1.6.

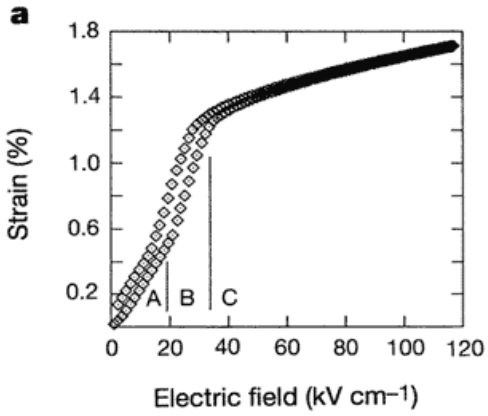

Figure 1.5 Strain responses under electric field for PZN–8%PT. Reprint with permission from [20]. Copyright [1997], American Institute of Physics.

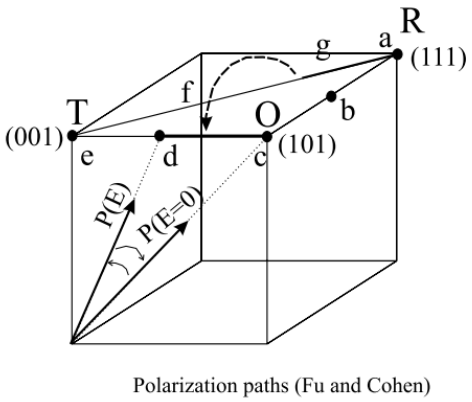

Figure 1.6 The polarization path from [111] in the R phase to [001] in the T phase. Reprint with permission from [18], Copyright [2000], Nature Publishing Group.

It has been reported that the high electromechanical properties of PMN-*x*%PT and PZN-*x*%PT is due to a rhombohedral (*R*)→tetragonal(*T*) phase transition induced by an applied electric field (*E*).[21] The discovery of ferroelectric monoclinic (*M*) phases bridging the *R* and *T* ones, which was firstly reported for $Pb(Zr_xTi_{1-x})O_3$, was an important breakthrough in understanding the structural origin of high electromechanical properties of MPB compositions.[6] A typical phase diagram of PMN is shown in Figure 1.7, which has *M* phase sandwiched by *T* and *R* ones. The monoclinic symmetry allows the polarization vector to be unconstrained within a plane, rather than constricted to a particular crystallographic axis as for higher symmetry *R, T*,

or orthorhombic (*O*) phases. More explicitly, it is the strong interaction between the lattice dynamics and the acoustic phonons that cause the instability of ferroelectric monoclinic phases.[22]

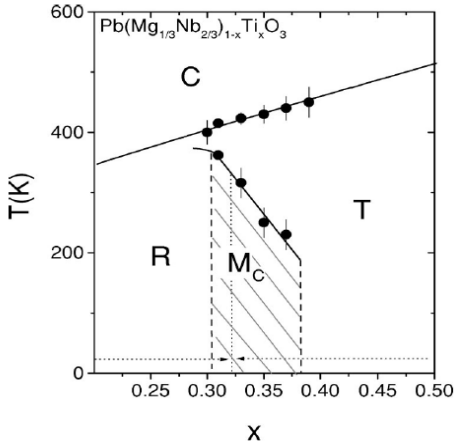

Figure 1.7 The phase diagram of PMN, the monoclinic phase is bridging the R phase and T phase. Reprint with permission from [22]. Copyright [2002], American Physical Society.

The domain structure where a region within which the spontaneous polarization is constant has a close relationship with ferroelectric properties and phase structure. Fingerprint-like ferroelectric domains in PMN-x%PT crystals were oriented along {110} for both PMN-30%PT and PMN-35%PT (see Figure 1.8), both of which have higher piezoelectric properties than other compositions. It is thought that such type of domains is assembled from finer scale polar structures—there is an additional lower end of the hierarchal scale. Thus, the domain hierarchy cannot be completely adjusted at each length scale in an independent manner, i.e., polarization compensation and stress accommodation occurs at all stages of the hierarchy, and not at separate length scales independent of the other.[19] It is also observed that the fingerprint-like domains in PMN-*x*%PT crystals were very thin—the hierarchy consists of an extremely high domain wall density. In particular, the density of fingerprints was extreme high near the MPB: at lower PT contents domain irregularities dominated the morphology and at higher PT contents fingerprints did not form.[15] The formation of nanodomain morphology was considered to result from the reduction of the domain wall energy owing to the vanish of the polar anisotropy, which ultimately induces enhanced piezoelectric properties.

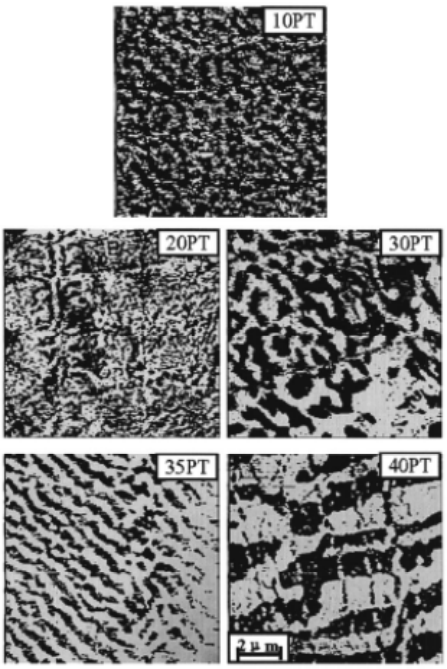

Figure 1.8 PFM images of ferroelectric domains in PMN-x%PT. Reprint with permission from [19]. Copyright [2004], American Institute of Physics.

Stress-accommodating domain structures are observed for any displacive transformation, which can form a domain-averaged transformation strain. The presence of polarization in structural domains will result in a formation of a head-to-tail pattern of the 90° ferroelectric domains.[15] It does not generate spatial charges and thus automatically provides electrostatic energy minimization. For very low values of domain-wall energies, the system transforms into a mixed (or adaptive) state.[7] This adaptive state is inhomogeneous on the nanoscale and homogeneous on the macroscale. The nanoscale microstructure of this adaptive state is a miniaturized microdomain structure determined by the accommodation of the misfit-generated stress and electric field. The changes in the microdomain topology result in gradual average symmetry adaptations.[7,15]

1.2.3 Prior structural investigations of NBT-BT system and KNN ceramics

Since the discovery of NBT, many of its characteristics, particularly dielectric properties and structural phase transitions, have been studied [24-27]. $Na_{1/2}Bi_{1/2}TiO_3$-xat.%$BaTiO_3$ solid

solution (NBT-x%BT) is a very complex system which has a MPB for 5.5<x<6.5. The MPB is a temperature independent boundary between rhombohedral (R) and tetragonal (T) FE phases. Studies have shown that the NBT-based solid solution is a Pb-free FE that has a MPB, which is beneficial for piezoelectrics that need to operate over a wide temperature range.[28]

NBT has been reported to belong to the polar *R3c* space group at room temperature [24]. It is reported that NBT undergoes a phase transition sequence of high-temperature cubic (*C*) → paraelectric tetragonal (*T*) → FE rhombohedral (*R*) at temperatures of 520ºC and 250ºC, respectively [29-33]. The T phase is ferroelastic, and there is no characteristic dielectric anomaly at the *C* → *T* transition [26,34]. Controversy remains concerning the *T* → *R* transition. Neutron scattering and high-resolution synchrotron x-ray diffraction (XRD) have indicated a relatively wide transition range over which *T* and *R* phases coexist [29,31], whereas TEM investigations of powder samples evidenced an intermediate modulated orthorhombic (O) phase that lies between the R and T phases in the temperature range between 230^{o}C and 300^{o}C [26].

Interestingly, no distinct structural changes associated with the ferroelectric transformation have been reported at the maximum in the dielectric constant T_{max} = 330°C.[26] It would thus appear that the high temperature (paraelectric) prototypic phase of NBT has T symmetry, rather than cubic. Ferroelastic domains and a splitting of the lattice parameters have been reported to persist on heating until near 520°C, indicating that this high temperature paraelectric tetragonal phase is ferroelastic. Below T_{max}, the tetragonal phase becomes polar, where it has been reported to have double P-E hysteresis loops. Furthermore, the ferroelectric *T*→*R* transition is diffused, as evidenced by temperature dependent dielectric constant measurements. An inflection in the dielectric constant near 250°C has been assumed to be that of the *T*→*R* transition, below which relaxor ferroelectric characteristics became evident in the dielectric constant on further cooling. Vakhrushev et al. have conjectured that ferroelectric rhombohedral clusters gradually form within the polar tetragonal matrix over a broad temperature range on cooling between 330 and 200°C.[30]

An essential feature of all ferroelectrics is a polydomain structure. The formation of micrometric domains in NBT has been attributed to a deformation of the lattice along the [111], which corresponds to the direction of the Bi shifting that produces a spontaneous polarization.[28] Investigations of the domain structure of NBT and NBT-x%BT have previously been performed by TEM.[25-27] For NBT ceramics, different types of domains have been observed: lamellar,

needle-shaped or crosshatched shaped patterns. However, the findings do not help to explain the relaxor-like characteristics in the R phase, as relaxors are characterized by polar nanodomains and the lack of normal long-range ferroelectric order. However, domains were not observed by TEM for x=3 and 8 [25]: which might be due to electron beam effects.

Within NBT, the oxygen octahedra are anti-phase tilted which can be observed in the 1/2(ooo) reflections (o represents odd). Furthermore, in the rhombohedral R3c phase, tetragonal platelets on the nanoscale have been reported [35], as shown in Figure 1.9. It is believed that these small amount of tetragonal platelets originated from in-phase oxygen octahedra tilts are the reason for 1/2 (ooe) reflections (where e presents even). Temperature dependent TEM studies found that the 1/2(ooo) reflections still can be found at 600°C, similar phenomenon also was observed in NBT-3%BT and NBT-8%BT.

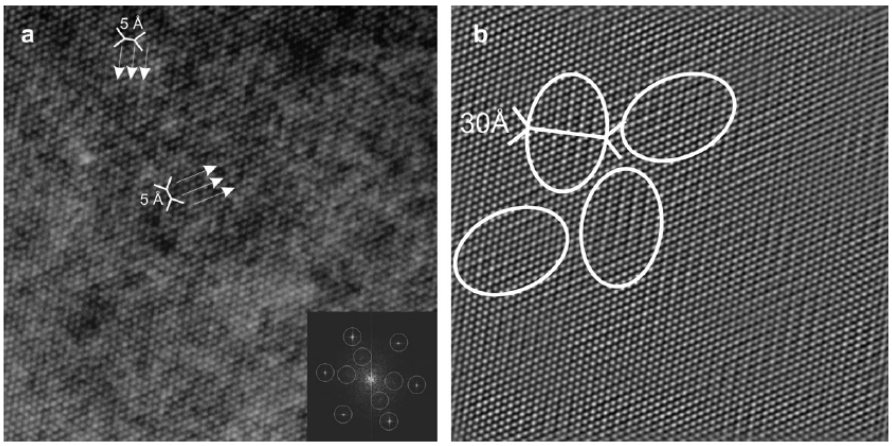

Figure 1.9 (a) HRTEM lattice image of NBT obtained along {111} direction, the claimed tetragonal nano-plates in NBT. Reprint with permission from [35]. Copyright [2008], Elsevier.

$KNbO_3$ and $NaNbO_3$ form a complete solid solution of $K_{1-x}Na_xNbO_3$ (KNN) over the entire range of $0 < x < 1$. Both $KNbO_3$ and $NaNbO_3$ solid solutions are orthorhombic at room temperature and early work on the ceramics in this system indicated multiple temperature-induced phase transformations and MPB comprising a rather complex phase diagram.[4,36,37] Since high performance ceramics KNN were first reported by the Toyota Central Research Laboratory in 2004,[4] which triggered many subsequent activities in search of lead-free alternative piezoelectrics: through compositional modifications and shifting of the PPB. The PPB

is a boundary which is between tetragonal (T) $\xrightarrow{\sim 210^{\circ}C}$ orthorhombic (O).[9] It is expected that a significant increase of the piezoelectric coefficients in <001> textured KNN ceramics, compared to randomly oriented ceramics, is due to an enhanced ordering of the distribution of grain orientations along <001>. Polar vectors of the orthorhombic phase of KNN lie along the <011> direction, and are thus able to achieve domain engineered configurations in <001> textured ceramics. Domain engineered states allow for improved piezoelectric responses in Pb-based systems due to a polarization rotation.[6,18,20]

Recently, x-ray studies of textured Li doped $(K_{0.5}Na_{0.5})NbO_3$ ceramics have revealed a phase coexistence near the PPB over a 30°C temperature range, where the relative phase volume fractions change with temperature. Furthermore, increasing electric field applied along the [001] texture direction results in a notable increase in the *T* phase volume fraction, effectively shifting the *O* → *T* boundary to lower temperatures. The piezoelectric properties are then increased with *T* volume fraction.[39]

The structure of KNN has been reported to be dependent on stoichiometry. At room temperature, an orthorhombic phase is believed to be the ground state,[8,9] but is not the only structure that has been reported.[40-43] Monoclinic and tetragonal structures have also been reported for compositions near the boundary at x=0.5.[40-43] However, for <001> textured KNN ceramics we own, x-ray investigations have shown a single orthorhombic phase field.[10,39] In MPB systems, nanodomains are believed to contribute to the high piezoelectric property of Pb-based perovskites.[19] However, whether a nanodomain mechanism is possible in KNN is not yet clear. Coexisting *O* and *T* structures with fine domain structures of widths on the order of 20–50 nm have been reported, where domain walls intersect at 90° and where nano-domains also exist adjacent to sub-micron domains having 45° intersections,[42] as shown in Figure 1.10. More recently, it was shown that domain morphologies of KNN can vary with stoichiometry and sintering conditions: between featureless, stripe-like and fine irregular structures.[44]

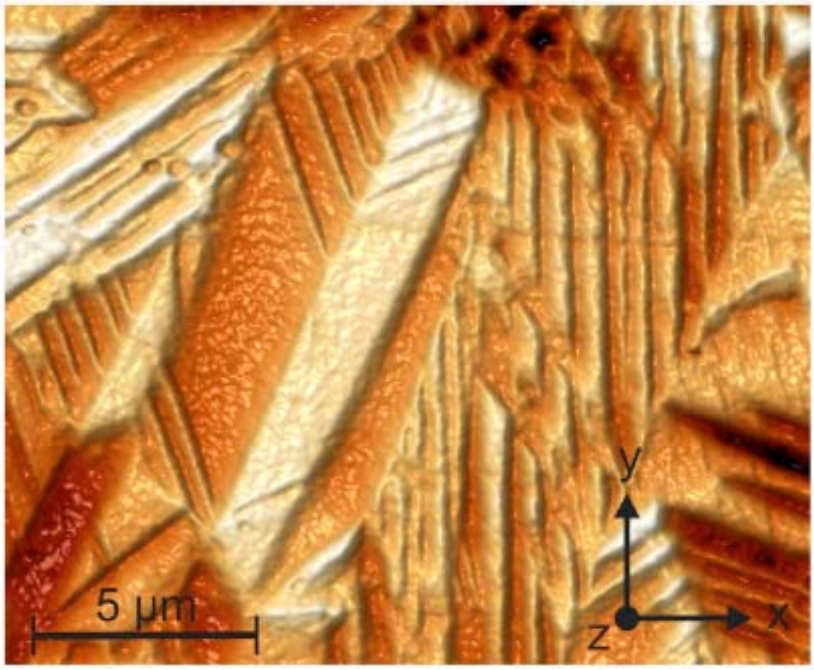

Figure 1.10 Domain structures in *T* and *O* coexisting phases revealed by PFM. Reprint with permission from [42]. Copyright [2007], American Institute of Physics.

Owning to the sensitivity of KNN's domain morphology on thermal treatment, aging has been exploited as a means to improve its piezoelectric properties. [41] A defect migration model has been proposed to explain the origin of such aging.[45] This model was based on x-ray diffraction data, revealed apparent changes in the crystallographic orientations related to a 90° domain switching between before and after the aging and re-poling process. The process was described as an aging-assisted switching of the tetragonal 90° domains, illustrated in Figure 1.11.

It was proposed that aging was effective in improving piezoelectric properties of compositions that had coexisting *O* and *T* phases.[41] However, enhanced field induced domain switching in single *T* phase $BaTiO_3$ crystals after aging has been reported[45]. A symmetry-conforming property of a defect migration model has been proposed to provide a restoring force for reversible domain switching, and consequently a large recoverable electrically-induced strain.[45] Therefore, whether aging was effective in improving the piezoelectric properties of single *O* phase field KNN is not clear. In addition, details concerning defects and their interaction with domain structures, simultaneously with aging and repoling, remains to be experimentally established.

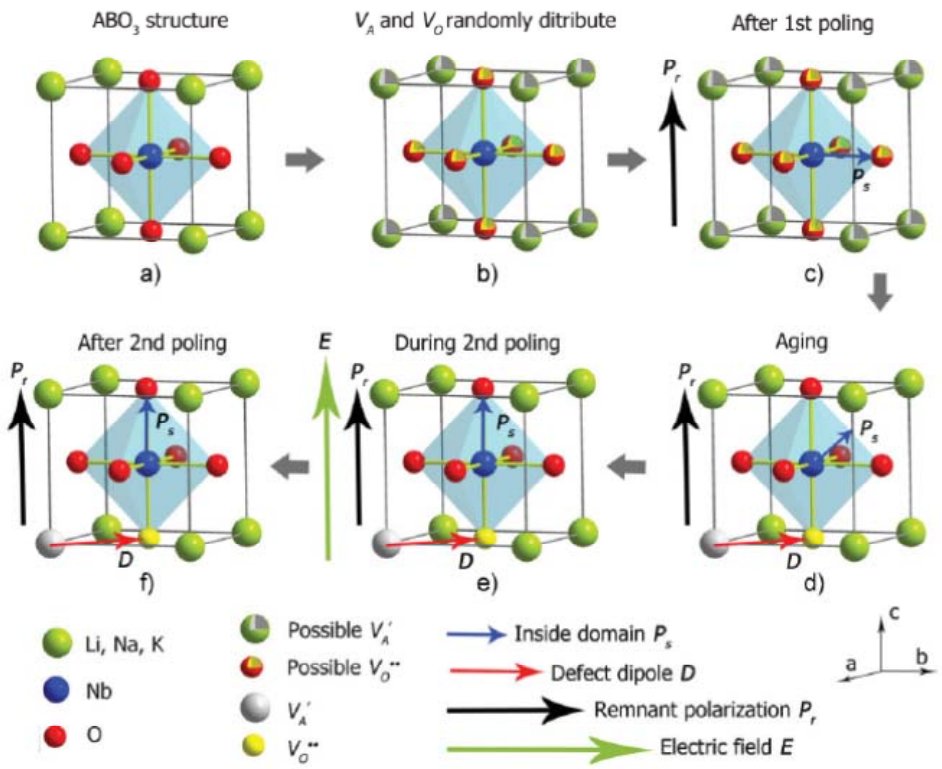

Figure 1.11 Schematic illustration for the aging-induced spontaneous polarization change in Li-modified KNN ceramics. Reprint with permission from [41]. Copyright [2010], John Wiley and Sons.

1.3 High performance ferromagnetic material

Giant magnetostriction in Fe-x%Ga alloys offers potential for sensors and actuators. A maximum in the magnetostrictive strain of 400 ppm was reported for x=19.[46] Meanwhile good performance in ductility, mechanical strength, imposed blocking stress and weak field properties at moderate saturation fields makes them of interest as candidates for micro- or nano-sensors and actuators.

1.3.1 Origin of magnetostriction

Magnetostriction is the feature of ferromagnetic materials that changes their volume during the application of a magnetic field. The variation of magnetization with the applied magnetic field changes the magnetostrictive strain until reaching its saturation value (λ_{100}). From a

structural view point, local structures of Fe-x%Ga can be divided into domains, each of which is a region of limited spatial extent of spontaneous alignment of magnetic moments. Similar to ferroelectric domains, these magnetic domains are randomly oriented with respect to each other among on various directions, resulting in an overall magnetization equal to zero. However, upon application of magnetic field, magnetic domains can be reoriented along the direction of the field, giving rise to a magnetic hysteresis loop.

It is known that pure Fe has limited magnetostriction, which increases notably with increasing x.[47] The origin of enhanced magnetostriction in Fe-x%Ga is unclear, in spite of the significant efforts have been made. Both equilibrium and metastable phase diagrams for Fe-*x*% Ga have been reported.[48,49] In the equilibrium diagram, a disordered body-centered-cubic (bcc)-Fe or A2 phase is in equilibrium with a face-centered-cubic (fcc) *L*12 ordered one; whereas in the metastable diagram, the A2 phase is in a metastable equilibrium with a bcc $D0_3$ ordered phase.[49] The unit structure of A2, D03 and B2 are illustrated in the Figure 1.12.

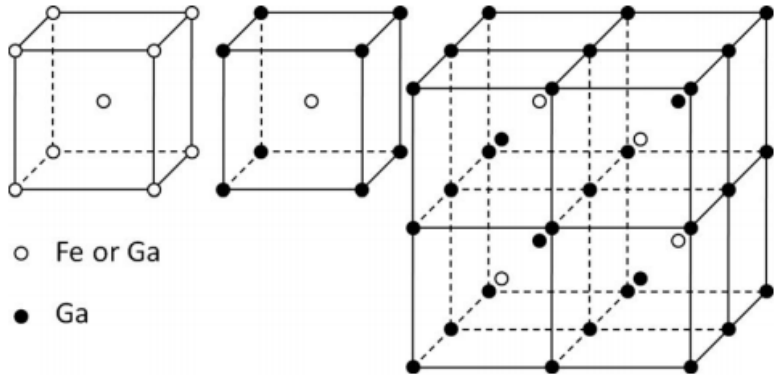

Fig.1.12 Unit cell of A2, B2, and D03 respectively. Reprint with permission from [50]. Copyright [2010], American Physical Society.

Until now, much effort has attempted to explain the origin of this enhanced magnetostriction (λ_{100}) of Fe-x%Ga: in particular, two maximum values in λ_{100} are known near x≈19-20 and x≈28-29. Several models have been proposed to explain this enhanced magnetostriction.[51-54] In spite of differences between the individual proposed mechanisms with respect each other, all of them have a common conceptual basis: that is an underlying heterogeneity. To date, the compositional dependent heterogeneity is still not well understood.

One model proposes that a directional short-range ordering of Ga atoms strains the bcc lattice of α-Fe (or A2) along the [100] direction.[54] Clusters act as locally distorted anisotropic defects that form in the solute, which can change their orientations under application of magnetic (H) and/or stress (σ) fields. Wu et al. [53] suggested that the enhanced magnetostriction was affiliated with a local ordering of Ga atoms: where the B2 structure accompanying Ga pairing contributed a positive effect, whereas the $D0_3$ structure contributed negatively. Later, Khachaturyan and Viehland [51,52] proposed that the enhanced magnetostriction originated from a reorientation of tetragonally distorted $D0_3$ nanoclusters within a A2 matrix. This model was based on the assumption that the slow-cooled Fe-x%Ga alloys are in a structurally and chemically heterogeneous state, consisting of a coarsening-resistant nanodispersion of a $D0_3$ phase within an A2 matrix that formed due to coherency lifting by excess vacancies. A coarsening-resistant nanodispersion is known for chemically similar Fe-x%Al and other alloys.[55]

1.3.2 Composition and thermal treatment dependent magnetostriction in Fe-Ga alloys

It has been established that the phase stability and magnetostrictive properties of Fe-x%Ga are significantly dependent on the thermal treatment history,[47] varying with annealing time, temperature, and cooling rate. This indicates that the enhanced magnetostriction is not an intrinsic property of the lattice, but rather might be due to an underlying inhomogeneity. The variation of magnetostriction with heat treatment and composition is concluded as follows:

(i) For $17.9<x<20.6$, the strain monotonically increases, reaching a maximum at a composition that significantly depends on thermal history for alloys: in slow-cooled conditions 10 °C/ min from (1000 °C), the first maximum occurs at 320 ppm and x=18, whereas, in quenched conditions, the maximum occurs at 390 ppm and 20.6 at.% Ga [48,49].

(ii) Between 17.9–20.6 at.% and 22.5 at.% Ga, the strain decreases, dropping down to 250 ppm at x=25.[48]

(iii) For $22.5<x<28.5$, the magnetostriction increases again, climbing to 380 ppm for slowcooled alloys and 440 ppm for quenched alloys for x=28.5.[48]

(iv) For compositions $x>28.5$, the strain decreases dramatically with increasing x. [48,49,56].

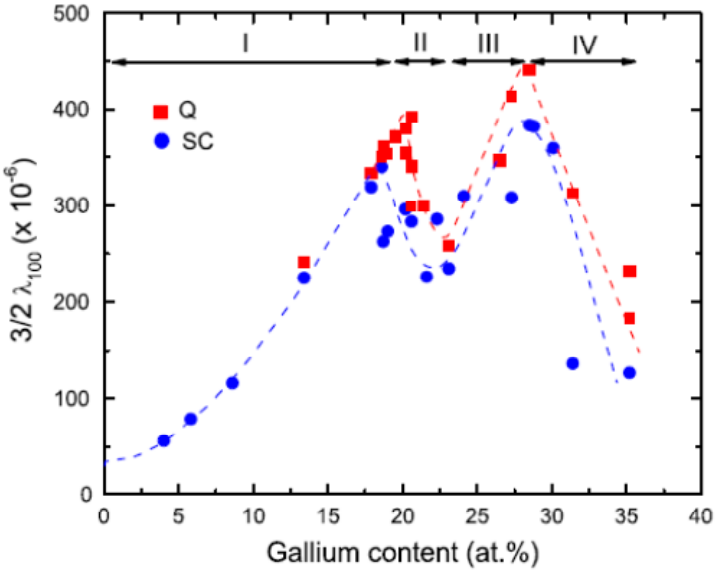

Figure 1.13 Saturation magnetostriction in [001] direction of Fe-Ga alloys as a function of Ga concentration and different thermal treatment. Q represents quenching, SC slow cooling at 10°C/min from 1000°C. Reprint with permission from [47]. Copyright [2008], Elsevier.

1.3.3 Prior structural investigations of Fe-Ga alloys

In order to get insights into the local structures of Fe-x%Ga, X-ray diffraction (XRD), neutron diffraction, transmission electron microscopy (TEM) and other techniques have been used to examine the Ga ordering and determine its length scale.[47,57,58] The dependence of the magnetostriction on phase stability was studied by Xing et al.[47], based on structural analyses by TEM and high-energy transmission XRD: where it was proposed that the A2 phase can account for the enhanced magnetostriction with increasing Ga in either the slow-cooled or quenched alloys. A phase mixture of (A2 + $D0_3$) was then suggested to lead to a quick drop in the magnetostriction with further increasing x, near the first maximum in λ_{100}. However, some discrepancies became apparent on subsequent investigations.[50] For instance, a single-phase A2 region was found on slow-cooled alloys for x<18, which was inconsistent with a transmission synchrotron diffraction study in this range where $D0_3$-type short range ordered (SRO) clusters were reported.[50] In addition, a structural ordering study using Mössbauer spectroscopy revealed the presence of a nearly random distribution of local Fe environments, with a small amount of short-range Ga-Ga pairing with increasing Ga content. This suggests the presence of

at least short-range $D0_3$ type ordering for x<20.[59] In addition, small $D0_3$ regions within an A2 matrix have been reported for x=19/20 Ga by TEM, which were about 30–80 nm in size.[3] For x=22, these $D0_3$ regions coarsened to sizes of 400 nm upon thermal annealing. The size observed for these precipitates (>40nm) differs with that subsequently found by HRTEM, where nanodispersed precipitates consisting of fragments 2-5nm in size were found to orient along <001> directions [16], as shown in Figure 1.14.

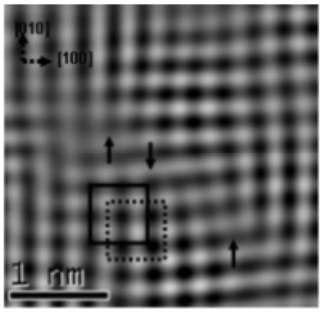

Figure 1.14 Nano-sized D03-like precipitates revealed by HRTEM. Reprint with permission from [50]. Copyright [2008], American Physical Society.

In spite of an inconsistency in $D0_3$ precipitate size, the various investigations support the proposition of a nano-size structurally heterogeneous $D0_3$ phase dispersed within an A2 matrix. There is also some evidence that a magnetic field-induced rotation of the structurally distorted $D0_3$ nano-precipitates contributes to the enhanced magnetostriction: as predicted by Khachaturyan and Viehland.[51,52] Neutron diffuse scattering suggested that the structure of the $D0_3$ nanoprecipitates within the A2 matrix may be distorted from cubic symmetry, as indicated by an asymmetric (300) peak for x=0.19.[57] Furthermore, small-angle neutron scattering has subsequently shown nano-size magnetic heterogeneities in the $D0_3$ phase which are distinct from the matrix, where the moments in and around the heterogeneities reorient under magnetic field or mechanical stress.[60]

From the introduction, it can be seen that there remain a lot of unanswered questions associated with the enhanced piezoelectricity in the NBT-x%BT system in the vicinity of the MPB. Near the MPB of PMN-x%PT and PZN-x%PT crystals, E-field induced ferroelectric phase transitions, polarization rotations via monoclinic phases and domain engineered states with nano-domains have been used to explain such piezoelectric enhancements. Till now, the

information about NBT-x%BT system is scarce. In particular, recent evidence exists of a very weak monoclinicity for NBT,[61,62] suggesting that it may not have a strong correlation between polarization rotation in a monoclinic distorted structure and enhanced piezoelectricity. Thus, the mechanism of enhanced piezoelectricity in MPB compositions of NBT-x%BT remains in question. An alternative model of an electric field induced nonpolar (or pseudocubic) to ferroelectric transition was proposed to explain a giant strain observed near the MPB for NBT-x%BT.[63-65] To date, a detailed understanding of the local nonpolar structure is unclear, especially its evolution with compositions approaching the MPB. Therefore, systematic studies of the complex structural evolution with x would help to evaluate the structure-property relations and to identify the mechanism of enhancement near the MPB. Whether the mechanism of domain engineered states with nano-domains still is effective in NBT-x%BT is still not clear. In addition, Mn substitution increases piezoelectric properties. However, the effect of such substitution on the local structure is unknown. As a ferroelectric relaxor, the dynamic domain behavior and nucleation-growth mechanism during polarization reversal are key issues which also remain unknown for NBT-x%BT.

The KNN system is known to have an unique aging effect, which has been utilized to improve its piezoelectric properties.[41] A defect migration model has been proposed to explain the origin of aging.[45] This model was based on x-ray diffraction data of KNN ceramics, which underwent different thermal treatments. In addition, an aging and re-poling induced enhancement of the piezoelectric properties has been reported for KNN compositions with coexisting orthorhombic (*O*) and tetragonal (*T*) phases.[41] However, micro-structural studies concerning domain evolution associated with aging and repoling have not yet been reported. Aging has been proven to be effective in enhancing field induced domain switching in single T phase $BaTiO_3$ crystals,[45] via a defect symmetry conforming principle. However, such property enhancements due to aging have not yet been reported for single orthorhombic phase field of KNN.

The composition dependent phase structures of Fe-x%Ga alloys have not yet been well sorted out by TEM, even though there have been numerous prior investigations. This has caused confusion with regards to understanding the relationship between enhanced magnetostriction and phase composition.[47] Detailed changes in the morphology of the $D0_3$-like precipitates with thermal treatment and composition need to be examined. Recent theoretical calculations have predicted that an optimum nano-size and volume fraction of precipitates guarantees preservation

of a single-domain magnetic state, thus reducing hysteresis by eliminating the energy dissipation associated with domain wall movement.[66] This implies an importance in determining the condition dependent size effect of $D0_3$-like precipitates. Insights could be provided by establishing a more specific correlation between changes in magnetostriction and the $D0_3$-like precipitates.

In this work, ferroelectric NBT-x%BT single crystals, KNN textured ceramics, and ferromagnetic Fe-x%Ga alloys will be investigated. Objectives of this study are to address (i) mechanisms controlling the piezoelectric response in lead-free systems (NBT-x%BT and KNN) by systematically studying the domain and local structures and their effect on properties, (ii) the effect of Mn substitution on the ferroelectric domain and local structures in NBT-x%BT; and (iii) the structural origin of the peak value of the magnetostriction, near x=19 in Fe-Ga alloys, by analyzing the size of the $D0_3$-like precipitates correlated with thermal treatments and compositions.

The significance of this study would enable an understanding of the structure-property relations on the nano- and macro-length scales, which could be used to (i) identify similarities and differences between MPBs in lead-based and lead-free NBT-x%BT systems; (ii) check for domain engineering of nano-domain structures in lead-free ferroelectrics; and (iii) examine the model of E field induced nonpolar (or pseudocubic) to ferroelectric transitions to explain a giant strain observed near the MPB for NBT-x%BT. We aim to investigate the MPB in NBT-x%BT from the nano-scale structure to the macroscopic physical properties, thus exploring this material's full potential as a functioning lead-free alternative and providing a thorough description and understanding of an MPB in a lead-free system. The work on KNN textured ceramics could extend the understanding of the aging-enhanced properties and possibly expand the application of such an approach not only to coexisting O and T structures, but also to single phase field. Studies on Fe-Ga alloys would further clarify the specific correlation between magnetostriction and the $D0_3$-like precipitates, and reveal the optimized length of short-range ordering of $D0_3$-like precipitates.

Based on the literatures available and our speculations, following hypothesises in this work are addressed as follows:

(i) Nanoscale domain engineering structure in NBT-x%BT contributes to the high piezoelectric response: (i) the high-temperature tetragonal ferroelastic domain structure coexist with a lower temperature rhombohedral ferroelectric phase in NBT; (ii) $BaTiO_3$ refines the size of polar nano-regions and enhances their self-organization; and suppresses formation of proper ferroelastic domains.

(ii) The mechanism of enhanced piezoelectricity for NBT-x%BT near the MPB has both polarization rotation and polarization extension contributions, different than the classical Pb-based ferroelectrics. The in-phase octahedral tilting associated *T* distortion is beneficial for such enhancement.

(iii) Mn increases ferroelectric ordering and enhances in-plane octahedral tilting.

(iv) The assembly of polar nanoregions into larger domain structures is associated with spatial homogeneity of the polarization switching and the relaxation behavior on the surface.

(v) Aging effect exists in the orthorhombic single phase field, not only in the orthorhombic and tetragonal two-phase field as previously reported.

(vi) Quenching decreases the short range ordering in Fe-Ga alloys and the density of $D0_3$-like precipitates increases accordingly, both of which are beneficial for the enhancement of magnetostriction. The optimized length of short-range ordered $D0_3$-like precipitates is on the order of 2-3nm, forming single domain state.

Chapter 2 Experiment

2.1 Sample preparation

2.1.1 $(Na_{1/2}Bi_{1/2})TiO_3$-$BaTiO_3$ crystals and KNN ceramics

Single crystals of NBT-x%BT were grown by a top-seeded solution growth (TSSG) method [11]. <001> oriented wafers of crystals were cut into dimensions of $3\times3\times0.3mm^3$, and the surface was polished down to 0.3 μm finishes. Gold electrodes were deposited on the bottom face of each sample by sputtering. Before PFM measurements, all crystals were annealed at 900 K for 30 min. Careful investigations were performed starting from the annealed condition.

<001> textured KNN ceramics were prepared by a templated grain growth (TGG) technique developed by Chang et al. with strong pseudocubic <001> orientation.[14] Wafers of ceramics were cut into dimensions of $3\times3\times0.3mm^3$, and were subsequently electroded on both surfaces with gold. Samples were poled in silicone oil at room temperature under a dc field of E=3kV/mm for 20min and the aging process was carried out at 170°C for 30 days.

Samples of NBT-BT single crystals and KNN ceramics for TEM were prepared utilizing standard techniques of grinding, dimpling and argon ion-beam thinning (Model 1010 ion mill, E.A. Fischione Instrument Inc., PA, USA). Ion-beam thinning was carried out on both sides of the samples at an inclination angle of 8° to the ion-beam (5kV), which was finally followed by gentle milling (2kV) with an angle of 6° to electron transparency for 20 min in order to remove surface artifacts before TEM examination.

2.1.2 Fe-Ga alloys

Single crystal specimens with various compositions were grown at Ames Lab, and then given different thermal treatments. Annealing was carried out at 900°C for 48h with heating/cooling rates of 5°C/min in an inert gas atmosphere. During quenching, the samples were held at 900°C for 8h, reached at a heating rate of 5°C/min in an inert gas atmosphere, and then dropped into ice water. Samples were cut in a direction perpendicular to the preferred electron beam direction <001> TEM observations. Specimens for TEM study were prepared using the same mechanical and subsequent ion milling method, as described above.

2.2 Property and structural analysis tools

Polarization hysteresis (P-E) and strain vs E-field (ε-E) curves were measured at a frequency of 1 Hz using a modified Sawyer-Tower circuit and a linear variable differential transducer driven by a lock-in amplifier (Stanford Research, SR850). The domain structures of NBT-BT single crystals were studied by polarized light microscopy (PLM) using a Leica Microsystem (Wetzlar Gmbh) equipped with a crossed polarizer–analyzer (P/A) pair and a Linkam THMS600 (Linkam Scientific Instruments Ltd.,Tadworth, Surrey, U.K.) temperature control stage. Temperature-dependent dielectric constant measurements were performed using a multi-frequency LCR meter (HP 4284A). XRD studies were performed using a Philips MPD high-resolution x-ray diffraction (XRD) system equipped with a two bounce hybrid monchromator, an open 3-circle Eulerian cradle, and a doomed hot-stage. The x-ray wavelength was that of Cu$K\alpha$ = 1.5406 Å, and the x-ray generator was operated at 45 kV and 40 mA.

2.2.1 Piezo-response force microscopy

Careful investigations of the domain structure were performed by scanning probe microscopy using the piezo-force mode (DI 3100a, Veeco). During PFM studies, the electrode faces were then glued to the sample stage, and the opposite unelectroded surface was scanned by the SPM tip. All scans were performed at room temperature, using a conductive silicon tip coated with cobalt. An ac modulation voltage of 5V (peak to peak) with a frequency of 25 kHz was applied between the conductive tip and the bottom gold electrode.

PFM measures the mechanical response when a voltage is applied to the sample surface by a conductive tip of an AFM. In response to the electrical stimulus, the sample then locally expands or contracts. The relationship between the strain and the applied field in piezoelectrics is described by a rank-3 tensor. The most important component of this tensor for typical "vertical" PFM is the d_{33} component,[67] since it couples directly into the vertical motion of the cantilever. The voltage applied to the tip is,

$$V_{tip} = V_{dc} + V_{ac}\, cos(wt) \quad (1)$$

resulting in piezoelectric strain in the material that causes cantilever displacement

$$z = z_{dc} + A(w, V_{ac}, V_{dc})\ \cos(wt + \varphi) \quad (2)$$

due to piezoelectric effect. When the voltage is driven at a frequency well below that of the contact resonance of the cantilever, this expression becomes

$$z=d_{33}V_{\mathrm{dc}}+d_{33}V_{\mathrm{ac}}\cos(wt+\varphi) \quad (3)$$

where we have implicitly assumed d_{33} dependent on the polarization state of the material. From this last equation, the magnitude of the oscillating response is a measure of the magnitude of d_{33} and the phase is sensitive to the polarization direction of the sample.

PFM spectroscopy refers to locally generating hysteresis loops in ferroelectric materials. From these hysteresis loops, information on local ferroelectric behavior such as imprint, local work of switching, and nucleation biases can be obtained. Switching Spectrum PFM (SSPFM) extend the mapping of hysteresis loops to a 2-D region. In SS-PFM, a sine wave is carried by a square wave that steps in magnitude with time. Between each ever-increasing voltage step, the offset is stepped back to zero with the ac bias still applied to determine the bias-induced change in polarization distribution (e.g. the size of the switched domain). It is then possible to see the hysteresis curve of the switching of the polarization of the surface (bottom diagram). If the measurements are performed over a rectangular grid, a map of the switching spectra of that surface can be obtained. It offers a number of approaches to the fundamental understanding of ferroelectric materials, including: imaging of nucleation centers on free surfaces, nucleation mechanisms, and domain wall dynamics.[69] It offers a good tool to investigate the polarization dynamics of relaxor surfaces including the polarization switching mechanism, domain nucleation process, and statistical studies of the switching behavior.

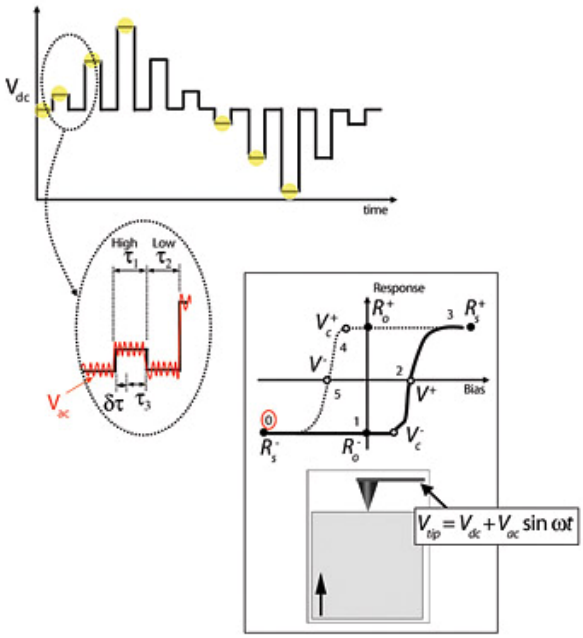

Figure 2.1 In SS-PFM, local hysteresis loop is collected at each point on $N \times M$ mesh. The single-point probing wave form in SS-PFM and data acquisition sequence. Reprint with permission from [69]. Copyright [2006], American Institute of Physics.

2.2.2 Transmission electron microscopy

Selected area electron diffraction (SAED) and bright field image studies were performed using a Philips EM 420 electron microscope working at 120kV, equipped with a double-tilt sample holder to enable access to various zone axes. HRTEM experiments were performed using a FEI TitanTM TEM, operated at 300 kV. Care was taken to orient the individual zone-axis of the specimens parallel to the incident electron beam. Note that in order to obtain the best contrast of domain structures, small tilting of samples was performed before imaging. The principle contrast mechanism of domains can be considered as diffraction contrast due to the atom displacement of dipoles. Digital micrograph software (Gatan Inc., Pleasanton, CA, USA) was used to analyze these HRTEM lattice images.

Chapter 3

Domain and local structures of $Na_{1/2}Bi_{1/2}TiO_3$-x%$BaTiO_3$ single crystals

3.1 Hierarchical domains in $Na_{1/2}Bi_{1/2}TiO_3$-x%$BaTiO_3$ single crystals

The phase transformational sequence on cooling for NBT has been reported to be cubic(*C*)→tetragonal(*T*)→rhombohedral(*R*) [29-33]: with phase transition temperatures of about 520^{o}C and 260^{o}C, respectively. Interestingly, no distinct structural changes associated with the ferroelectric transformation have been reported at the maximum in the dielectric constant T_{max}=330^{o}C [34,35]. It would thus appear that the high temperature (paraelectric) prototypic phase of NBT has tetragonal symmetry, rather than cubic. Ferroelastic domains [71] and a splitting of the lattice parameters [30] have been reported to persist on heating until near 520^{o}C, indicating that this high temperature paraelectric tetragonal phase is ferroelastic. Below T_{max}, the tetragonal phase becomes polar, where it has been reported to have double P-E hysteresis loops indicative of antiferroelectric ordering [24,71] . Furthermore, the ferroelectric *T*→*R* transition is diffuse, as evidenced by temperature dependent dielectric constant measurements [30,34]. An inflection in the dielectric constant near 250^{o}C has been assumed to be that of the *T*→*R* transition, below which relaxor ferroelectric characteristics became evident in the dielectric constant on further cooling. Vakhrushev et al. [30] have conjectured that ferroelectric rhombohedral clusters gradually form within the polar tetragonal matrix over a broad temperature range on cooling between 330 and 200^{o}C.

Relaxor ferroelectrics, such as $Pb(Mg_{1/3}Nb_{2/3})O_3$-x%$PbTiO_3$ or PMN-x%PT, are characterized by the presence of polar clusters as observed by electron microscopy [72]. With increasing x, PFM and polarized light (PLM) microscopy investigations have shown [19,73] that these polar nano-regions self-assemble into small domain striations along the <110> that are sub-micron sized, which subsequently geometrically organize into large {100} platelets or bands of about 100μm in size. These hierarchical domain organizations are similar to those of martensite [74,75] where such arrangements achieve stress accommodation relaxing the elastic energy.

However, in-spite of the relaxor analogy for the *R* phase of NBT, neither the presence of polar nano-regions nor Hierarchical domains has yet been reported.

3.1.1 Domain state in $Na_{1/2}Bi_{1/2}TiO_3$

Here, we have studied the phase transformation and domain structures of NBT by a variety of structural and microstructural methods. We find (i) that the high temperature tetragonal ferroelastic domain structure is unchanged on cooling from 520 to 25^{o}C, where it is elastically inherited by the ferroelectric rhombohedral phase; and (ii) that polar microdomains nucleate on cooling in the rhombohedral ferroelectric phase, tending to self-organize to a limited extent along <110>. These results reveal a unique presence of independent ferroelastic and ferroelectric domain structures.

First, we show the phase transformational characteristics in Figure 3.1. Temperature dependent dielectric data are given in Part (a). In this figure, we can see that the dielectric maximum occurs near 330^{o}C, near and just below which the dielectric constant is frequency independent. On further cooling, an inflection was found near 250^{o}C below which notably frequency dispersion was observed. This dispersion was similar to that of relaxors below T_{max} [76], indicating polar heterogeneities with low frequency fluctuations. In Part (b), temperature dependent lattice parameters are given. These data reveal a splitting of the *c* and *a* parameters in the temperature range between 300 and 530^{o}C: demonstrating that both the polar (near and below T_{max}) and prototypic (>T_{max}) phases have tetragonal symmetry. Below 300^{o}C, the structure transformed to rhombohedral (i.e., pseudo-cubic). No other structural changes were found at the Curie temperature, or at the inflection in the dielectric constant near 250^{o}C. These XRD results do not preclude that a structural phase transition occurred on a local scale in some regions of the crystal near or above T_{max}. A diffuse phase transformation is apparent in the broad dielectric response with a maximum near T_{max}, consistent with this possibility. However, if such local $T \rightarrow R$ transitions occur, they have correlation lengths less than that of the coherence length of X-ray required by the optical diffraction conditions. Thus, they would not be detectable at the Bragg conditions.

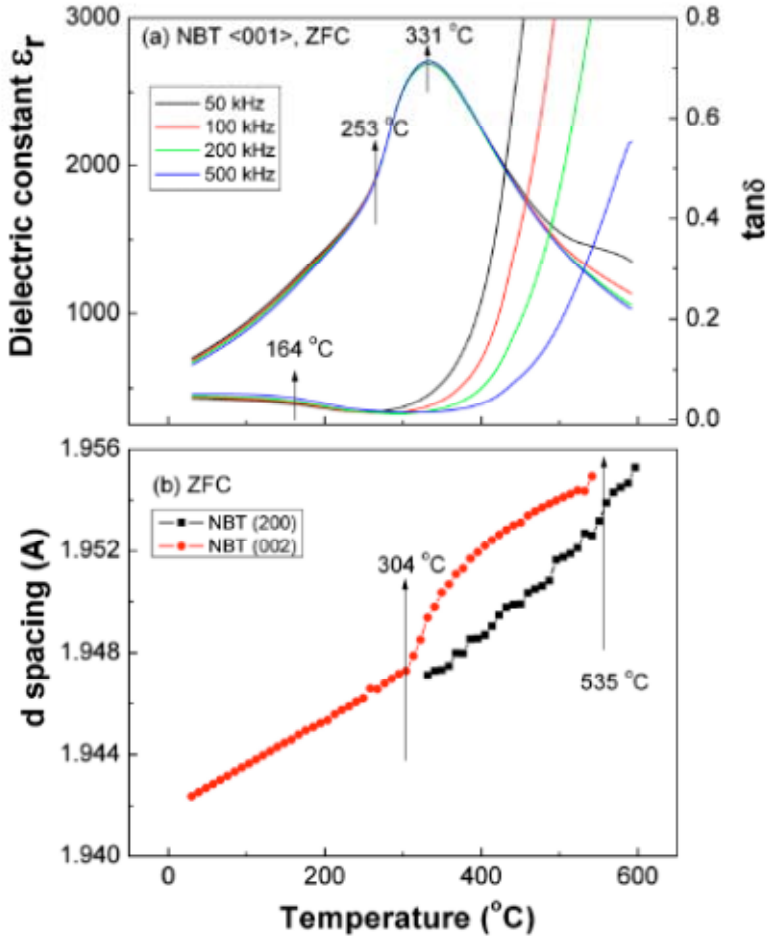

Figure 3.1 Phase transformation characteristics of <001> oriented NBT single crystal in the zero-field cooled condition, observed by (a) temperature dependent dielectric constant measurements taken at various frequencies; and (b) temperature dependent lattice parameter measurements.

Next, we show the presence of a ferroelastic domain structure in both the *R* and *T* phase fields. Figure 3.2 shows PLM images taken at various temperatures: (a) and (b) 25°C in the *R* phase; (c) and (d) 250°C near the temperature at which frequency dispersion became evident in the dielectric constant; (e) and (f) close to but below T_{max} at 325°C; (g) and (h) at T_{max}=330°C, where dielectric constant shows maximum; (i) and (j) near but below the $T \rightarrow C$ transition at 500°C; and (k) and (l) in the *C* phase at 550°C. The angles (θ) provided in the images is that between the polarizer/analyzer (P/A) pair and the pseudocubic <110>. The left column shows images at θ=0°, and the right one at θ=45°.

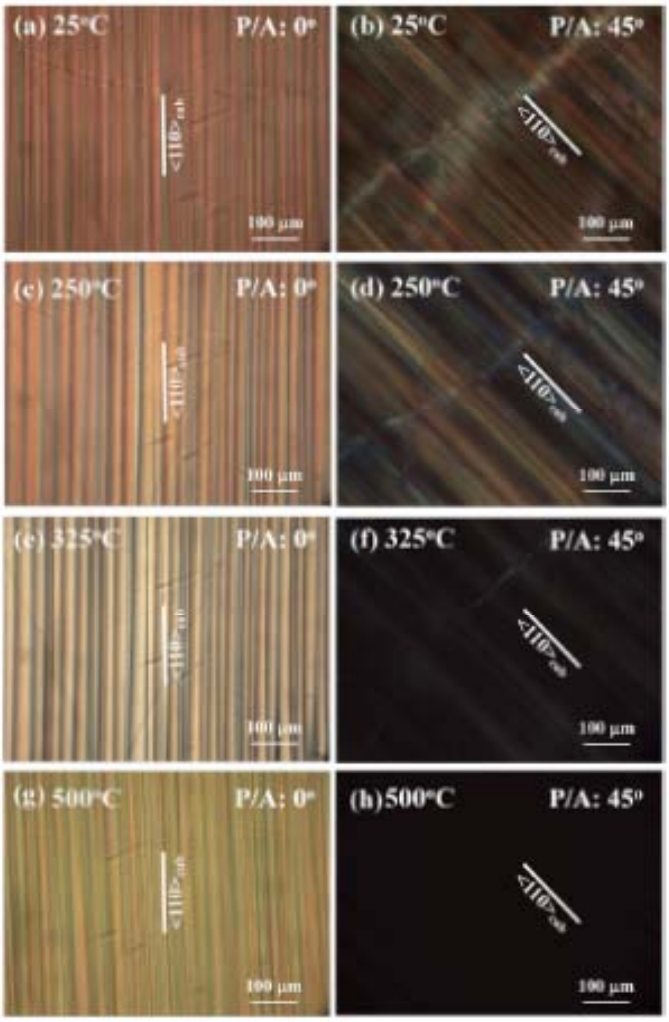

Figure 3.2 Polarized light microscopy (PLM) images taken at various temperatures of (a, b) 25°C, (c, d) 250°C, (e, f) 325°C, (g, h) 330°C, (i, j) 500°C, (k, l) 550°C.

Please note that the images in Fig. 3.2 clearly reveal the presence of tetragonal ferroelastic domains for temperatures below 500°C, which have a width of about 10~100μm and a length on the order of hundreds of microns, and which are oriented along the <110>. These ferroelastic domains disappeared on heating at the $T \rightarrow C$ transition near 550°C. It is important to note that the size, shape, and position of these ferroelastic domains were somewhat unchanged with temperature on cooling between 500°C and room temperature, even though the sample went through (i) two polar phase transformations on cooling, and (ii) that the ferroelastic tetragonal strain (*c/a*) disappeared at 300°C on cooling into the *R* phase. These findings clearly demonstrate

that the ferroelastic domain structure is inherited into the rhombohedral polar phase at room temperature.

Also, please note in Figure 3.2 the extinction at different temperatures. At 550^{o}C, complete extinction was found for θ=0 to 360^{o}: this indicates that NBT is cubic and optically isotropy as revealed by XRD data in Fig.3.1(b). On cooling to 500^{o}C in the *T* phase field, ferroelastic domain appeared and the extinction angle was θ=45^{o}+m·90^{o} (m=0, 1, 2 and 3): this is the typical extinction position for tetragonal structures. The extinction angle did not change on cooling to T_{max}=330^{o}C. However, complete optical extinction could not be maintained on cooling to 325^{o}C (see Fig.3.2f), even though NBT was still tetragonal by XRD. These results indicate that ferroelectric R phase nuclei have begun to form in the tetragonal matrix, as the *R* structure has extinction for θ=0^{o} rather than θ=45^{o}. On cooling to and in the *R* phase field, the contrast in the extinction images for θ=45^{o} became more pronounced, as can be seen in Figs.3.2b and 3.2d; whereas, the contrast in the images for θ=0^{o} also became darker on cooling between 325^{o}C to 25^{o}C. Comparisons of the PLM images at various temperatures show that the optical extinction conditions gradually change with decreasing temperature below T_{max}. However, complete optical extinction could not be achieved in the *R* phase field. This indicates that the ferroelectric *R* domains in NBT crystals could not organize into large domain platlets or bands, as previously reported for PMN-PT crystals [19,73]. These results clearly illustrate the diffuse nature of the phase transformation, and that polar R nuclei initially begin to form near T_{max}.

Finally, we have performed investigations of the domain structure of NBT over various length scales using different types of microscopy. These investigations have shown the presence of two different types of domain structures of different characteristic sizes. We confirmed the presence of ferroelastic domains by optical mode and Raman mode SPM as shown in Figs. 3.3(a) and (b). In this case, <110> oriented domains of width about 10μm were found, consistent with the PLM images (See Fig.3.2). We then performed SPM investigations using the piezo-force mode (or PFM), so that we could detect the ferroelectric domain structure. Figures 3(c) and (d) show typical PFM images, which reveal the presence of much smaller ferroelectric domains that exist within the ferroelastic domains of larger length scale. The size of these ferroelectric domains was on the order of 0.2 to 0.5μm. The spatial distribution of these ferroelectric microdomains was not well organized; however, comprehensive studies by PFM showed that the ferroelectric domains had some tendency for organization along the <110> direction.

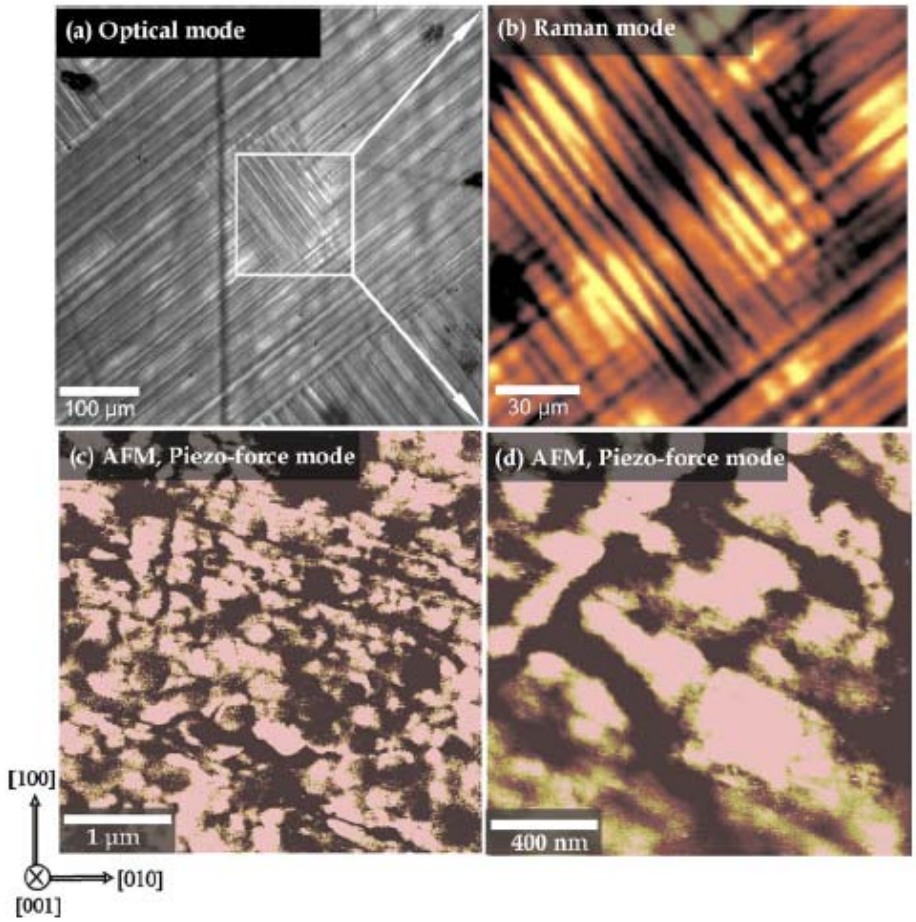

Figure 3.3 Domain structure of NBT at different lengths scales taken by (a) atomic force microscopy using an optical mode; (b) atomic force microscopy using a Raman mode, which demonstrates ferroelastic domains of about 10μm; (c) atomic force microscopy, which shows ferroelectric domains of about 0.2~0.5μm in size; and (d) a higher resolution image of ferroelectric domains, which demonstrates much clear ferroelectric domains that exists within side the feroelastic ones.

Generally in a distortive phase transformation, changes in the domain variant distribution and population allow the achievement of the elastic compatibility conditions and minimization of the elastic free energy [77]. However, our findings show a unique sequence of phase transformations in NBT, where a ferroelastic *T* domain structure is inherited into a ferroelectric *R* phase. This is important because it means that the polar *R* phase is geometrically and elastically restricted by its high temperature ferroelastic *T* parent phase. On cooling into the *R* phase,

ferroelectric microdomains then form within the ferroelastic *T* domains. The system can organize the ferroelectric microdomain distribution in an attempt to achieve the invariant plane strain conditions: however, a fully-relaxed elastic state is clearly not achieved for NBT. Because complete stress accommodation is not achieved, the polar microdomain ensemble may undergo low frequency dynamical fluctuations, typical of a relaxor ferroelectric state.

3.1.2 Evolution of domain structures in $Na_{1/2}Bi_{1/2}TiO_3$ -x%$BaTiO_3$

Investigations of the domain structure of NBT and NBT-x%BT have previously been performed by TEM.[35,78] Domains were not observed by TEM for x=3 and 8 [68]: which might be due to electron beam effects.[72] However, PLM studies of NBT (i.e., x=0) have shown the presence of ferroelastic domains of size 10-100μm in the high temperature paraelectric *T* phase. These ferroelastic domains form on cooling at the *T*→*C* phase boundary near 550ºC. Clearly, the *T* domains must be proper ferroelastics. Proper ferroelastic twins form to achieve elastic compatibility between regions of different orientational variants having strain as a spontaneous order parameter [79]. Improper ferroelastic twins can accompany ferroelectric domain formation, due to an electrostrictive coupling of the polarization to the lattice strain [80]. But, improper ferroelastic twins disappear on heating above the ferroelectric→paraelectric boundary.

Scanning probe microscopy (SPM), performed in the piezoresponse mode (PFM), provides a way to study the ferroelectric domain structures at various length scales with high spatial resolution, and could be used to study the ferroelectric domains of NBT-x%BT. The prior investigations of NBT by PFM have revealed the presence of polar nano-regions in the ferroelectric R phase field. Formation of these nano-regions occurs on cooling at temperatures below the dielectric maximum (T_m). Interestingly, the high temperature ferroelastic *T* domains remained present in the ferroelectric R phase field, as shown by PLM.

Here, we report an investigation of the evolution of the domain structure of (001) oriented crystals of NBT-x%BT for x=0, 4.5, and 5.5 by means of PFM and PLM. Investigations were focused on revealing how the domain structure changes with the addition of BT, as the MPB is approached. The results show with increasing x that (i) the polar nano-region width is decreased, and the nano-regions become increasingly self-organized; and (ii) the formation of proper tetragonal ferroelastic domains is suppressed, and rather improper ferroelastic ones formed below the ferroelectric Curie temperature. Our findings provide insights into why the piezoelectric properties of NBT-x%BT are enhanced with increasing x, as the MPB is approached.

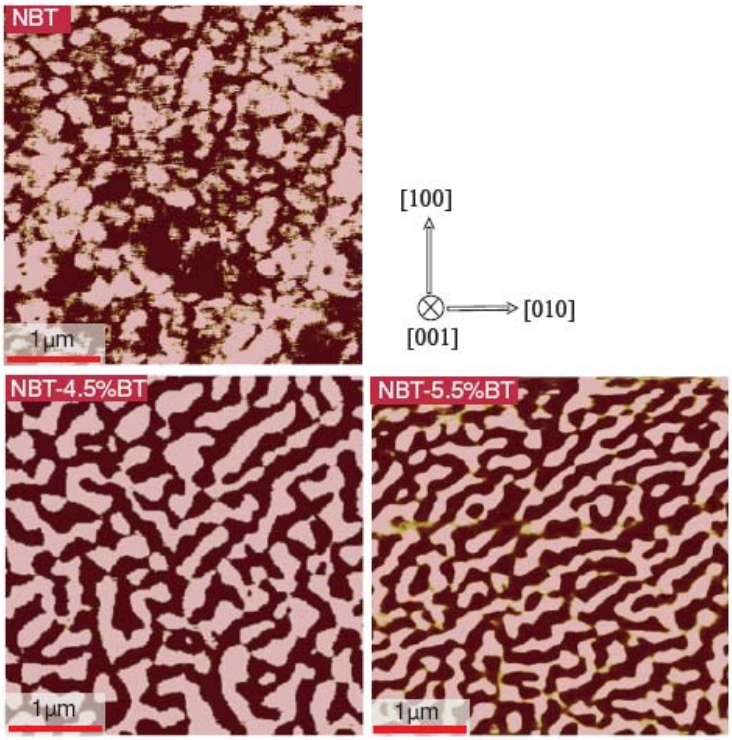

Figure 3.4 Ferroelectric domains of (001)-oriented NBT, NBT-4.5%BT and NBT-5.5%BT crystals revealed by PFM.

Figure 3.4 shows PFM images of unpoled (001)-oriented crystals for (a) x=0, (b) 4.5% and (c) 5.5%. The image for NBT reveals the presence of polar nano-regions (PNRs) that are on the order of 50nm to 500nm in size, as recently reported. It is worth to note that the PNRs for NBT can be expected to have a size of about 10nm,[81] and in fact, our TEM images are consistent with this expectation. However, for NBT, the size of the PNRs revealed by PFM is considerably larger, and no self-organization into periodic patterns was found. It is possible that individual PNR are not able to be observed by PFM due to a small value of d_{33} that provides modest contrast: rather we may only observe colonies of them that are not well-organized. These nano-regions may not have appeared well organized, although optical diffractograms obtained by fast Fourier transforms showed some tendency to organize along the <110>. Furthermore, their distribution was not very uniform, and the boundaries between regions were quite rough.

With increasing $BaTiO_3$ content to 4.5%, the distribution of nano-regions became more uniform than for NBT. In particular, the length became notably longer along the <110> with sizes on average of >1μm. Furthermore, the boundaries between regions became much smoother.

The labyrinthine domain pattern is indicative of the local deviation of surface symmetry from cubic [82]. With further increasing BT to 5.5%, these changes became more pronounced: with lengths becoming on average >2 μm. One notable difference with increasing BT content between x=4.5% to 5.5% was that the widths of the polar regions were refined to a thickness of <100nm. As the MPB region was approached, this increased length and decreased width resulted in a stripe-like morphology with an orientation along the <110>. These results clearly show a tendency of increased self-organization of the polar regions with increasing BT. Polar nano-regions organized into stripe-like domains of increasing length along the <110>. These changes with x%BT are similar to those previously reported for $Pb(Mg_{1/3}Nb_{2/3})O3$-x%$PbTiO_3$ (PMN-x%PT) with increasing x%PT [19,83] as the MPB region in that solution was also approached.

Polarized light microscopy is widely used in transmission geometry and the principle of setup in our case is as following: the orientation herein is based on the axis of a prototype cubic phase of the perovskite structure. Based on the lattice symmetry, when a single crystal sample is observed along the crystallographic <001> direction under cross-polarized light, domains of the T phase exhibit optical extinctions when the polarizer is set along the <100> or <010> directions. For domains of the R phase, they exhibit optical extinction when the polarizer is set along the <110> crystallographic directions, namely in an angle of 45^0 with respect to the [010] direction. This enables us to distinguish the possible different phases in the crystals.

Figure 3.5 shows the PLM images of (001)-oriented NBT taken at temperatures of (a) 25℃, and (b) 550℃. Comparisons of these figures will reveal that structural domains oriented along the <110> formed on cooling below 550℃, as recently reported. The domain lengths were on the order of hundreds of microns, and their widths between 5 and 100μm. Please note that we used reflected light to observe domain formation, and that the results are consistent with those obtained using polarized light where optical extinction was found to occur at 550℃ in the *C* phase field. The formation of these domains corresponded in temperature to that of the paraelectric *C*→paraelectric *T* phase boundary, which is far above that of the dielectric maximum at about T_m=330℃. The crystal lattice parameters of this phase were confirmed by x-ray diffraction to be tetragonal with c/a≈1.01. Clearly, these tetragonal structural domains are proper ferroelastic ones.

Interestingly, these T ferroelastic domains persisted on cooling into the ferroelectric R phase field below 300℃, and remained nearly unchanged at 25℃. This demonstrates that the invariant

conditions established to relax the elastic energy in the *T* phase persist into the *R* phase field, even though the structure is no longer tetragonally distorted and that c/a≈1.00: i.e., there is a geometrical and elastic inheritance from the parent paraelectric/ferroelastic tetragonal phase into the product ferroelectric rhombohedral one. On cooling below the *T*→*R* phase boundary, polar nano-regions formed, as discussed above with reference to Fig.3c (25℃), and as re-shown in Fig.3c at higher resolution for comparative purpose with the PLM images.

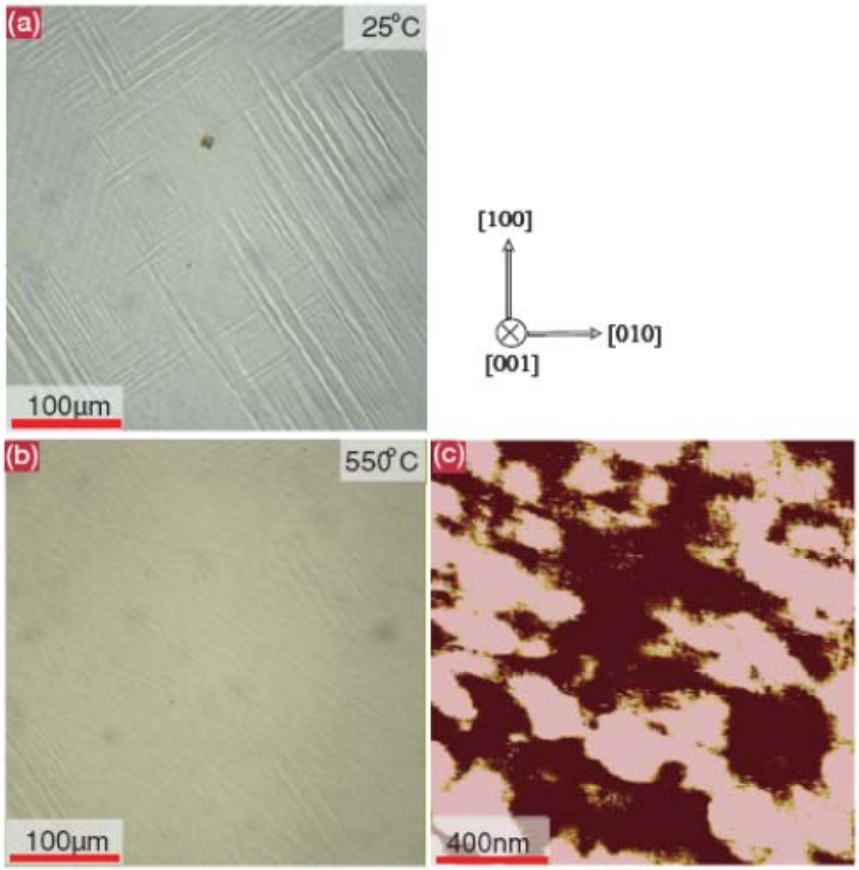

Figure 3.5 Domain hierarchy of (001)-orientated NBT. (a) Tetragonal ferroelastic domains with a <110> preferred orientation revealed by PLM at room temperature; (b) ferroelastic domains begin to disappear at 550 ℃; (c) PFM image showing irregular ferroelectric nano-domains.

These findings for NBT thus demonstrate the presence of two different types of co-existing domains in NBT: large (10-100μm) proper ferroelastic ones that form at high temperatures, and much smaller (100-500nm) polar regions that form at lower temperatures. The polar regions are

embedded in the *T* ferroelastic domains. Please note that the ferroelastic domain structure does not form or change to stress-accommodate the polar ones. The polar R regions do not assemble into bands defined by the invariant plane strain to relax stress [84], but rather nucleate within the pre-existing geometrical restrictions of the proper ferroelastic domains.

Figure 3.6 shows the PLM images for NBT-4.5%BT at temperatures of (a) 25℃, and (b) 176℃. At room temperature, macrodomain platelets notably larger than those for NBT were observed: which were of length >500μm and of width ≈50μm. These domain platelets for NBT-4.5%BT were oriented along the <100> direction, rather than the <110> as for NBT. We note that the domain platelets were observed when one of the P/A axes was oriented along the $<100>_{cub}$ and when the polarizer was set along the <110> directions that optical extinction was found. This infers that no true T ferroelastic phase exists in NBT-4.5%BT as for NBT, and that these macrodomain platelets have the Rhombohedral structure. Furthermore, these macrodomain platelets for NBT-4.5%BT were found to disappear on heating above 175℃, as can be seen in Fig.3.6b. This temperature was notably below that of the dielectric maximum of T_m=300℃, and rather is close to that previously attributed to a transformation between ferroelectric and antiferroelectric *R* phases [85]. Clearly, significant and important changes have occurred with regards to the nature of these macrodomain platelets with increasing BT content. It is important to note that structural studies by XRD failed to reveal a tetragonal phase at temperatures above the dielectric maximum for x>2 (data not shown); rather, the phase transformational sequence on cooling was found to be paraelectric $C \rightarrow R$. Comparisons of these data with our finding demonstrate that the platelets for NBT-4.5%BT are not true tetragonal ferroelastic domains.

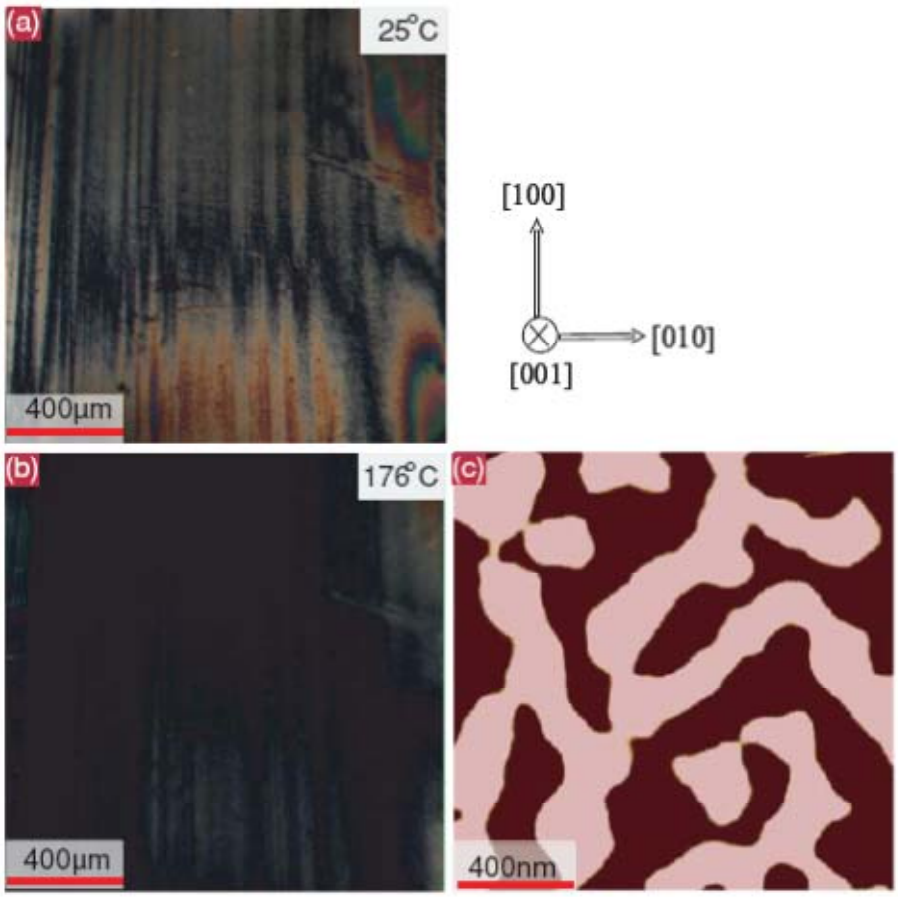

Figure 3.6 Domain study of (001)-orientated NBT-4.5%BT. (a) Macrodomain platelets with a <100> preferred orientation by PLM in room temperature; (b) Optical extinction began to occur at 176 ℃; (c) PFM image showing long stripe-like ferroelectric nano-domains.

Furthermore, these changes in macrodomain platelets with x% were accompanied by important changes in the self-organization of the polar regions as observed by PFM, and as re-shown in Fig.3.6c at higher resolution for comparative purpose; where stripe-like domains were found that were of width 150nm and of lengths >1μm. Please note that self-organization occurs along the <110>, which is the direction along which elastic compatibility can be achieved for either R or T domains. These results strongly indicate an important role of stress accommodation between polar nano-regions in the self-organization process.

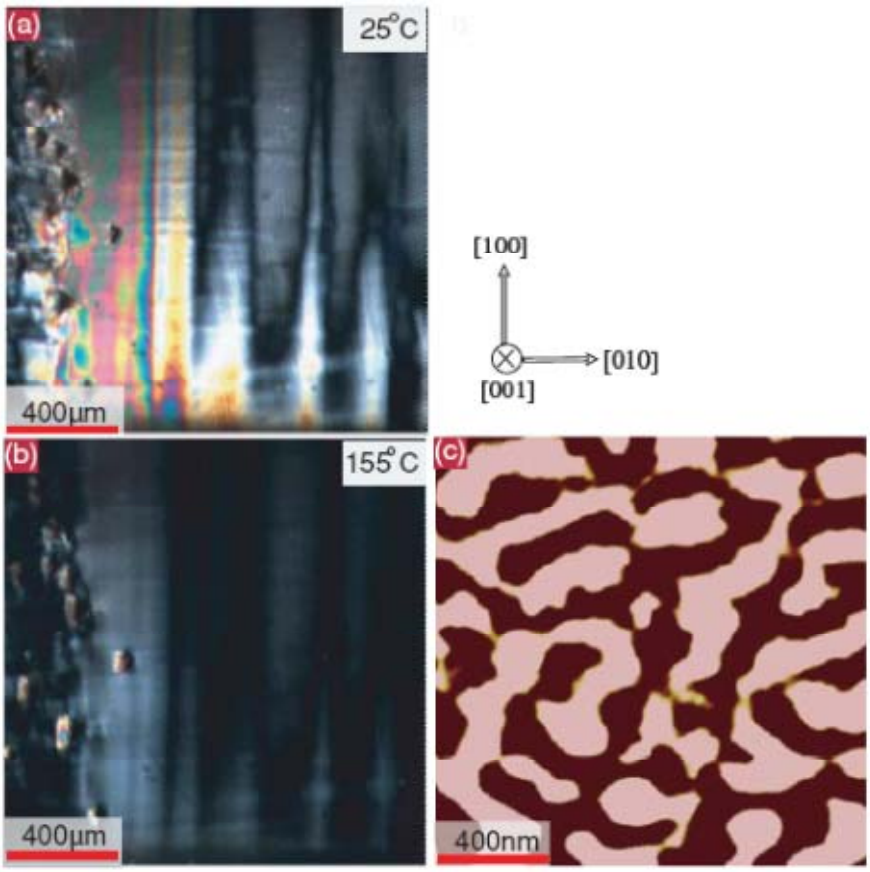

Figure 3.7 Morphology and domain structures of (001)-orientated NBT-5.5%BT. (a) optical image which reveals that a <100> preferred oriented macrodomain platelets; (b) optical extinction occurs at 155℃; (c) high-resolution PFM image showing long stripe-like nano-size ferroelectric domains.

Similar results can be seen in the PLM images given in Figure 3.7 for NBT-5.5%BT at temperatures of (a) 25℃, and (b) 155℃. Again, macrodomain platelets can be seen that are oriented along the <100>, although they are notably larger than those than those for NBT-4.5%BT. In particular, the widths were increased to about 200-400µm, as the MPB compositional region was approached. These macrodomain platelets disappeared on heating at 155℃, which was notably below the dielectric maximum at 300℃. A PFM image at high resolution is re-shown in Fig.3.7c for comparative purposes, which reveals similar features as those for NBT-4.5%BT: with the exception that the polar regions were longer and narrower, as noted above.

These findings for NBT-4.5%BT and NBT-5.5%BT thus demonstrate the presence of a ferroelectric domain structure, which minimizes its elastic energy by the geometrical arrangement of ferroelectric domains into macrodomain platelets. Such types of stress-accommodating domain structures are typical of any displacive transformation, which can achieve a domain-averaged transformation strain that is an invariant plane strain [84]. These macrodomain platelets for NBT-4.5%BT and NBT-5.5%BT are not true ferroelastic domains, but rather are improper ferroelastic ones that arise due to the electrostrictive coupling of the spontaneous polarization to the lattice.

Clearly, there are dramatic changes in the domain structure(s) of NBT-x%BT with modest changes in x, as the MPB is approached. Before we turn to the analysis of the domain structure of NBT-x%BT, here we are going to discuss a couple of possible factors existed in experiments which would help in understanding the data better.

First, when consideration of surface state and specimen, surface states or "skin effects" are known in PMN-x%PT relaxors.[82,86,87] These surface states result in an apparent "phase X" or distorted Cubic. However such surface states have not been reported to have either Rhombohedral or Tetragonal structures. Studies of PMN-x%PT by PFM have revealed PNRs for composition of x<30at.%, where "phase X" and a Cubic phase (x<25at.%) are known.[19] Such surface states in PMN-x%PT do not exhibit self-organization of PNRs into somewhat periodic arrangements until when the Monoclinic and Tetragonal phases are stable near the MPB. In this region of the PMN-x%PT phase diagram (i.e., where Mc and T phases are stable), surface states are not found.

The possibility that the PNRs of NBT might have influence from the surface condition was considered. Our TEM images reveal PNRs that are similar in morphology to those by PFM: however, those by PFM are larger. We are not for sure if it is a surface effect that makes them appear larger, or rather the low d_{33} of 25 pC/N reduces the contrast in the PFM image. Probably, colonies of PNRs in NBT were imaged whose individual PNRs cannot be resolved because of a low d_{33}. It is noted that the self-organization of PNRs into more periodic twin structures with increasing x at.%BT is much like that of PMN-x%PT near its MPB.[19] However, surface states are not the cause, rather relaxation of the elastic energy by stress accommodation.

In order to verify that our observations on the ferroelectric domains have validity to the bulk, two issues need to be mentioned. First, elastic accommodation that drives self-assembly of the

polar nano-regions into more periodic arrays is a long-range force. It achieves a lower energy configuration by volume effects. Such changes in domains with x at.% have validity not just to surface states, but rather to bulk ones. Second, charge compensation during the PFM imaging needs to be considered. In this study, the effect of small ac biases applied to the PFM tip and to the bottom of the sample was compared: both cases showed similar results. If charge compensation occurred, the results of the two cases would not be the same. Therefore, it can be inferred that the effect of charge compensation on PFM images is negligible for the NBT-x%BT system. In order to minimize the possible influence of a charged PFM tip on the surface domains, especially for electrostatic tip-surface interactions, the PFM tip (DDESP, Veeco) with a cantilever spring constant of 20-80N/m was used, which should guarantee that the influence of a charged PFM tip on domains is negligible in present study.[88-90]

Next we attempt to summarize the changes we observed in section III into a diagram, as shown in Figure 3.8. Please note that we begin by using the previously published NBT-x%BT phase diagram [24], and superimpose on this diagram changes in domain stability. We refrain here forward from referring to it as the equilibrium phase diagram.

First, we modified the diagram by including at low BT concentrations of x<2% the high temperature tetragonal paraelectric phase. The $C \rightarrow T$ phase boundary for NBT is shown to be at about 550℃, and is represented by a solid point. However, we do not know for sure what happens to the $C \rightarrow T$ phase boundary with small increases in x, other than the simple fact that it disappears by x≈2%. This was confirmed both by recent XRD studies which reveal that the c/a splitting of the *T* phase disappears (data not shown), and the fact that we observe the *T* ferroelastic domains to disappear for x<4%. Thus, we represent the $C \rightarrow$paraelectric *T* phase boundary for x<2% by a dashed line. In this paraelectric T phase field, we show that true ferroelastic domains are present. These ferroelastic domains are of length >100μm and were oriented along the <110> direction.

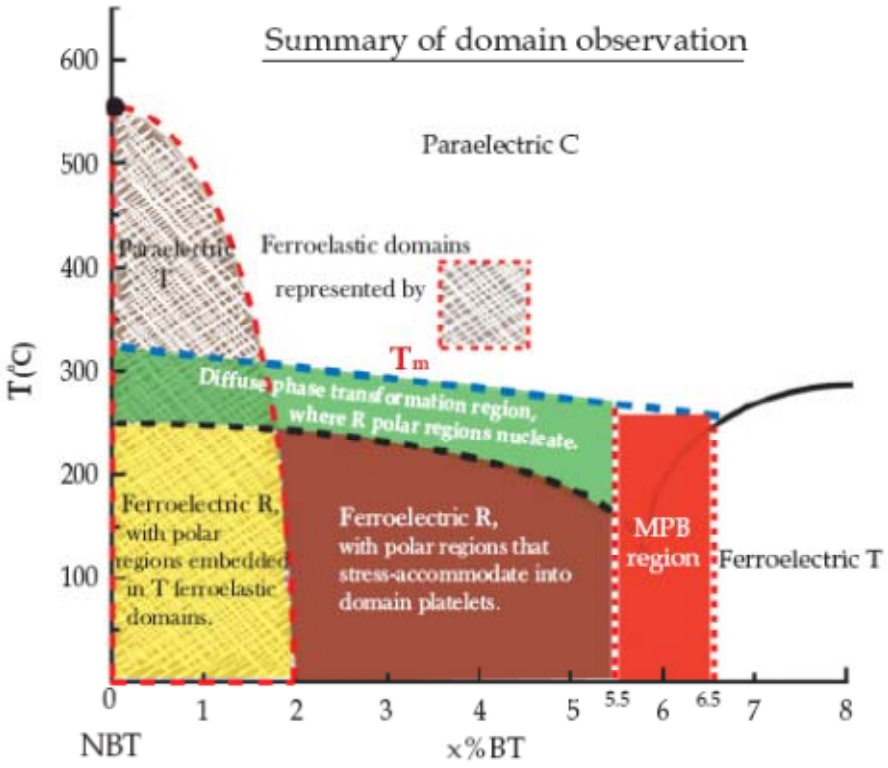

Figure 3.8 Summary of domain observation/ phase diagram of NBT-x%BT.

An intermediate phase field is shown that is sandwiched between the paraelectric and ferroelectric phases. We refrain from assigning the crystal class for this phase field. Prior investigations have given evidence of intermediate antiferroelectric phases that are rhombohedral [10], structurally modulated orthorhombic phases [26], and tetragonal ferroelectric phases [91]. Our investigations by PLM have shown that on cooling between 320 and 200℃ that there are gradual changes in the optical extinction conditions, indicating a diffuse transformation region, where R polar regions gradually nucleate and increase in volume fraction with decreasing temperature. This is consistent with the broad dielectric constant maximum, which is also a hallmark feature of a diffuse transformation [92]. Our recent XRD studies showed that the average structure in this temperature range is pseudo-cubic. However, we note that within this pseudo-cubic structure that polar nano-regions that are electrostrictive exists, which are elastically clamped by their matrix. Thus, it is possible that alternative near-degenerate thermodynamically metastable states could exist, that try to relax the elastic energy of clamped elastically distorted polar nano-regions: which might rationalize the various differing results

from prior studies. We designate this phase field in the diagram as a diffuse phase transformation region, where *R* polar regions nucleate that are elastically clamped. The upper boundary between this phase field and the paraelectric state is defined by the temperature of the dielectric maximum [93,94]. The lower boundary between this phase field and the rhombohedral ferroelectric state is defined by the onset of frequency dispersion in the dielectric constant [93-95]. We note that both of these boundaries, although previously shown in published phase diagrams defining an antiferroelectric phase, are imprecise: thus, we also denote them as dashed lines.

Next, we show the low temperature rhombohedral *R* field for x<6%, whose upper boundary was designated just above to be determined by the onset of frequency dispersion in the dielectric constant [93-95]. We show this *R* phase field to be "divided" by a dashed boundary representing an unknown limit of stability for the tetragonal ferroelastic domains. For x<2%, we show in the diagram that polar *R* domains (which nucleate in the diffuse phase transformation region) are embedded in the *T* ferroelastic domains. In this area of the diagram, the entire matrix is converted into *R* polar nano-regions, but yet the ferroelastic domains persist. These polar nano-regions cannot stress-accommodate each other by geometrically arranging themselves into domain platelets that achieve a domain-averaged transformation strain that is an invariant plane strain. The crystal lattice parameters in this area of the diagram have been shown to be rhombohedral , with a small rhombohedral distortion angle of α_r=89.90°. For x>2%, we show in the diagram that polar *R* domains exists that are stess-accommodating into macrodomain platelets. These macrodomain platelets are improper ferroelastics. The crystal parameters in this area of the diagram have been shown to be (a_r,α_r)=(3.96Å, 89.98°). Thus, the average structure is nearly, if not, pseudo-cubic: similar to that of relaxor ferroeletrics.

Furthermore, in this diagram, we show the MPB region between rhombohedral and tetragonal ferroelectric phases, near x=6%. We have drawn the boundary to be wide between 5.5<x<6.5%. This is because recent investigations [96] have shown that the location of this boundary in composition space, x, can somewhat depend on the electrical history of the sample. It is interesting to note that near this MPB boundary is where the dielectric and piezoelectric constants have been reported to be maximum. The refinement of stress-accommodating ferroelectric domains may be an important contributing factor to the enhancement of the piezoelectric properties near the MPB. Refinement of ferroelectric domains would lead to an increased domain wall density, which may act as natural nucleation sites for inducing phase

transitions [97]. At lower BT contents, the piezoelectric properties may be suppressed by the ferroelastic domains, which are independent of the ferroelectric ones and which seem to suppress their ability to stress-accommodate.

Finally, we try to understand the competing order parameters and we applied the Tagantsev-Balashova model [98,99] to analyze the competition of structural and ferroelectric instabilities in NBT-xat.%BT. The existence of true ferroelastic domains in the NBT-xat.%BT system makes the sequence of phase transformations more complex than the model. The most relevant equation for our use is:

$$T_c=(T_{cp}-\boldsymbol{\Delta}T_{c\boldsymbol{\eta}})/(1-\boldsymbol{\Delta})$$

$$b/a = 1-\boldsymbol{\varphi\Delta}$$

where $\boldsymbol{\Delta}$ is the difference in the temperature dependence between the energies of the nonpolar ordered state and the polar state; $\boldsymbol{\varphi}$ is the coupling between these order parameters; *a* and *b* are the slopes of the reciprocal dielectric constants with temperature in the paraelectric and nonpolar ordered states, respectively. Figure 3.9 (a) shows the dielectric constant for NBT taken at a frequency of 100KHz: from which the structural (i.e., antiferroelectric) phase transition temperature can be seen to be $T_{c\boldsymbol{\eta}}$=598K. We identified from in the dielectric data, that T_c=498K, which corresponds to the ferroelectric phase transition temperature. The value of T_{cp}=518K was determined by the reciprocal dielectric constant extrapolated using the Curie-Weiss relationship, as shown in Figure 3.9(b).

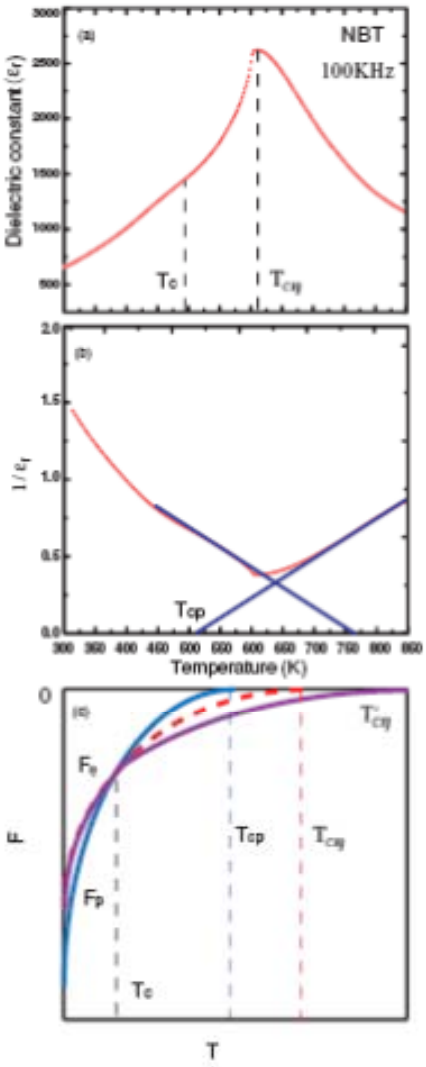

Figure 3.9 Temperature dependences of the dielectric constant of NBT (a); (b) reciprocal dielectric constant; and (c) schematic temperature dependences of the energies of polar F_p and nonpolar F_η ordered states for NBT system.

We can then estimate that φ=10.2 and Δ=0.2 for NBT. Accordingly, following the Tagantsev-Balashova model, we can ascribe the behavior to the S region, which is considered as an intermediate region between antiferroelectric and ferroelectric behaviors. This in term reveals that transformational sequence is antiferroelectric to noncritical first-order ferroelectric, the latter being accompanied by a weak dielectric anomaly.

In the S region, two conditions for independent parameters should be valid: these are $\varphi\Delta$>1 and Δ <1. The first condition means that the structural order parameter, which appears at $T< T_{c\eta}$,

suppresses completely the ferroelectric instability: i.e., a critical ferroelectric phase transition is impossible, as in the temperature range below $T_{c\eta}$ there is no point where the nonpolar ordered state loses its stability. The second condition (Δ<1) means that the energy of the polar state changes with temperature faster than that of the nonpolar ordered one. The temperature dependent free energies of the states are illustrated in Figure 3.9(c). At T_c , these conditions mean that the energies of the two states are equal; where for $T< T_c$, the polar phase appears by means of a noncritical first-order ferroelectric phase transition. [98,99]

Following this approach, a structural instability is realized before the ferroelectric one at a temperature of $T_{c\eta} > T_{cp}$, and the polar state then appears by means of a non critical first-order phase transition at T_c . This transition is a result of a difference in the temperature dependence of the energies of the polar and nonpolar ordered states as illustrated in Figure 3.9(c). Following the Tagantsev-Balashova model, the system would enter into a paraelectric state above $T_{c\eta}$ and structural stability would be achieved.(follow the red dashed line in Fig. 3.9.) However for NBT, there are some important differences that we need to note, with respect to this model. As we know, NBT has an additional transition from a tetragonal paraelectric phase to a cubic paraelectric phase near 550°C. We can designate this temperature as $T'_{c\eta}$: please note that its structural instability is different in nature than that of the Tagantsev-Balashova theory. At T_c , structural stability of NBT is not achieved, and the system remains unstable until the temperature $T'_{c\eta}$ is reached (as shown the revised line in Fig.3.9(c)).

3.2 Local structures in $Na_{1/2}Bi_{1/2}TiO_3$-x% $BaTiO_3$

Near the MPB of PMN-x%PT and PZN-x%PT crystals, structurally bridging monoclinic (*M*) phases that separate rhombohedral (*R*) and tetragonal (*T*) ones have been reported.[6,7] Polarization rotation within these *M* phases is believed to be the mechanism of enhanced piezoelectricity. The MPB of NBT-x%BT is found near 5.5<x<6.5 at.%, where the highest piezoelectric constants and electric field induced strains are found.[9-11] In spite of comprehensive investigations of NBT-x%BT, structurally bridging *M* phases have not been found that have significant c/a ratios in domain engineered states, similar to that of PMN-PT and PZN-PT.[6,7] However, recent evidence exists of a very weak monoclinicity for NBT, suggesting that it may not have a strong correlation between polarization rotation in a monoclinic distorted structure and enhanced piezoelectricity.[61,62] Thus, the mechanism of enhanced piezoelectricity in MPB compositions of NBT-x%BT remains in question. An alternative model of an electric field induced nonpolar (or pseudocubic) to ferroelectric transition was proposed to explain a giant strain observed near the MPB for NBT-x%BT.[63-65] To date, a detailed understanding of the local nonpolar structure is unclear, especially its evolution with compositions approaching the MPB. Therefore, systematic studies of the complex structural evolution with x would help to evaluate the structure-property relations and to identify the mechanism of enhancement near the MPB.

3.2.1 Composition dependent octahedral tilting

Here, we have studied the domain structures and octahedral tiltings of NBT-x%BT for x=0, 4.5, and 5.5 by TEM methods of bright field (BF) imaging and SAED. We found with increasing x that: (i) the size of polar nano-regions was refined, and their density increased; and (ii) the intensity of the octahedral in-phase ½(ooe) tilting reflections in both [100] and $[11\bar{2}]$ SAED patterns increased, revealing that the volume fraction of a *T* phase increases. These findings support that the mechanism of enhanced piezoelectricity near the MPB in NBT-BT is due not only to polarization rotations, but also polarization extension.

Figures 3.10(a) and (b) show BF images for NBT-4.5%BT and NBT-5.5%BT. Polar nano-regions (PNR) are evident, similar to our prior data by PFM. The average size of these polar nano-regions was about 20-50nm. The size of the nano-regions for NBT-5.5%BT was smaller

than that for NBT-4.5%BT. Previous TEM studies of NBT have shown polar nano-regions of size around 50-100nm. Comparison of these prior results of NBT with the present ones (Figs.3.10a and 1b) for x=4.5 and 5.5 will show that the PNR size is reduced with increasing x at.% BT on approaching the MPB. This reduction in PNR size is more clearly shown in the higher resolution images given in Figures 3.10(c),(d), respectively. For x=5.5, the ensemble of polar nano-regions had a notably higher degree of self-organization, consistent with prior PFM studies. Such self-organization indicates that the system is able to relax its elastic energy by geometrically arranging the PNRs into improper ferroelastic domain bands.[19] Please note that this MPB boundary region (5.5<x<6.5) is where the dielectric and piezoelectric constants have been reported to be maximum.[7] Stress accommodated finer PNRs would result in a polydomain structure, which is more susceptible to electric field E. This could be manifested by changes in the PNR distribution as in an adaptive phase,[7] or by induced local phase transformations confined to regions of high twin density.[97]

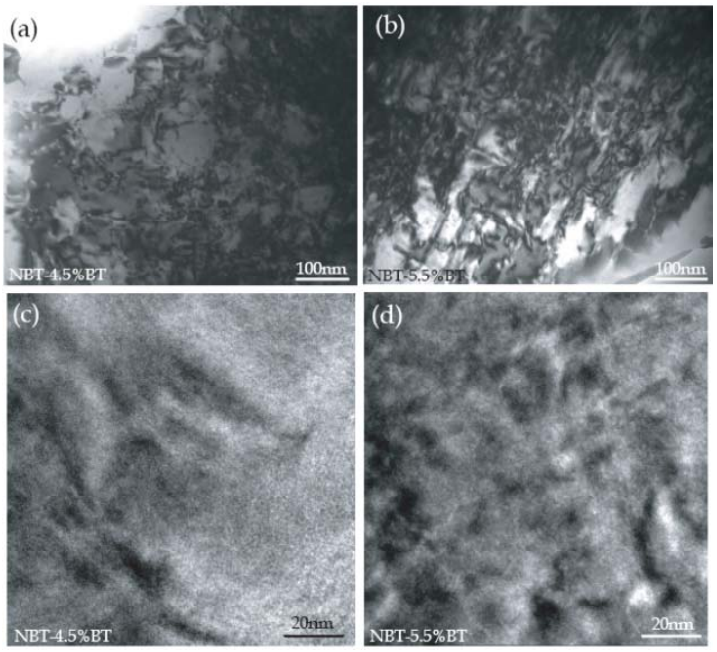

Figure 3.10. TEM bright field images of (a) NBT-4.5%BT and (b) NBT-5.5%BT, which reveal enhanced density of polar nano-regions for NBT-5.5%BT than NBT-4.5%BT. High resolution image of polar nano-regions of (c) NBT-4.5%BT and (d) NBT-5.5%BT.

Electron diffraction patterns for NBT taken along different zone axes are shown in Figure 3.11(a)-(c). For NBT-xat.%BT, the superlattice reflections are believed to originate from ½(ooo) anti-phase and ½(ooe) in-phase oxygen octahedral tiltings (where o designates odd values of the Millers indices, and e even) of limited spatial correlation,[100,101] which can be used to identify local *R* and *T* phase regions. For pure NBT, no obvious ½(ooe) superlattice reflections were found in the SAED patterns (Fig.3.11a), consistent with prior work. This indicates limited to no tendency for short-range ordered in-phase oxygen octahedral tilted regions. One can thus infer very small to no volume fraction of *T* regions on the nanoscale.[35] However, along the [110] zone, ½(ooo) superlattice reflections were notable, as marked by rings in the SAED pattern of Fig.3.11b. Figure 3.11(c) taken along the [11$\bar{2}$] zone, where both ½(ooe) and ½(ooo) reflections could be present, shows strong ½(ooo) reflections (as marked by rings), but no ½(ooe) ones. One can thus infer a high volume fraction (V_f) of anti-phase tilted regions with *R* symmetry, with little to no V_f of in-phase tilted ones with *T* symmetry. Please note that previous studies have shown that the ½(ooe) reflections of NBT become more intense in the range of 400-500 °C, where a *T* ferroelastic paraelectric phase exists.

Next, we show the effect of BT content on the ½(ooe) and ½(ooo) reflections. Figures 3.11 (d)-(f) and (g)-(i) show SAED patterns for x= 4.5 and 5.5 taken along [001], [110], and [112] zones, respectively. Relative to NBT, the intensity of the ½(ooe) reflections for NBT-4.5%BT can be seen to be increased (marked by arrows in Fig.3.11d), whereas that of ½(ooo) was decreased (marked by rings in Fig.3.11e). Furthermore, along the [112] zone, coexisting weak ½(ooe) and ½(ooo) reflections were found (as marked by arrows and rings, respectively in Fig.3.11f). These observations demonstrate that the V_f of short-range ordered in-phase tilted regions is increased with x%, and that of anti-phase tilted ones decreased. Regions of *R* and *T* symmetries on the nanoscale level coexist. Changes in the intensity of the ½(ooo) and ½(ooe) reflections continued with increasing BT content to x=5.5: as can be seen in Figs.3.11g-i taken along the [001], [110], and [112] zones, respectively. In this case, the intensity of the two superlattice reflections were nearly equal, indicating that the volume fraction of short-range ordered anti-phase tilted regions are the same.

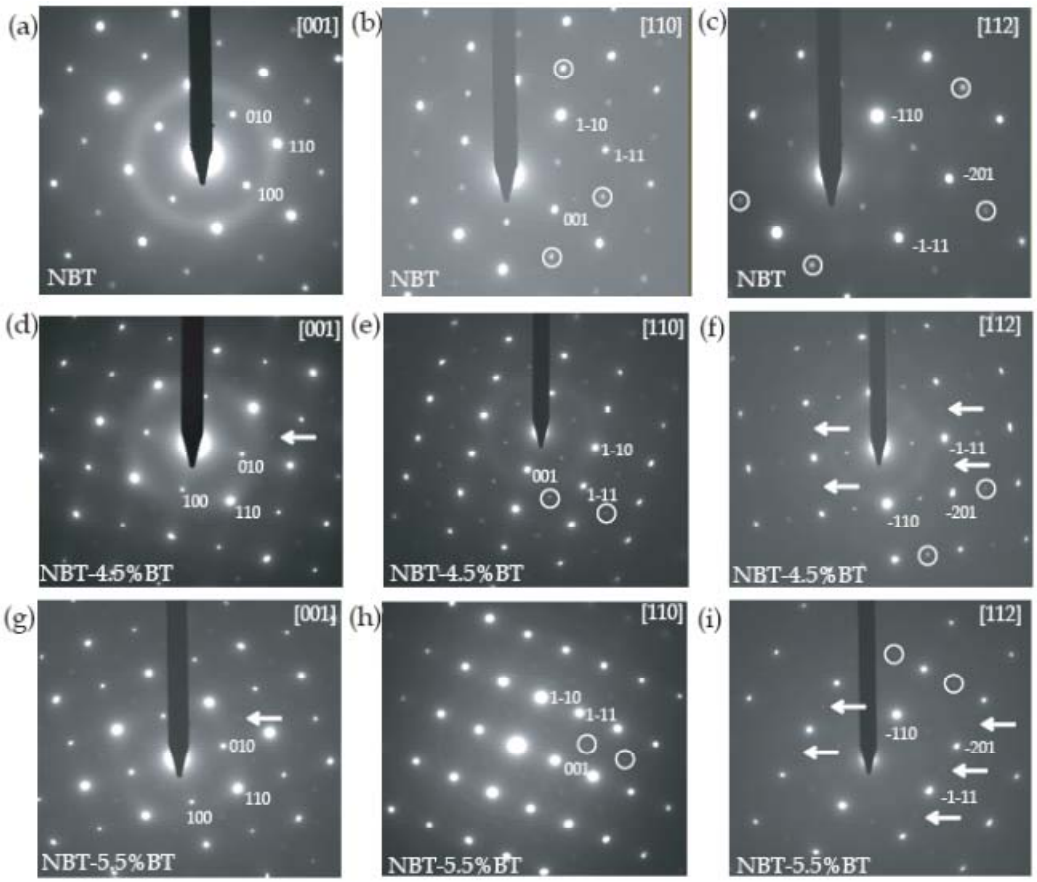

Figure 3.11 SAED patterns for NBT (a)-(c) taken along [001], [110], [112] zone axis, respectively; NBT-4.5%BT (d)-(f); NBT-5.5%BT (g)-(i), where ½(ooo) superlattice reflections are marked by rings, ½ (ooe) ones by arrows.

The question now needs to be asked about why the increased density of local tetragonal distorted regions might be beneficial to the enhancement of the piezoelectric properties for NBT-xat%BT. It has been reported that an electric field induced phase transition results in a giant strain for compositions near the MPB. The transition was initially ascribed to one between ferroelectric and antiferroelectric states under E [102-104], which remains controversial following Raman studies.[105] Soon thereafter, a field-induced transition between non-polar and ferroelectric phases was proposed,[63-65] where the nonpolar phase has a *T* structure.[63] We note that the increased density of local tetragonally distorted regions could contribute significantly to the total strain during an induced transition from non-polar to ferroelectric phases under E.

Recently, Damjanovic proposed that in addition to polarization rotation that polarization extension could result in enhanced electro-mechanical properties.[106,107] He suggested that the presence of a long-range *M* phase may not by itself guarantee enhanced piezoelectricity, but rather structural instabilities having both polarization rotation and extension contributions could be more important near the MPB.[106] With regards to NBT-x%BT, our findings of enhanced local *T* distortions (or short-range ordered in-phase oxygen octahedral tilts) within the *R* phase on approaching the MPB supports the possibility that polarization extension makes significant contributions to the total piezoelectric response. The increasing *T* volume fraction within the *R* phase on approaching the MPB would result in enhanced electrically-induced macro-strains, via polarization extension. Furthermore, with increasing temperature between 25°C and 130°C, the electrically induced strain of NBT-x%BT is increased: this could be the result of polarization extension, due to a temperature-driven phase transition.

3.2.2 Effect of Mn substitution

It has been reported that Mn substitution in NBT-x%BT crystals for compositions near the MPB can effectively increase the value of d_{33} from 280 to 480 pC/N. [11] This could be due to a more complete poling enabled by enhanced resistivity.[11] Doping is known to modify the crystal structure and improve material properties: examples include La and K in PZT [108], Sr and Ta in $NaNbO_3$ [109], and Ca and Sm in $BiFeO_3$[110-111]. Crystals of Mn-doped NBT have been reported to have: (i) enhanced resistivities, remnant polarizations, coercive fields and d_{33} values; (ii) a slight decrease in the phase transformation temperatures; and (iii) a decrease in the size of the T ferroelastic domains.[112] It is noted that the addition of Mn has little effect on the properties of NBT ceramics at room temperature:[113] which might indicate subtle differences between crystals and ceramics, possibly due to changes in stress accommodation of domains. High-resolution synchrotron XRD of both NBT and Mn-NBT have shown a broad transition range characterized by *T* and *R* phase coexistence on heating, no distinct difference found.[114]

The evolution of the domain and local structure for NBT with Mn substitution has not yet been reported. Domains make an important contribution to the dielectric, and piezoelectric properties of ferroelectric materials. Because of these advantages, PFM has been used to map the domain distributions of many ferroelectrics. [115-117]

Here, we have used PFM to map the ferroelectric domain structures for Mn-NBT, and have compared the images to those obtained for NBT. The images evidence an increased ordering of polar nano-regions by Mn. Lattice images reveal that modest additions of Mn effectively decrease the number of planar defects at the boundaries between polar regions, while favoring coexisting in-phase and anti-phase octahedral tiltings.

Figures 3.12 (a) and (b) show typical domain structures obtained by PFM for as-grown NBT and Mn-NBT. Randomly distributed polar nano-regions can be seen, as our report for NBT. For as-grown NBT, the size of the polar regions ranged from 200 to 500 nm, with many regions of much smaller size randomly distributed there within. However for as-grown Mn-NBT, the size of the polar regions was decreased to 100-200nm and the domain distribution was more uniform. The smaller size of the polar regions for as-grown Mn-NBT may help explain a previously reported enhancement in the frequency dispersion of the dielectric constant in the temperature range of 373K-473K with Mn substitution.[112] When Mn-NBT was annealed at 970K, the polar region size was found to coarsen as shown in the PFM image given in Figure 3.12 (c). These results are different than the ones of NBT, where a domain refinement was found upon annealing. These observed changes may originate from the Mn substitution and associated defect compensation, the details of which will be described in a proceeding section.

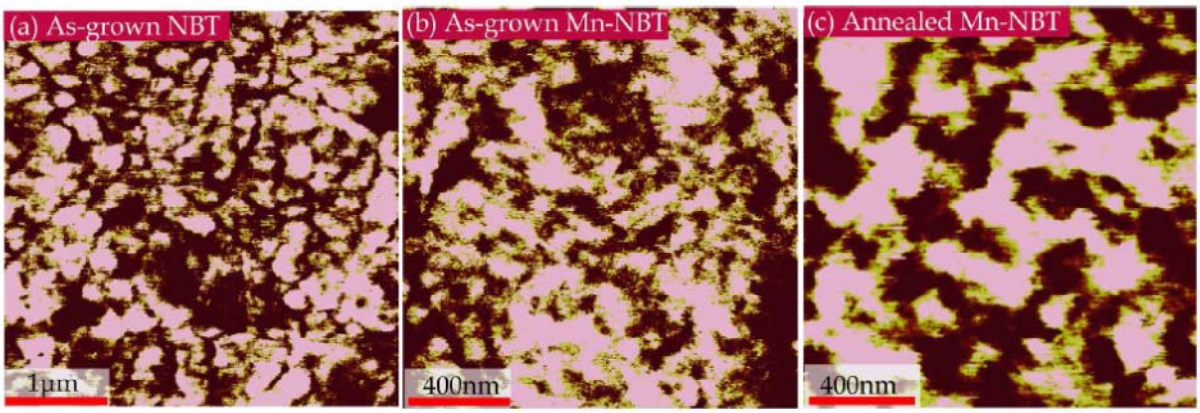

Figure 3.12 Ferroelectric domain images of (a) as-grown NBT; (b) as-grown Mn-NBT; (c) annealed Mn-NBT.

Based on these observed changes in size and distribution of polar regions, we can conclude that the degree of long-range polar ordering of NBT increases with Mn. We can quantify this observation by using a correlation function technique that has been applied to topography analysis [118], where the signal contrast (D) taken from the piezoresponse image is then proportional to the local polarization. The autocorrelation function

$$C(R_1, R_2) = \sum_{x,y} D(x, y) D(x + R_1, y + R_2) \qquad (1)$$

C is equivalent to the polarization-polarization correlation function. It has been reported that the average correlation function can then be approximated as

$$C(R) \alpha \exp[(R / \xi)^{-2h}]; \qquad (2)$$

where R is the radius, ξ is the correlation length and h a exponent parameter [108]. It is believed that ξ is directly related to the average polar region size. Thus, it can serve as a measure of the polarization disorder (or quenched random fields).[117] The averaged autocorrelation function for the three PFM images is given in Figure 3.13. It can be seen that the value of ξ increases from 36nm for pure NBT to 41nm for as-grown Mn-NBT; and upon annealing Mn-NBT, ξ was further increased to 78nm.

The valence of Mn is variable, but it is believed that the 3^+ valence of Mn in NBT is dominant. [119] Theoretically, Mn^{3+} can occupy either the B-site Ti^{4+} or an A-site vacancy. A-site occupancy is favored by considering the volatility of Bi^{3+} and Na^+. The ionic radius of Mn^{3+} is larger than that of Ti^{4+} and the resistivity is increased by up to two orders of magnitude by Mn doping, implying that the occupancy of the A-site in NBT would be preferred, suppressing the concentration of oxygen vacancies.[11] Please note that the substitution of B-site Ti^{4+} by Mn^{3+} would induce oxygen vacancy formation, which could decrease the resistivity. When Mn is incorporated onto the A sites of NBT, the concentration of oxygen vacancy is decreased as: $2Mn^{3+}$ $2Bi^{3+}$ $+3O^{2-} \leftrightarrow 2Mn_{Bi}^{\times} + Bi_2O_3\uparrow$. Accordingly, conduction would be suppressed by Mn, which should enhance the high-temperature electrical resistivity. A-site occupancy of Mn is also supported by composition analysis previously reported by Nagata and Takenaka.[120]

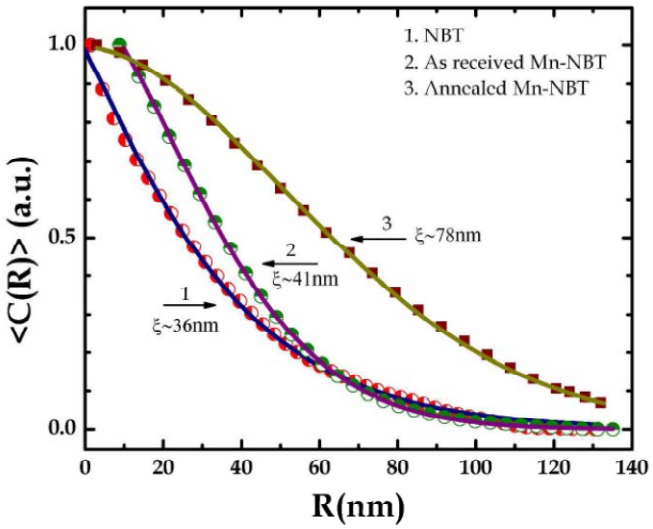

Figure 3.13 The averaged autocorrelation function for as-grown NBT, as-grown Mn-NBT and annealed Mn-doped NBT, respectively.

Since O^{2-} is large and occupies the corner of the octahedron, ionic conduction via oxygen vacancies is relatively high at moderate temperatures. These crystal chemical considerations may help explain not only the changes in the dielectric loss factors and electrical resistance, but may also provide insights into the coarsening of the polar regions by Mn substitution and subsequent annealing. Mn substitution is known to impart "hard" characteristics to PZT and PMN-PT,[121,122] due to defect pinning. Based on the symmetry-conforming property of defects in ferroelectrics, one might anticipate higher degree of polar order in systems with defects that can pin the polarization, [59,60] rather than those of the random-field type.[123]

The size of the polar regions for NBT was prone to decrease upon annealing.[113] Oxygen vacancies may be randomly quenched-in on cooling from high temperature above the phase transformation. Random fields are known to disrupt the polar order [124], favoring smaller polar domain sizes as observed in the annealed NBT. In Mn-NBT, on one hand, the Mn doping probably prefers to suppress the random-field type defects; on the other hand, a portion of the defects may be quenched-in on annealing that interact strongly with domain boundaries on cooling which pin the polarization. Then, annealing may result in the formation of extended defect structures along the domain boundaries, as previously reported for "hard" PZT.[118] This would result in large defect free regions that allow for the achievement of larger sized domain structures.

We then performed TEM and lattice imaging studies on Mn-NBT. These studies were done (i) to check whether the domains obtained by PFM reflected domain states, typical of the volume, as PFM only maps them out on the surface; and (ii) to obtain direct evidence of possible defects near the domain boundaries. First, we note that bright field images support the results by PFM. The bright field images revealed the presence of fine domain structures that were characterized by cross-hatched contrast: as shown in Figure 3.14 for Mn-NBT. The features of this nanodomain structure are similar to that observed in the PFM image. Furthermore, the TEM images reveal that the polar regions of Mn-NBT were larger than those of NBT (data not shown).

Please note that for our TEM/PFM studies, domain mapping was performed on several samples and over different regions of each sample. Comprehensive studies and analysis on two different compositions revealed that the patterns of pure NBT and Mn-NBT are different. The domain patterns shown in the manuscript are the typical ones which represent those of the Mn doped samples. Although Mn substitution is the major reason for the change of the domain, the effect of Na/Bi distribution still can not be ignored.

Next, lattice images were obtained for Mn-NBT near the nanodomain boundaries, as shown in Figure 3.15. The boundary in this figure is marked by a dashed line. The image reveals that the lattice remains coherent across the boundary: few planar defects were found. This is in difference with recent studies of NBT, where a large number of planar defects were found at the boundaries. For NBT, the elastic stress caused by the coexistence of *T* and *R* structures was believed to be partially relaxed by lifting the lattice coherency across boundaries. For Mn-NBT, there may be several reasons to explain the enhanced lattice coherency at the domain boundaries. First, the size of ferroelastic domains in Mn-NBT is decreased compared to NBT. High densities of small ferroelastic domains might more easily stress accommodate each other. Second, Mn-substitution at A sites would result in a decreased concentration of vacancies gathering at the boundaries to form planar defects that are required to lift coherency.

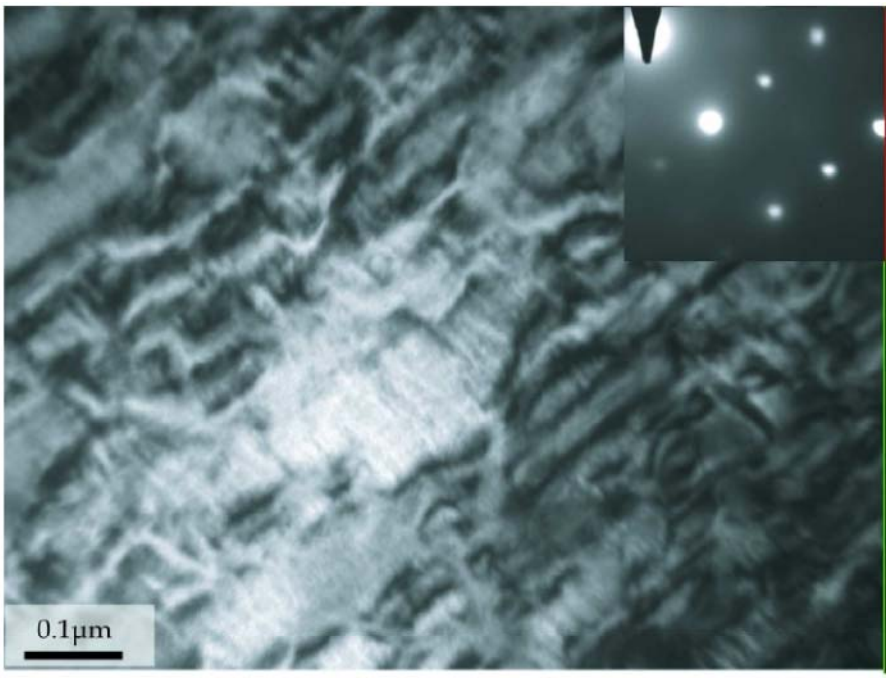

Figure 3.14 Bright field TEM image which shows nano-sized ferroelectric domains for Mn-NBT. The inset shows a SAED pattern taken along the [112] zone axis.

Figure 3.16 shows SAED patterns for Mn-NBT taken along the (a) [001], (b) [112], (c) [111] and (d) [110]. Weak ½ (ooe) reflections can be observed in Figure 3.16(a), as marked by arrows: where o designates odd values of the Millers indices, and e even. It has been noted that these superlattice reflections originate from slight deviations from the ideal perovskite structure which could have intensity contributions from: (i) oxygen octahedral tilts; (ii) chemical ordering of the A-site cations; and/or (iii) antiparallel displacements of cations [125-126]. In NBT, following theoretical [33] and experimental studies [125,126], it is believed that oxygen octahedral tilting is the dominate source of the intensity.[127]

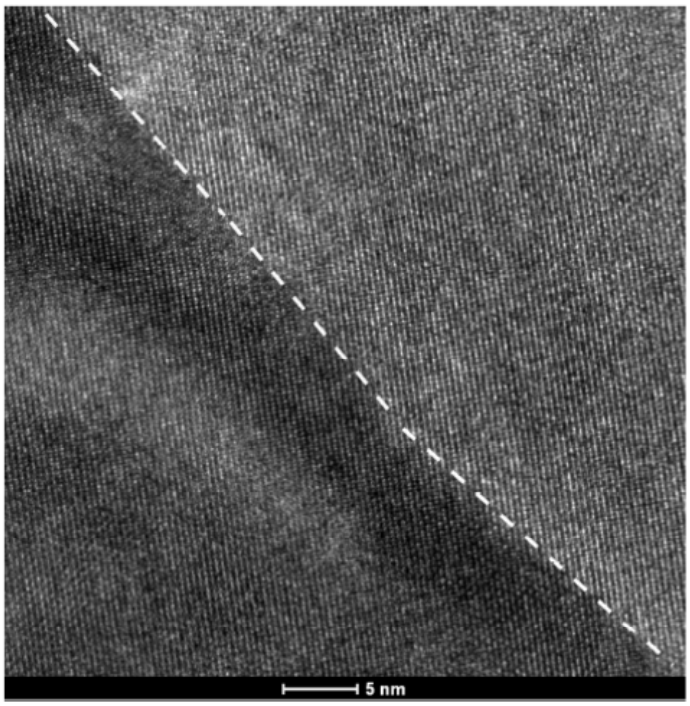

Figure 3.15 High resolution electron micrograph of Mn-NBT along the [110] projection.

Evidence of in-phase octahedral tilting in Mn-NBT at room temperature was apparent in (001) SAED patterns by weak ½ (ooe) supelattice reflections, as marked by an arrow in Figure 3.16(a). This type of in-phase octahedral tilt system generally occurs in tetragonal structures [35,125]. Whereas, rhombohedral (*R3c*) structures of perovskite often have an anti-phase ½ (ooo) octahedral tilting about the pseudo-cubic axes.[35] In Figures 3.16 (b) and (d), ½(ooo) reflections were found as marked by circles. It is worth to note that ½ (ooe) reflections were also observed along [110], as marked by arrows in Fig. 3.16 (d): indicating coexisting in-phase and anti-phase tiltings in Mn-NBT. However, no such ½ (ooe) reflections were apparent along [111] and [112]. The structure of NBT in the temperature range of 5-528K has been reported to be single phase *R*, with an anti-phase ½ (ooo) octahedra tiling. However in-phase ½ (ooe) octahedral tilts are known to become prominent between 528-800K.[125] Dorcet et al. [26,27] proposed in this higher temperature range that *T* and *R* phases coexist, which have two different types of tilts (i.e., in-phase and anti-phase) that need to be accommodated. It should be noticed that in the [011] zone axis pattern of their work, the expected ½ (ooe) extra spots of the *T* phase were not observed: this implies a systematic extinction corresponding to a glide plane.

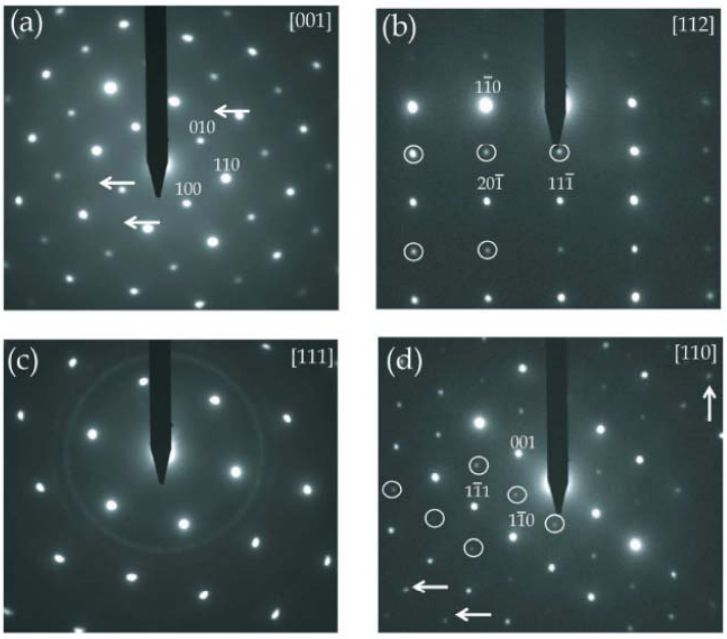

Figure 3.16 (a)-(c) SAED patterns of Mn-NBT taken along the (a)[001],(b) [112],(c) [111], and (d) [110]. The arrows indicate the possible ½ (ooe) super-reflections from in-phase octahedral tilting and the circles show the ½ (ooo) super-reflections from anti-phase octahedral tilting.

However, in the [011] zone axis pattern for Mn-NBT, the expected ½ (ooe) extra spots were indeed observed, as marked by arrows in Figure 3.16(d). This indicates that glide planes in Mn-NBT are present, and that tetragonal in-phase tilting has become more pronounced. This can also be explained by the Goldschmidt tolerance factor:[127]

$$t = \frac{R_A + R_O}{\sqrt{2}(R_B + R_O)};$$

where R_A, R_B, and R_O are ionic radii of A and B cations and oxygen in ABO_3 perovskite structure, respectively. Compounds in the perovskite family are found to exist over the tolerance factor range $1.05 > t > 0.78$.[127] An in-phase tilting distortion generally has a smaller value of t than anti-phase ones. It is known that Mn substitution is incorporated onto the A sites and that the ionic radius of Mn^{3+} (0.65 Å) is significantly smaller than Bi^{3+} (1.28 Å) or Na^{+} (1.39 Å): this could decrease the value of t and accordingly suppress anti-phase rotations, producing slightly more intense ½ (ooe) reflections.

Due to the weak intensity of in-phase ½ (ooe) super-reflections in Mn-NBT, it was extremely difficult to study ½ (ooe) one using HRTEM. Accordingly, only the octahedral anti-phase ½(ooo)

superlattice reflections were investigated. A lattice image for Mn-NBT taken along the [110] zone axis, and the corresponding power spectrum, are shown in Figure 3.17(a). ½ (ooo) superlattice reflections were obvious in the power spectrum, as marked by dashed circles. In order to obtain more detailed information about the anti-phase tilts, inverse Fourier transforms of these super-reflections were obtained. The corresponding image is shown in Figure 3.17(b). In this image, lattice clusters of size 3-8nm can be seen. It can be inferred that the ½ (ooe) in-phase tilted domains for Mn-NBT would be of similar or smaller size, but notably lower density. The enhanced ferroelectric ordering and in-phase octahedral tilting may help explain the enhanced piezoelectric properties of NBT with Mn.[112]

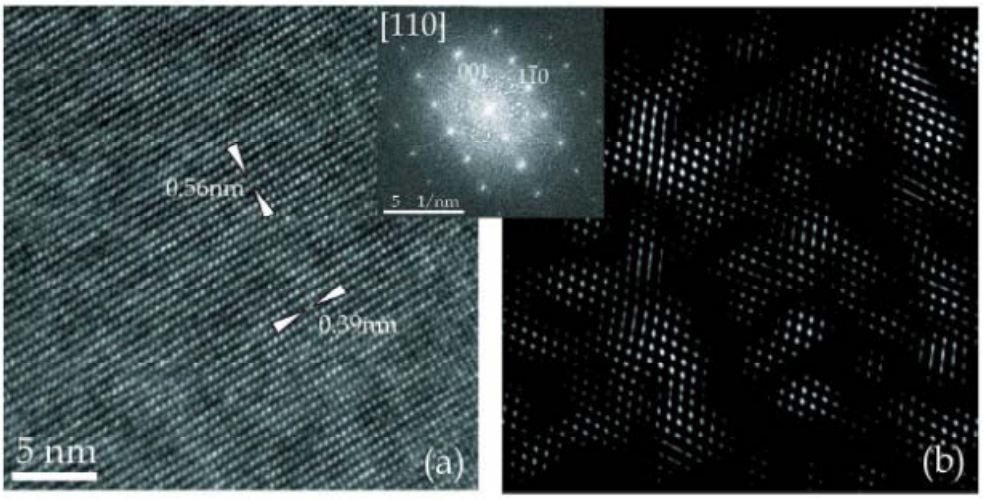

Figure 3.17 (a) High resolution electron microscopy image of Mn-NBT along the [110] projection; (b) inverse Fourier transform of the super-reflections of image (a). The inset shows the power spectrum of the lattice image in (a) in which weak ½ (ooo) super-reflections were observed.

The doping effect becomes more obvious near the MPB. Here, we have studied the domain structure, octahedral tilting, and lattice structure of NBT-x%BT and Mn:NBT-x%BT with x=5.5 using bright field and lattice imaging, and SAED. We find with Mn substitution: (i) increased tendencies of ferroelectric ordering and in-plane octahedral tilting; (ii) formation of structural modulation across domain boundaries, which may help relax elastic stress between ferroelectric

domains; and (iii) an increase in the number of in-phase oxygen tilted regions, with a size of about 2 to 8 nm and with a tendency of alignment along {110}.

Figures 3.18(a) and (b) show bright-field images for NBT-x%BT and Mn:NBT-x%BT with x=5.5, respectively. Two types of domain structures can readily be discerned. For NBT-5.5%BT, polar nanodomains are clearly evident. The average size of these polar nanodomains was about 20-50nm. Prior studies of pure NBT single crystal have shown a polar nanodomain size of 50-100nm, thus it appears that the polar nanodomain size is reducing with increasing x at% BT on approaching the MPB. Upon Mn substitution, the morphology of these domains was notably changed. More highly ordered domain structures became evident, which were aligned along {110}. It is worth noting that similar types of domains have been found on the tetragonal side of the MPB for PMN-x%PT: i.e., the so-called normal micron-sized *T* domains.[128] However, there are two notable differences of the domain state between Mn:NBT-5.5%BT and the T phase of PMN-PT, which are: (i) Mn:NBT-5.5%BT displays relaxor ferroelectric features, not normal ferroelectric ones[11]; and (ii) the stable crystal structure in Mn:NBT-5.5%BT was R, where as that of PMN-x%PT was *T*. Clearly, the development of micron-sized domains in Mn:NBT-5.5%BT is due to Mn substitution. We can ascertain this from the fact that there were no changes in crystal structure for NBT-5.5%BT with Mn based on our x-ray studies. Furthermore, this infers that the change in domain stability arise due to changes in defect distributions and their interaction with domains. Figures 3.18(c) and (d) show lattice images obtained near domain boundaries for NBT-5.5%BT and Mn:NBT-5.5%BT, respectively. For NBT-5.5%BT, planar defects along {110} twin boundaries can be seen, as previously reported for NBT. However, for NBT-5.5%BT, the lattice planes were found to be tilted with respect to each other across this boundary, as illustrated by dashed lines in the figure and by a higher resolution image shown in the insert of the figure. This tilt clearly shows that the lattice is elastically relaxed across the boundary. For Mn:NBT-5.5%BT, the lattice was found to be coherent across the boundaries, as can be seen in Fig.3.18(d), also the inset of the figure. In this case, the lattice planes of different regions were not found to exhibit a tilt with respect to each other. Clearly, Mn substitution not only makes significant changes in the polar domain structure and superlattice reflections, but also to the mechanism of stress accommodation between octahedral tilt regions.

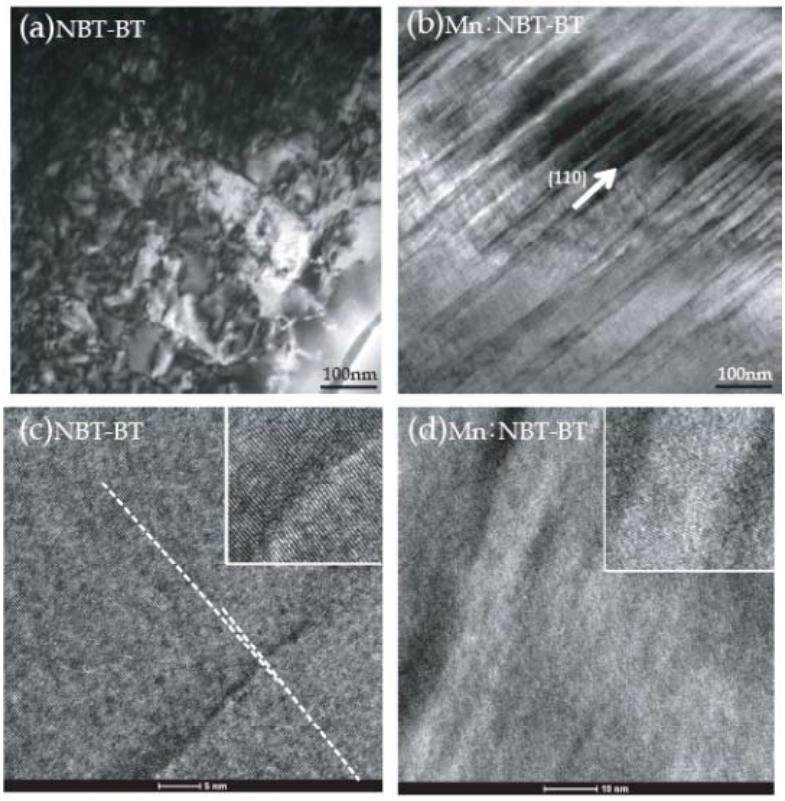

Figure 3.18 TEM bright field images of (a) NBT-5.5%BT and (b) Mn:NBT-5.5%BT, which reveal enhanced ferroelectric ordering for NBT-5.5%BT with Mn substitution; lattice images taken across octahedral tilt boundaries for (c) NBT-5.5%BT, and (d) Mn:NBT-5.5%BT, the insets show the magnified region across the boundaries.

An electron diffraction pattern for NBT-5.5%BT taken along [001] is shown in Figure 3.19(a). Weak ½ (ooe) superlattice reflections can be seen, as marked by arrows: where o designates odd values of the Millers indices, and e even. These finding are consistent with prior reports for NBT-5.5%BT ceramics.[129] It is believed that these ½ (ooe) reflections originate from oxygen octahedra tilts in the NBT-5.5%BT system of limited spatial correlation [25,27-33]. These small tilted regions may have a local tetragonal distortion within the average *R* structure. For Mn:NBT-5.5%BT, SAED patterns taken along [001] and [110] are shown in Figures 3.19 (b) and (c), respectively. These patterns clearly revealed intense ½ (ooe) and weak ½ (ooo) reflections as marked by arrows and rings, respectively. These results show that a coexistence of in-phase ½ (ooe) and out-of-plane ½(ooo) octahedral tilted regions is stabilized by Mn substitution, this is indicative of a mixture of *R* and *T* phases. It is noted that an orthorhombic (O)

perovskite phase can also exhibit both superlattice spots simultaneously.[116] For NBT, the orthorhombic phase was only observed near 230°C, bridging between *R* and *T* ones.[26,27] To date, no *O* phase in NBT-based solution has been observed at room temperature, either by TEM or X-ray studies. Therefore, the possibility that these superlattice are due to an orthorhombic phase in Mn:NBT-BT can be reasonably excluded. The strong intensity of the in-phase tilts with Mn may indicate an enhanced local tetragonal distortions within the *R* phase, which is coincidental with a significant enhancement of d_{33} with Mn.[11]

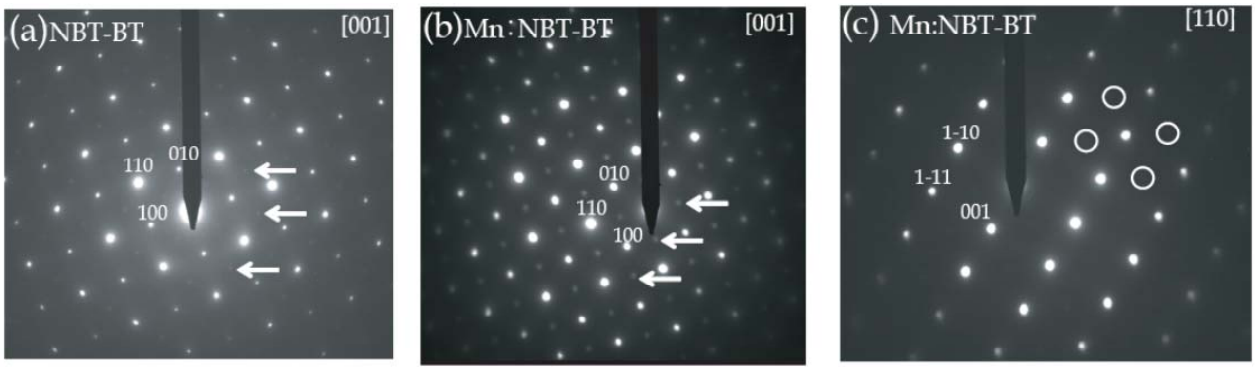

Figure 3.19 SAED patterns for (a) NBT-5.5%BT taken along the [001] zone axis; (b) and (c) Mn:NBT-5.5%BT along [001] and [110] zone axis, respectively, where intense ½ (ooe) superlattice reflections can be seen in (b) as marked by arrows.

Lattice imaging was then performed on Mn:NBT-5.5%BT near the edge of the specimen along the [001] zone axis. The edge was chosen so that we could try to observe the lattice planes in areas of the sample which had thicknesses on the order of the spatial coherence of the ½ (ooe) octahedral tilts. Figure 3.20(a) shows such a lattice image and the inset shows a fast Fourier transform (FFT). The FFT reveals intense ½ (ooe) reflections from in-phase octahedra tilts, consistent with the SAED patterns in Fig.3.19(b). However, a FFT of similar images for NBT-5.5%BT did not reveal such ½ (ooe) reflections, consistent with a much weak intensity in the SAED pattern. In Figures 3.20(b), we show the corresponding inverse FFT image obtained by selecting only the ½ (ooe) super-reflections of the FFT. It clearly reveals a high intensity of small octahedral tilt regions of size 2-8nm, consistent with a prior report for NBT-BKT-BT ceramics near the MPB.[130.131] By comparing the intensity of the ½ (ooe) reflections between NBT-

5.5%BT and Mn:NBT-5.5%BT, one can infer that Mn pronouncedly increases the number of in-phase tilted regions.

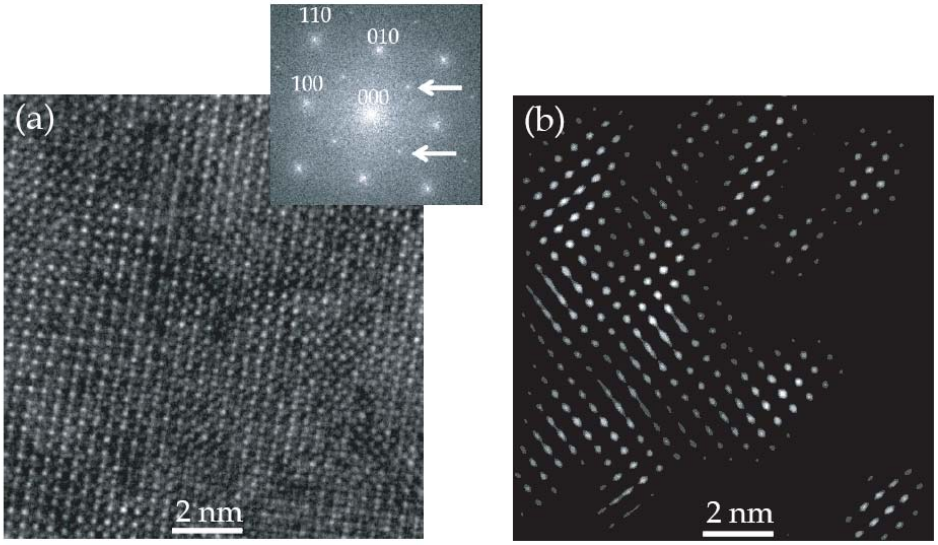

Figure 3.20 (a) Lattice image for Mn:NBT-5.5%BT taken along the [001] zone axis, and the inset shows power spectrum of the lattice image , which reveals ½ (ooe) super-reflections; and (b) corresponding inverse FFT image obtained using only the ½ (ooe) superlattice spots.

3.3 Mesoscopic dynamic heterogeneity

Investigations of the polarization dynamics of relaxor ferroelectrics and associated domain features has been the subject of research for a long time.[132] Relaxor behavior is characterized by the presence of polar nanodomains and frequency dispersion in the dielectric constant.[133] The relaxation time distribution has been shown to extend over many decades, near and below a characteristic freezing temperature.[133] Furthermore, macroscopic electrical measurements do not measure the switching dynamics of individual polar regions on the nanoscale.[134] Domains are well known to interact with defects of the random field (resulting in a breaking of the translational invariance of the polarization[135]) and of the mobile (resulting in pinning of boundaries[136]) types. Previous investigations of La-modified PZT [136] have shown under moderate amplitude AC electrical fields (E_{ac}<1kV/cm) significantly below the coercive field (E_c≈4-5kV/cm) that normal micro-size ferroelectric domains typical of a normal ferroelectric long-range ordered state are broken down into polar nano-domains typical of a relaxor. Correspondingly, dielectric measurements with increasing E_{ac} demonstrated that a dispersive

dielectric response was induced from a dispersionless one. These previous studies show that polarization reversal can occur by switching via nanodomain inhomogeneities, rather than by the motion of conventional ferroelectric domain boundaries.

NBT-x%BT is known to have relaxor ferroelectric characteristics [11] in its *R* or pseudocubic phase. The dynamic domain behavior and nucleation-growth mechanism during polarization reversal are key issues which remain unknown for NBT-x%BT.[132] These issues are potentially important to understanding enhanced piezoelectricity in Pb-free systems. Significant interest in theoretical and experimental studies of polarization dynamics at the nanoscale has been advanced satisfactorily by the development of SSPFM. This technique offers a number of approaches to the fundamental understanding of ferroelectric materials, including: imaging of nucleation centers on free surfaces, nucleation mechanisms, and domain wall dynamics.[132,68-70] It offers a good tool to investigate the polarization dynamics of NBT-x%BT surfaces including the polarization switching mechanism, domain nucleation process, and statistical studies of the switching behavior. Such investigations have previously not been reported for NBT-x%BT. High quality crystals of NBT-x%BT offer a defect-free subject for such a study, eliminating the effect of grain boundaries and polycrystallinity which complicate these processes. For example, it is known that the evolution of the strain state near grain boundaries results in a change of polarization.[135-137] Furthermore, information concerning polarization dynamics obtained from NBT-x%BT crystals could also be applied to understand the behavior of its ceramics or thin film forms. Here, we utilize the band excitation version of PFM spectroscopy (BEPS) in SSPFM experiments, the hysteresis loops were acquired on a grid of points, providing spatially resolved information of the switching behavior.

3.3.1 Domain structures

The domain structures of NBT-4.5%BT, NBT-5.5%BT and Mn:NBT-5.5%BT obtained by band-excitation mode are shown in Figure 3.21 and Figure 3.22. For NBT-4.5%BT, the domain structures exhibited a well-defined labyrinthine shape with an average length of less than 1μm (shown in Figs.3.21a and 3.21b). It should be noted that the domain boundaries were relatively rough. This is more obvious in the higher resolution images (see images Fig.3.22a and 3.22b), which demonstrate that there is an assembly of polar nano-regions into platelets at the boundaries.

The labyrinthine domain pattern is indicative of a local deviation of the surface symmetry from cubic.[82]

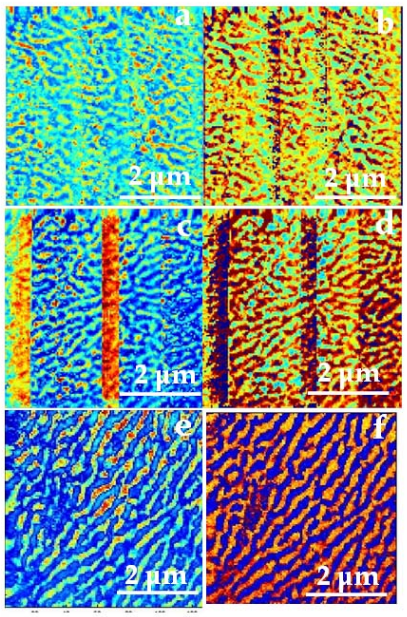

Figure 3.21 Domain structures of NBT-4.5%BT (a-b); NBT-5.5%BT (c-d); and Mn:NBT-5.5%BT (e-f).

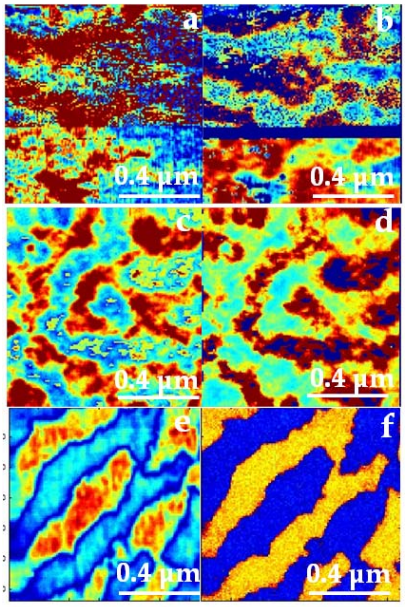

Figure 3.22 High resolution domain structures of NBT-4.5%BT (a-b); NBT-5.5%BT (c-d); and Mn:NBT-5.5%BT (e-f).

With increase of the BT content to x= 5.5 at.%, the length of the domains was increased but their widths were decreased, as can be seen in Figs. 3.21c to 3.21d, more obvious in the higher resolution images (see images Fig. 3.22c and 3.22d) These changes resulted in a stripe-like morphology, as the MPB region was approached, with an orientation along the <110>. Such a tendency towards enhanced self-organization of polar-regions into stripe-like domains was more pronounced for Mn:NBT-5.5%BT, as can be seen in the images of Figures 3.21e and 3.21f. In this case much finer stripe-like domains with smooth boundaries were apparent that were oriented along <110>, as shown in Fig. 3.22e and 3.22f.

The contrast contours in the domain structures for all three compositions exhibited irregularities. These non-uniformities reflected the presence of polar nanoregions that existed within the larger scale domain structures. Similar Hierarchical domains with internal irregularities have previously reported in PMN-x%PT crystals for compositions close to their MPB. Such Hierarchical domain structures self-assemble due to elastic accommodation that achieves the invariant plane strain, similar to martensitic transformations. It is important to note in Figure 3.21 the significant enhancement in self-assembly of domains with small changes in BT and Mn contents as the MPB is approached near x=6 at%. This is suggestive of an important role of changes in the distribution of polar nanodomains under field within the larger domain plates on the enhanced piezoelectric properties of NBT-x%BT at the MPB: such adaptive ferroelectric domain features have previously been proposed for Pb-based MPB systems.[73]

3.3.2 Polarization dynamics

The purpose of spatially-resolved spectroscopy is to obtain insight into the spatial distribution of polarization dynamics and relaxation behavior, and their relationship with domain structures. A detailed theoretical description of spatially-resolved spectroscopy has been given in the literature.[132] The approach could be important to understanding NBT-x%BT if the higher resolution PFM images with self-assembly of polar nano-regions into longer domain structures could be correlated with spatial and/or temporal non-uniformities. For example, it would be interesting to determine whether the domain boundary confine the polarization dynamics and relaxation behavior to be inside the domains or not, as the average polarization inside the boundary is supposed to be the same for conventional ferroelectrics.

Figure 3.23 shows the results from the SS-PFM study of Mn:NBT-5.5%BT. Parts (a) and (b) show the surface topography and corresponding ferroelectric domains (amplitude), taken on a $1\times1\mu m^2$ area. Part (c) shows a map of the switchable polarization taken across the same region. Representative hysteresis loops obtained at several positions across the scanned area are shown in (d), which demonstrate similar switching behavior for the various regions. The consistency of these curves shows that the spatial variation of the saturated polarization is not that long.

Detailed polarization switching parameters obtained from the same region are shown in Figure 3.24. These figures show the full set of BEPS maps, extracted from fitting the experimental hysteresis loops to a model. In SS-PFM, local hysteresis loops are collected at each point on a $N\times M$ mesh. The specific parameters taken in both forward and reverse directions are the coercive voltages (V^+ and V^-), nucleation voltages (V_c^+ and V_c^-), and remanent and saturated responses (R_0^+, R_0^-, R_s^+, and R_s^-). The work of switching is defined as the area within the loop. The imprint bias and switchable polarization are defined as $I_m = (V^+ + V^-)/2$ and $R_m = R_s^+ - R_s^-$, respectively.[69]

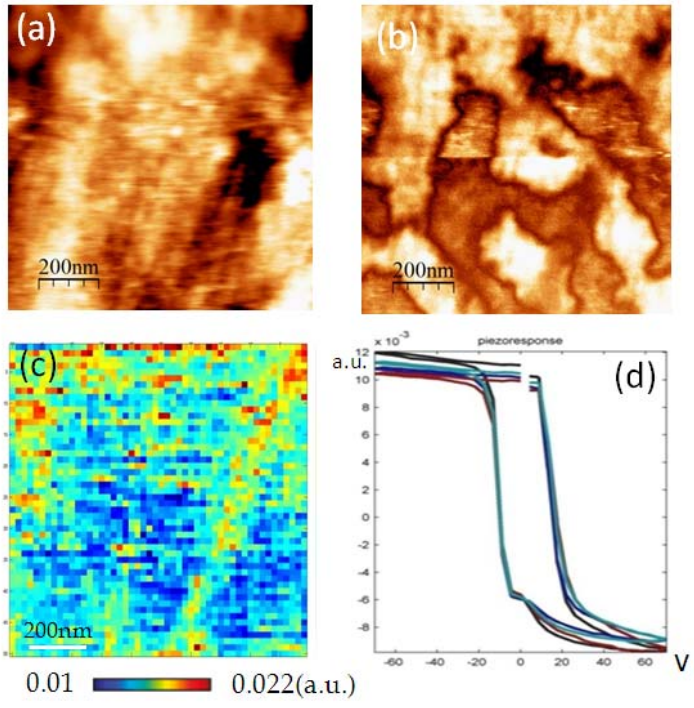

Figure 3.23 (a) and (b): surface topography and corresponding ferroelectric domains (amplitude) of Mn:NBT-5.5%BT; in (c) shows the map of switchable polarization across the same region. The hysteresis loops extracted from several locations are shown in (d).

The contour of the imprint bias can be seen in Figure 3.24 to be non-uniform, indicating that shape of the polarization curves should not be similar to each other. Although the P-E loops of Fig. 3.23d provide some information for a few number of regions, the contours of nucleation voltages, coercive voltages and remanent polarization provide a better comparison. In Figure 3.24, a variation on the scale of 50-200nmn from region to region is evident, evidencing a heterogeneity. Similar variability in the contours of the switchable polarization and work of switching were also seen. These 50-200 nm sized heterogeneities were not only confined to domain walls. But rather, they also existed within domains, as there were smaller characteristic regions having similar values of spontaneous polarization as the bulk average. The underlying cause of the heterogeneities maybe due to the fact that activation energy barrier of the initial polarization state before application of bias was low, and thus it was easy to overcome under electric field.

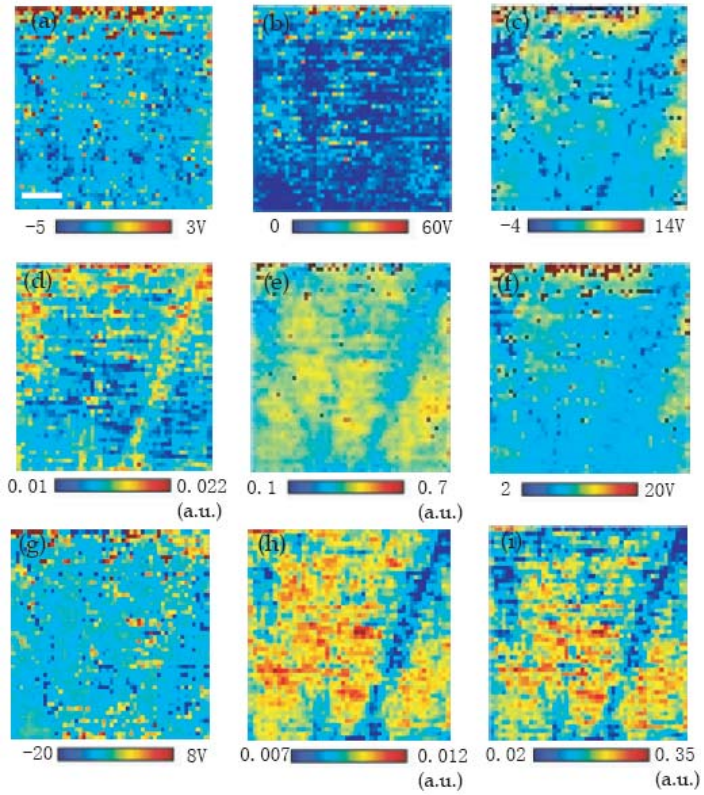

Figure 3.24 BEPS maps of Mn:NBT-5.5%BT: (a) imprint, (b) positive nucleation bias, (c) negative nucleation bias, (d) switching polarization, (e) work of switching, (f) positive coercive voltage, (g) negative coercive voltage, (h) positive remanent polarization, (i) negative remanent polarization.

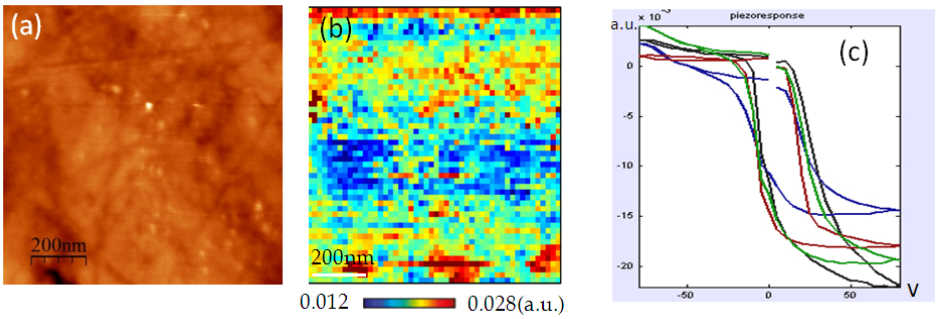

Figure 3.25 (a) surface topography and corresponding map of switchable polarization across the same region for NBT-5.5%BT. Hysteresis loops extracted from several locations are shown in (c).

A polarization heterogeneity was also apparent for NBT-5.5%BT, as can be seen in Fig. 3.25b. Inspection of this figure will reveal that the polarization heterogeneity was more pronounced, than that for Mn:NBT-5.5%BT. The surface topography for NBT-5.5%BT is shown in Figure 3.25a, which was very flat with no obvious scratches. Accordingly, the effect of surface irregularities was minimized, and the observed variation in the polarization behavior can be attributed to a structural heterogeneity. Hysteresis loops extracted from the image for NBT-5.5%BT are shown in Figure 3.25c, which confirmed that the P-E curves are much more spatially variable than for Mn:NBT-5.5%BT. Each of these piezoresponse curves had well-defined ferroelectric-like shapes. Detailed polarization parameters for this same region of NBT-5.5%BT are given in Figure 3.26, which displays the full set of BEPS maps. These data demonstrate the presence of a 100-200 nm sized heterogeneity, which again was independent of the domain boundaries. From the contours of imprint bias, work of switching and switchable polarization, it can be seen that their distributions were wider than those for Mn:NBT-5.5%BT, as also evidenced by the larger variability in the P-E curves (see Fig. 3.25c). The contour of nucleation voltages, coercive voltages and remanent polarization further displayed a wider variability from region to region for NBT-5.5%BT relative to Mn:NBT-5.5%BT.

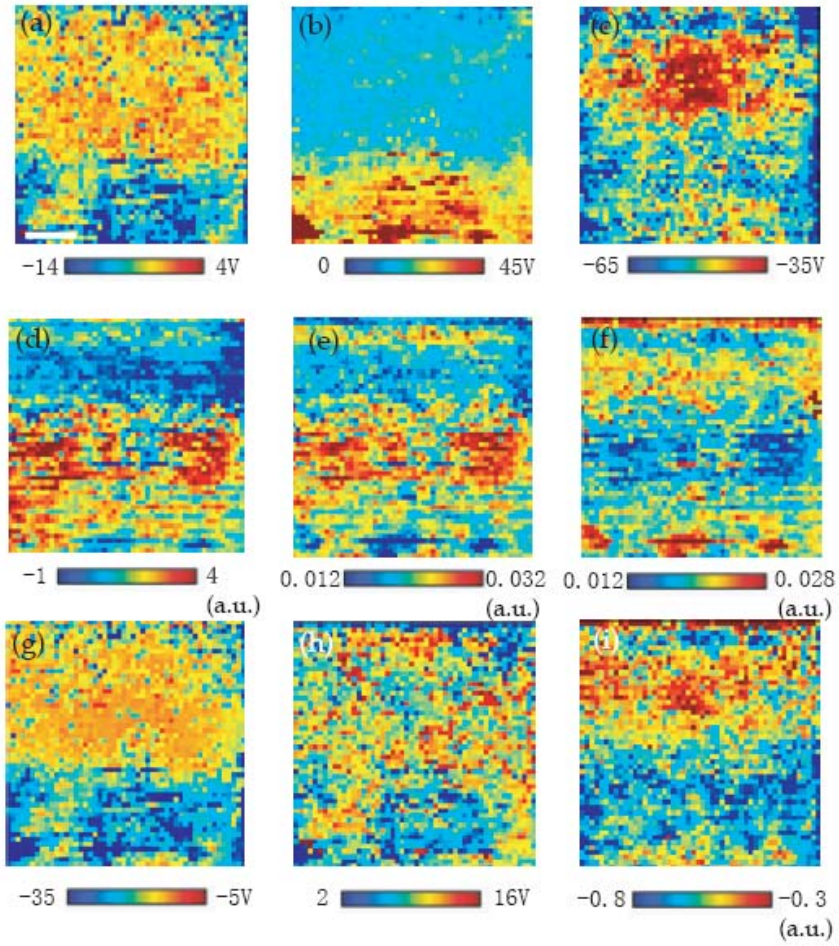

Figure 3.26 BEPS maps of NBT-5.5%BT: (a) imprint, (b) positive nucleation bias, (c) negative nucleation bias, (d) positive remanent polarization, (e) negative remanent polarization (f) switching polarization (g) negative coercive voltage, (h) positive coercive voltage, (i) work of switching. Scale bar is 200nm.

Corresponding histograms of PCF and NCF, PNB and NNB, and remnant polarization (P_r) for the three compositions are given in Figures 3.27 to 3.29. It can be seen that PCF/NCF and P_r of Mn:NBT-5.5%BT were well separated each lying along a narrow range, indicating a relatively uniform value of E_c and P_r. The PNB and NNB distributions were notably wider, reflecting a relatively smaller nucleation bias. The PCF/NCF and P_r distributions for the three concentrations were different: the widths were largest for NBT-4.5%BT, less so for NBT-5.5%BT, and smallest for Mn:NBT-5.5%BT. Furthermore, the difference in voltage between the PNB and NNB distributions were respectively increased for these three compositions, as the distributions

became wider. Comparison of these results with the domain images obtained by band excitation mode (Fig. 3.21 and Fig. 3.22) demonstrates that as the domains become more self-organized and their widths smaller that distributions in histograms become narrower.

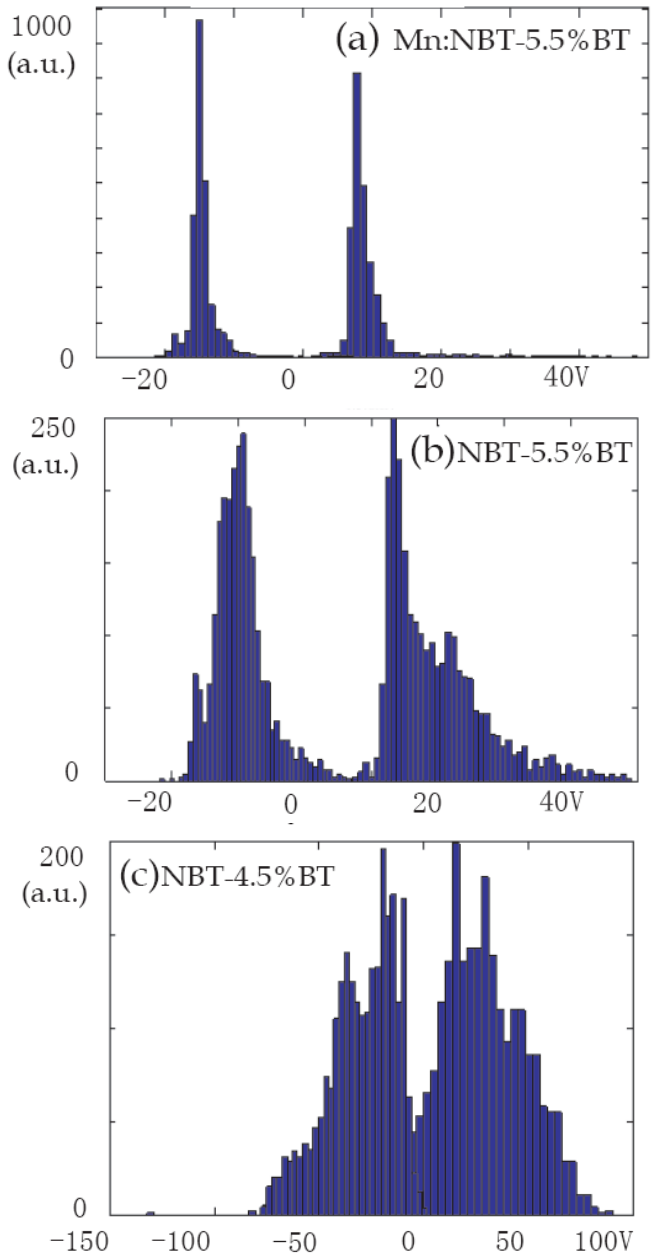

Figure 3.27 Histograms of positive and negative coercive field for (a) Mn:NBT-5.5%BT, (b) NBT-5.5%BT, and (c) NBT-4.5%BT.

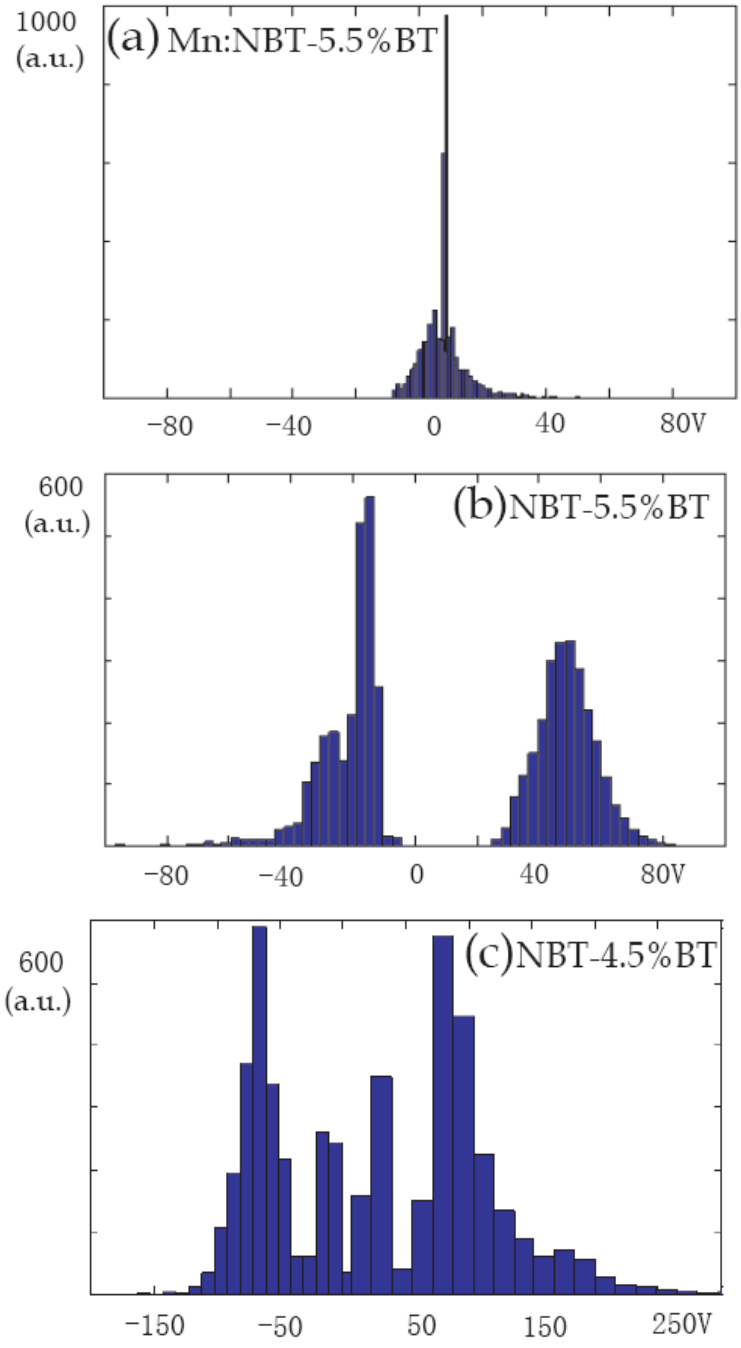

Figure 3.28 Histograms of positive and negative nucleation bias for (a) Mn-NBT-5.5%BT, (b) NBT-5.5%BT, and (c) NBT-4.5%BT.

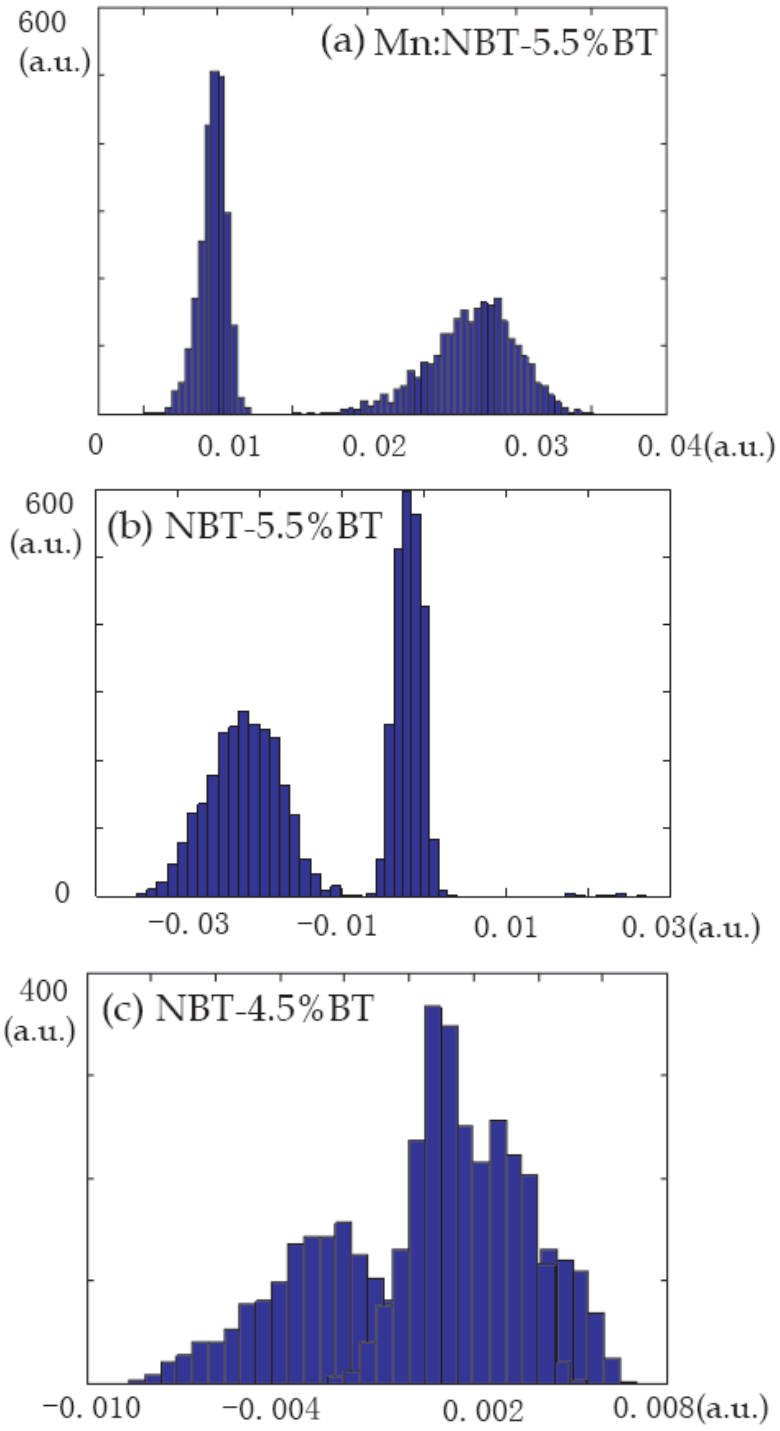

Figure 3.29 Histograms of remnant polarization for (a) Mn:NBT-5.5%BT, (b) NBT-5.5%BT, and (c) NBT-4.5%BT.

3.3.3 Relaxation behavior

Single point time-resolved relaxation was previously developed to study local retention and relaxation behavior in ferroelectrics. A strong variability of relaxation behavior between different grains of different orientations in $0.9Pb(Mg_{1/3}Nb_{2/3})O_3$-$0.1PbTiO_3$ (PMN-10PT) ceramics was reported. The relaxation process was shown to consist of two stages, the rapid initial decrease in the response and a slow (i.e., stretched exponential) decays of contrast.[138]

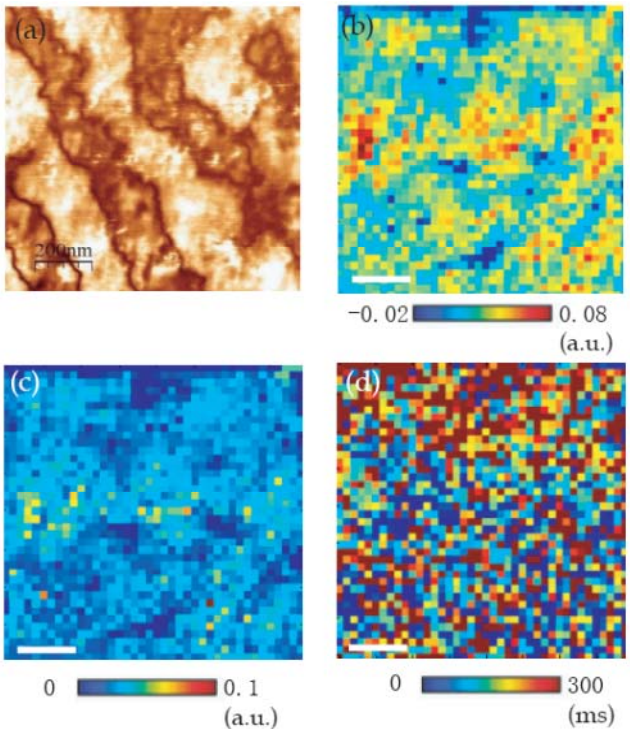

Figure 3.30 (a) Domain structures of Mn:NBT-5.5%BT of the region for relaxation measurement, (b) map of the fitted parameter A_0, polarization component using the stretched exponential law, $PR(t) = A_0 + A_1\exp^{-(t/\tau)}$ yields spatially resolved maps of relaxing, (c) map of the parameter A_1, the non relaxing component, (c) the map of relaxation time τ.

Spatially-resolved relaxation measurements provides a 3D array PR(x,y,t) of the relaxation curves at each spatial grid point: where PR is the piezoresponse signal, (x, y) is the coordinate and t is the time. An analysis of PR(x, y, t) using a functional fit f (α, t), where $\alpha = \alpha_1, \ldots, \alpha_n$ is an n-dimensional parameter vector, allows maps of $\alpha_i(x, y)$ describing the spatial variability of relaxation behavior to be constructed. As an example, the fit using the exponential law, PR(t) =

$A_0 + A_1 exp^{-(t/\tau)}$ yields spatially resolved maps of relaxing (A_1) and nonrelaxing (A_0) polarization components, and the relaxation time (τ). Alternatively, the fitting can be performed using power law or logarithmic function.[133]

A relaxation mapping of Mn-NBT-5.5%BT is shown in Figure 3.30. The stripe-like domain structure of the same region taken by PFM is shown in Fig. 3.30a. The fitting parameters are then given in Figures 10b-d. The values of A_0 (Fig. 3.30b) and A_1 (Fig.3.30c) can be seen to be on order of 50-100nm. This demonstrates that the size of the relaxing and non-relaxing polarization are both small. Clearly, these regions are much smaller than the size of the domain revealed by the PFM image. The findings demonstrate that the dynamical response of the Mn:NBT-5.5%BT crystal to an electric field does not occur at the domain boundaries, but rather on a much finer scale by a spatial inhomogenous processes. Furthermore, please note in Figure 3.30d the strong spatial dependence of the relaxation time distribution contour. These results clearly demonstrate the presence of a strongly inhomogenous phenomenon both in space and time. Representative relaxation curves of Mn:NBT-5.5%BT are shown in Figures 3.31a and b. They were fit using the function of $PR(t) = A_0 + A_1 exp^{-(t/\tau)}$. It can be seen that the fitting is good and that the value of relaxation time τ lies in the range of 90-270ms. Similar curves for NBT-5.5%BT are shown in Figures 3.31c and d, where τ lies in a narrower range of 70-120ms. From this comparison, we can conclude that Mn-NBT-5.5%BT has a broader relaxation time distribution.

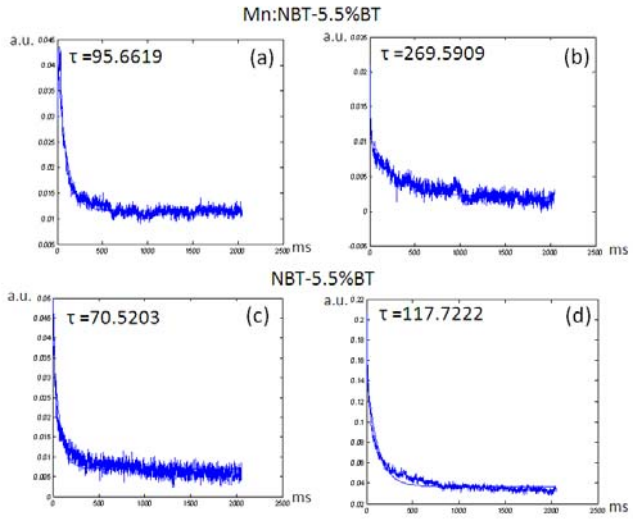

Figure 11

Figure 3.31 Typical rough relaxation data with fitted curves, (a) and (b) Mn:NBT-5.5%BT, (c) and (d) NBT-5.5%BT.

Our findings of a spatial and temporally inhomogenous polarization under excitation by SS-PFM give evidence of polarization switching by units that are much smaller than conventional macrodomains and that are not confined to regions near domain boundaries. This is consistent with switching by a random-field condition. In this case, relaxation-like state maybe induced under large amplitude reverse bias/drive from a poled condition. Before conventional domain boundary motion can be excited, the macrodomains breakdown and switching occurs by the internal polar non-uniformities whose existence is determined by quenched random fields. This maybe a natural consequence of the macrodomain plates being stabilized by the elastic accommodation of the polar nanoregions. Under reverse bias, as individual nuclei begin to reverse, strain accommodation of a colony of PNRs might not be fully achieved. This would tend to thermodynamically destabilize the macrododomain plates, unless the invariant plane strain can rotate.

A second issue is the effect of the coexistence of different octahedral tilted regions. It has been reported that a small amount of tetragonal platelets originating from in-phase oxygen octahedra tilts enhancces properties, where tetragonal phase volume fraction increases with x%BT. Mn substitution has been found to favor in-phase oxygen octahedral tilting.

3.4 Summary

Phase transformation and domain studies of NBT have revealed (i) that a high-temperature tetragonal ferroelastic domain structure is elastically inherited into a lower temperature rhombohedral ferroelectric phase; and (ii) that polar microdomains form within this geometrical constraint on cooling, resulting in a metastable state with attributes of a relaxor ferroelectric.

Our study shows that the addition of $BaTiO_3$ to NBT (i) refines the size of polar nano-regions and enhances their self-organization; and (ii) suppresses formation of proper ferroelastic domains at high temperatures in the paraelectric state, and rather favors the formation of improper ones that form below the ferroelectric Curie temperature that elastically accommodate the ferroelectric ones.

The domain structure and octahedral tilting of NBT-x%BT for x=0, 4.5, and 5.5 were studied by TEM. We find with increasing x: (i) a refined size of polar nano-regions and an enhanced self-organization, and (ii) an increased intensity of the octahedral in-phase tilt ½(ooe)

reflections and a decrease in the anti-phase ½(ooo) ones. This reveals that the volume fraction of the T phase increases with increasing x as the MPB is approached. The findings support that the mechanism of enhanced piezoelectricity for NBT-x%BT near the MPB has both polarization rotation and polarization extension contributions.

The ferroelectric domain structures of pure NBT and 1at.% Mn-doped NBT (Mn-NBT) single crystals were investigated by PFM. The correlation length of the polar clusters was found to increase from 36nm (NBT) to 78nm (Mn-NBT, annealed). In addition, SAED revealed ½ (ooo) octahedral tiltings for NBT. Coexisting in-phase ½ (ooe) and anti-phase ½ (ooo) tiltings were found on Mn substitution. Near the MPB, small amount of Mn substituents favor the formation of micro-sized ferroelectric domains in the *R* phase field, which contains a high density of ½ (ooe) octahedral tilted regions that may have tetragonal distortions of limited spatial lengths. Such local structurally inhomogenous states that coexist over different length scales may help explain the large induced strain as high as 0.6% and enhanced d_{33} values in Mn substituted NBT-5.5%BT crystals near the MPB.

The domain structure of $Na_{0.5}Bi_{0.5}TiO_3$-$BaTiO_3$ crystals near the morphotropic phase boundary was mapped by band excitation PFM: 10-50nm sized heterogeneous regions were observed within a 200nm sized domain structure. An inhomogeneous chemical composition and local asymmetry may account for the unusual multi-scale heterogeneity of this domain structure, representing isolated polar nanoregions inside of larger domain organizations. The spatial homogeneity of the polarization switching and the relaxation behavior near the surface were then investigated using three dimensional time-resolved spectroscopic PFM. The distribution of this heterogeneity was not found to be relevant to the domain morphology.

Note: this chapter is part of my published work from references [150-155].

Chapter 4 Aging associated domain evolution in $(K_{0.5}Na_{0.5})NbO_3$ textured ceramics

The significant increase of piezoelectric coefficients in <001> textured KNN ceramics compared to random ceramics is due to the enhanced ordered distribution of grain orientations along <001>. It is known that ferroelectrics with engineered domain configurations exhibit drastically enhanced piezoelectric responses along nonpolar axes.[139] The <001> texture guarantees that the application of E is along [001], rather than the polar vectors of the orthorhombic phase of KNN. It is able to achieve domain engineered configurations in <001> textured ceramics. Meanwhile, the effect of aging on domain configuration is studied for Sb and Li doped KNN textured ceramics. Our investigations found that an aging effect was found to exist in the orthorhombic single phase field, not only in the orthorhombic and tetragonal two-phase field as previously reported. No variation of phase structure was revealed between before and after aging states. However, pronounced changes in domain morphology were observed by both PFM and TEM: more uniform and finer domain structures were then found with aging. These changes were even more pronounced on poling the aged state. A large number of sub-micron lamellar domains within micron-domains were observed: suggesting a domain origin for improved piezoelectric properties.

4.1 $(K_{0.5}Na_{0.5})Nb_{0.97}Sb_{0.03}O_3$

Here, we present a study of domain evolution driven by aging of <001> textured $(K_{0.5}Na_{0.5})Nb_{0.97}Sb_{0.03}O_3$ (KNN-3%Sb) ceramics in the orthorhombic single phase field mainly using PFM. We find that aging results in a more uniform and finer domain structure, which is pronounced for KNN-3%Sb. Large domains with smooth boundaries were observed in this aged sample after poling.

The P-E hysteresis loops of unaged and aged KNN-3%Sb ceramics are shown in Figure 4.1(a). A remnant polarization of P_r=20.5 μC/cm^2 and a coercive field of E_c=2.1 kV/mm were found in the unaged condition. Aging make only slight difference in these values with P_r=21.5μC/cm^2 and E_c=1.9 kV/mm. The bipolar ε-E curves for the unaged and aged conditions are shown in Figure 4.1 (b). Aging results in a significant increase of the induced strain：from

0.1% for unaged to 0.16% for aged. However, the unipolar ε-E curves revealed a less pronounced increase, as can be seen in Figure 4.1 (c): from 0.079% (unaged) to 0.90% (aged). The reduced strain of the unipolar ε-E is consistent with changes in the induced polarization, via electrostriction (Q), as

$$\frac{\varepsilon_{unaged}}{\varepsilon_{aged}} = 0.88 \approx \frac{Q}{Q}\frac{P^2_{unaged}}{P^2_{aged}} = 0.91$$

Thus, the changes in the unipolar strain with aging arise due to these in the polarization. However, the much larger changes in strain of bipolar ε-E curves with aging must result from domain switching contributions, potentially similar to that of the T domains in the $BaTiO_3$ crystals by the symmetry conforming concept.[45] This would imply significant changes in the domain distribution with aging and/or subsequent poling.

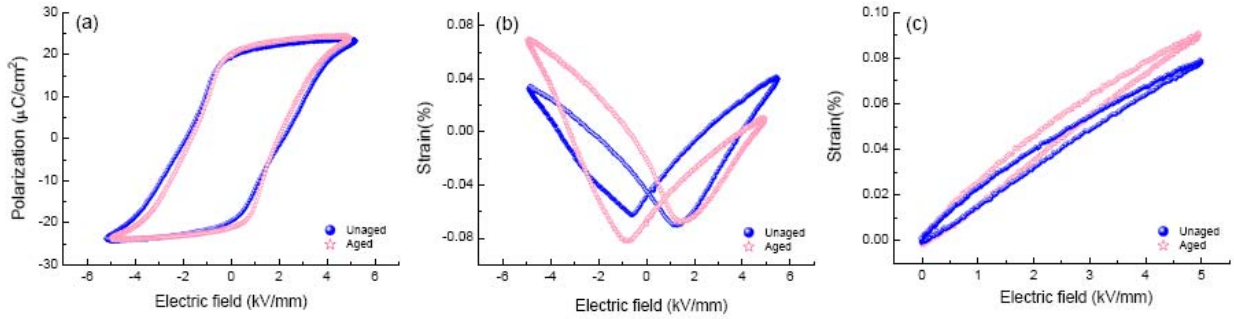

Figure 4.1 Dynamical electromechanical responses for unaged and aged KNN-3%Sb textured ceramics. (a) polarization hysteresis loops, (b) bipolar strain vs electric field curves,(c) unipolar strain vs electric field curves.

Representative PFM images of the domain morphology for <001> textured KNN-3%Sb with different heating treatments are as shown in Figure 4.2. In the unaged condition (see Fig. 4.2a and 4.2b), the domain morphology did not have a preferred crystallographic orientation, but rather irregular shaped boundaries. The size of these domains varied over a wide range between 0.1 and 5 μm. This abnormal domain distribution may result from residual stress remaining within grain structure during sintering. Such domain distributions and morphologies may not be beneficial for enhanced properties. Previous studies of PMN-PT systems near a MPB have

shown that the piezoelectric properties significantly increase with decreasing domain size.[19] The reduced domain size near the boundary is a result of a low anisotropy: which enables low symmetry structurally bridging phases. The reduced domain size was believed to enable a redistribution of the domains under application of electric field E. Representative domain morphology of the aged condition at 170°C after poling are shown in Figures 4.2c and 4.2d. Compared with the unaged state, clear differences can be seen. First, many small domains emerged after aging whose size was on the order of several hundred nanometers. Second, the domain distribution was more uniform, and due to the small size no notable domain boundaries can be seen. These changes are believed to generate from possible defect migration. [41,45] Please note that aging took place at 170 °C, which is in the *T* phase field and above the *O* -> *T* boundary near 130 °C. Thus, following a symmetry conforming principle, mobile defects would redistribution to have a tetragonal-like symmetry at this temperature with time on field. Under bipolar drive, this symmetry conforming state could enable domain switching between {110} orthorhombic variants.

Next, we studied the effect of poling before and after aging, as shown in Figure 4.3. Our finding supports the above arguments that the enhanced induced strain results from domain contribution via defect symmetry conformation. In the unaged condition, poling resulted in 2-5 μm sized irregular domain patters with rough domain boundaries. These results demonstrate an unusual polydomain structure for a poled state (see Figure 4.3a and 4.3b). However, when the aged condition was poled, the domain morphology was notably different features (see Figure 4.3c and 4.3d): macro-domains of 10μm in size were apparent with smooth boundaries, although a single domain state was still not found. It would seem that the more uniform and finer domain structure in the aged condition (see Figure 4.3c and 4.3d) is more ready redistributed under E, resulting in the evolution of larger macro-domain plates. Subsequent application of E along a nonpolar axis at room temperature may result in broadened domain walls, via the frozen in defect symmetry conformed along {001}. Such broadened walls could serve as nuclei for domain switching.[140]

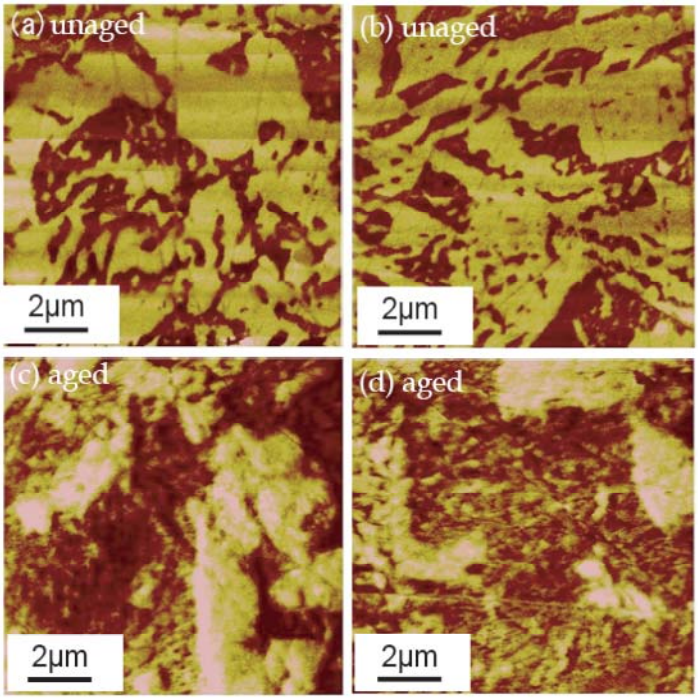

Figure 4.2 Domain morphologies of KNN-3%Sb textured ceramics under two different conditions, (a)-(b) unaged and (c)-(d) aged.

The high density of domain walls caused in the aging process dramatically increases this domain evolution under E. It is noted that domain patterns of <001> textured KNN-3%Sb ceramics observed here does not satisfy any crystallographic orientation, although different domain morphologies of KNN ceramics have been reported. [42-44] We believe that such difference may come from the stoichiometry or sintered process.

Finally, we investigated the domain and local structures in the aged condition by transmission electron microscopy (TEM). Typical domain structures by bright field and lattice imaging are shown in Figure 4.4. The bright field image reveals the presence of fine domains of length 100-300nm and width of 10-30nm. These fine domain structures were oriented along {110} type directions, consistent with an orthorhombic structure. Also, the domain size observed by TEM is consistent with that by PFM in the aged condition. Please note that the domain size observed by TEM images is often smaller than that by PFM, which is believed to originate from a decreasing domain size with sample thickness. A selected area electron diffraction (SAED) pattern is shown in the inset of Fig. 4.4a. This inset does not reveal diffuse scattering along <001> as recently reported. [141] Super-reflections observed in A-site perovskites were believed to originate from

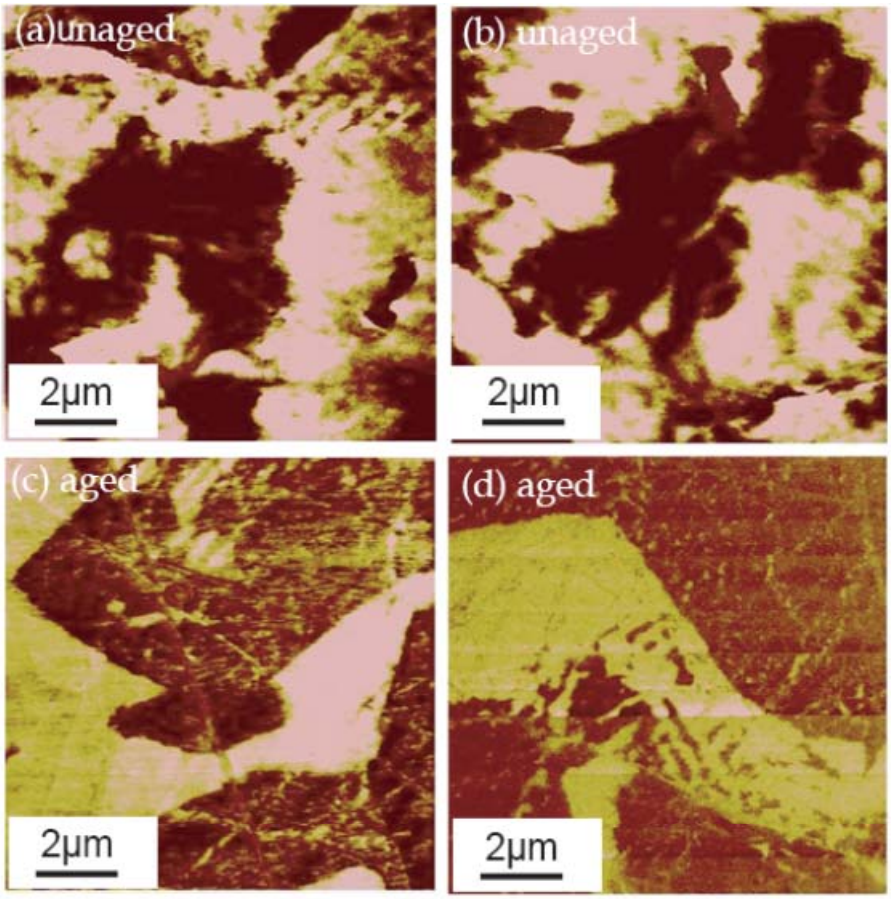

Figure 4.3 Domain topologies of poled KNN-3%Sb textured ceramics with E=3kV/mm, (a)-(b) unaged and (c)-(d) aged.

the possible octahedral tilting or A-site cation ordering. To investigate the possible existence of localized ordering of A-site cations or octahedral tilting on the nanoscale, high resolution lattice images were obtained for the aged condition (Fig.4.4b). No local structural modulation was observed in the lattice image and also the power spectrum of the lattice image (shown as the inset of Fig.4.4b) was consistent with that of the SAED, which demonstrates that A-site cation ordering or octahedral tilting does not exist on the nanoscale for the KNN-3%Sb textured ceramics.

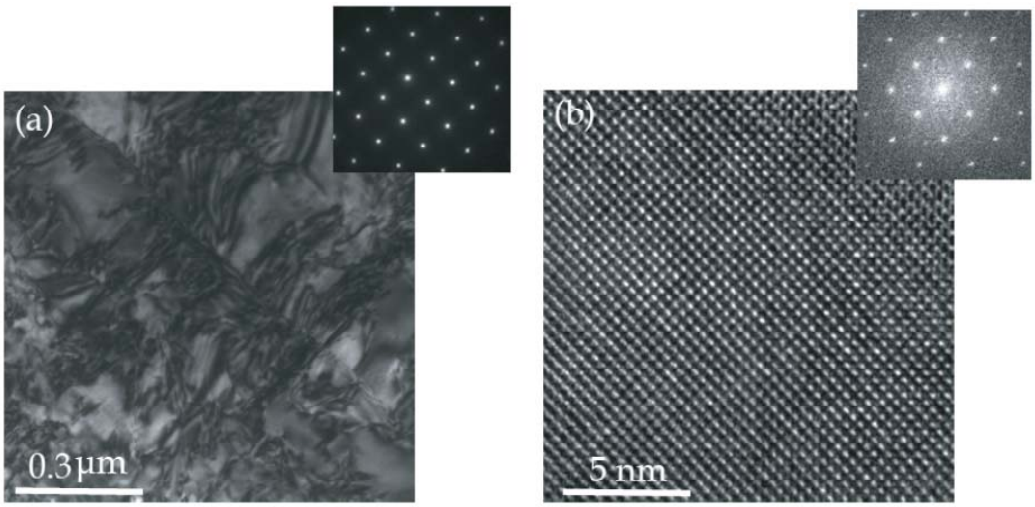

Figure 4.4 TEM results for KNN-3%Sb textured ceramics, (a) bright-field images along [001] zone axis, the inset shows the SAED; (b) a typical <001> high resolution lattice image and the inset is the corresponding power spectrum.

Our findings show that the defect symmetry conforming principle can have important consequence on systems containing a PPB boundary between *O* and *T* phases. This boundary is driven by temperature rather than composition as the MPB. Thus, electric fields applied in the high temperature phase develop a defect conforming symmetry consistent with phase. On cooling through the PPB, the defect-conforming symmetry of the high temperature phase is preserved in the lower one. This provides, in a sense, the low temperature phase with a structural link to the high temperature one. Such a link can have significant consequence for domain switching, where fields applied along crystallographic directions different than that of the polarization vector could result in enhanced induced strains.

4.2 $(K_{0.5}Na_{0.5})Nb_{0.98}Li_{0.02}O_3$

Owning to the sensitivity of KNN's domain morphology on thermal treatment, aging has been exploited as a means to improve its piezoelectric properties.[41] Improved piezoelectric properties in the single orthorhombic phase field of Sb doped KNN has been reported in previous section, whose origin was believed similar to enhanced field induced domain switching in single T phase $BaTiO_3$ crystals after aging[45]. The enhanced properties were ascribed to large domains

(~10μm) with smooth boundaries after poling in the aged state which were readily redistributed under electric field to a finer domain morphology. Whether such enhancement not only exists in Sb doped KNN, but also in Li-doped KNN is not clear.

Here, we present TEM study of KNN-2%Li textured ceramics, which possessed normal micro-size domains. These samples provided a good opportunity to study the evolution of domain structures. Four different conditions were investigated: unaged, poled before aging, aged, and poled after aging. Property measurements were taken that revealed aging effects. The features of domain walls were analyzed, and their possible role on properties discussed. The focus is on domain and property changes with aging.

The P-E hysteresis loops of unaged and aged KNN-2%Li ceramics are shown in Figure 4.5(a). A remnant polarization of P_r=16.2 μC/cm^2 and a coercive field of E_c=1.75 kV/mm were found in the unaged condition. Aging made only a slight difference in these values with P_r=18μC/cm^2 and E_c=1.5 kV/mm. Bipolar ε-E curves for the unaged and aged conditions are shown in Figure 4.5(b). Aging resulted in a significant increase of the induced strain： from 0.13% for the unaged condition to 0.21% for the aged one. These larger changes in the strain of the bipolar ε-E curves with aging may result from changes in the polarization and domain switching mechanism, potentially similar to that of the T domains in the $BaTiO_3$ crystals by the symmetry conforming concept.[24] This would imply significant changes in the domain distribution with aging and/or subsequent poling.

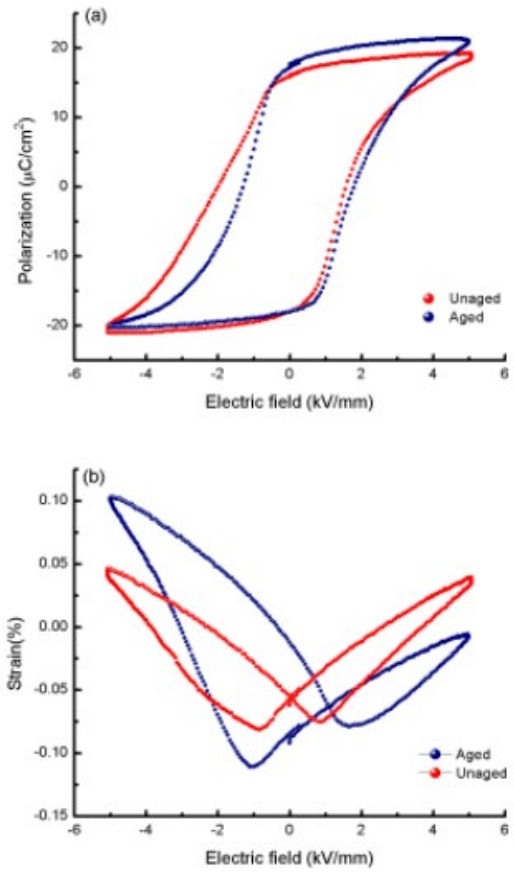

Figure 4.5 Dynamical electromechanical responses for unaged and aged KNN-2%Li textured ceramics. (a) Polarization hysteresis loops, (b) bipolar strain hysteresis curves.

Selected area diffraction patterns (SAED) for as-received KNN-2%Li taken along different zone axes is shown in Figure 4.6. Figure 4.6(a) taken along the [100], show only fundamental reflections, consistent with prior results for KNN-3%Sb textured ceramics.[23] No indications of super-reflections or diffuse scattering were detected, as recently reported.[44,141] The SAED patterns along [110] and [112] (see Figs.4.6b and 4.6c) further confirmed the lack of such super-reflections or diffuse scattering. Thus, it can be concluded that neither octahedral tilting and A-site cation ordering, nor 1-D correlated strings of atomic displacements,[141] exist in the KNN-2%Li ceramics studied here. SAED patterns for the aged state taken along [100], [110] and [112] are shown in Figure 4.7(a)-(c), respectively. No changes in these patterns were found, relative to those the as-received state (see Figs.4.6). Clearly, aging does not result in the change in the local or average crystal structure. Thus the improved properties with aging have no

contribution changes in phase structures. Next, possible domain configuration changes with aging will be considered.

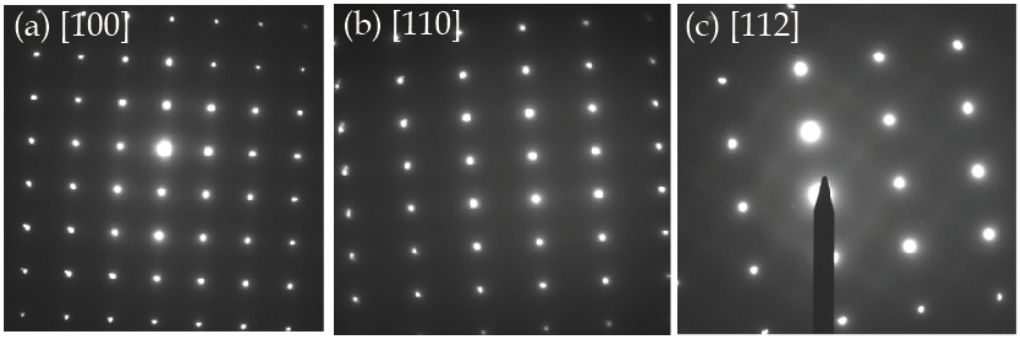

Figure 4.6 Selected area diffraction patterns for unaged sample along the (a) [100], (b)[110], and (c)[112], respectively.

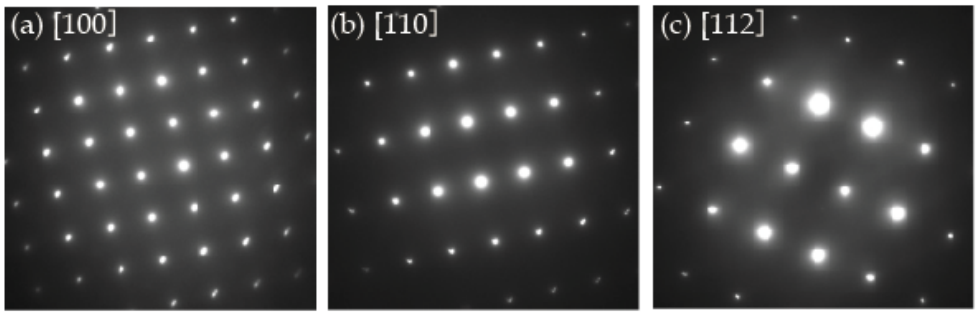

Figure 4.7 Selected area diffraction patterns for aged sample along the (a) [100], (b)[110], and (c)[112], respectively.

The domain morphology for the as-received state was studied by bright field imaging, as shown in Figure 4.8. The bright field images revealed the presence of fine regular domains of several hundred nanometers to microns in length. The width varied between different regions having domains of different shape: from 10nm to several hundred nanometers. In Figure 4.8a, long regular domain structures can be seen which have narrow walls: less than 10nm in width. Stripe-like and step-like domains are notable in Figure 4.8b. Step-like shaped domains result from the interaction of two intersecting domains, in order to minimize energy. Note that defects can easily be seen in both images, which were also commonly found in the as-received state.

Comprehensive observations of various regions revealed a large number of defects, which existed independently or interacting with domain walls. It is accepted that the interaction between domain walls and defects pin the motion of domains wall, and decrease the susceptibility with time during aging.[142-146]

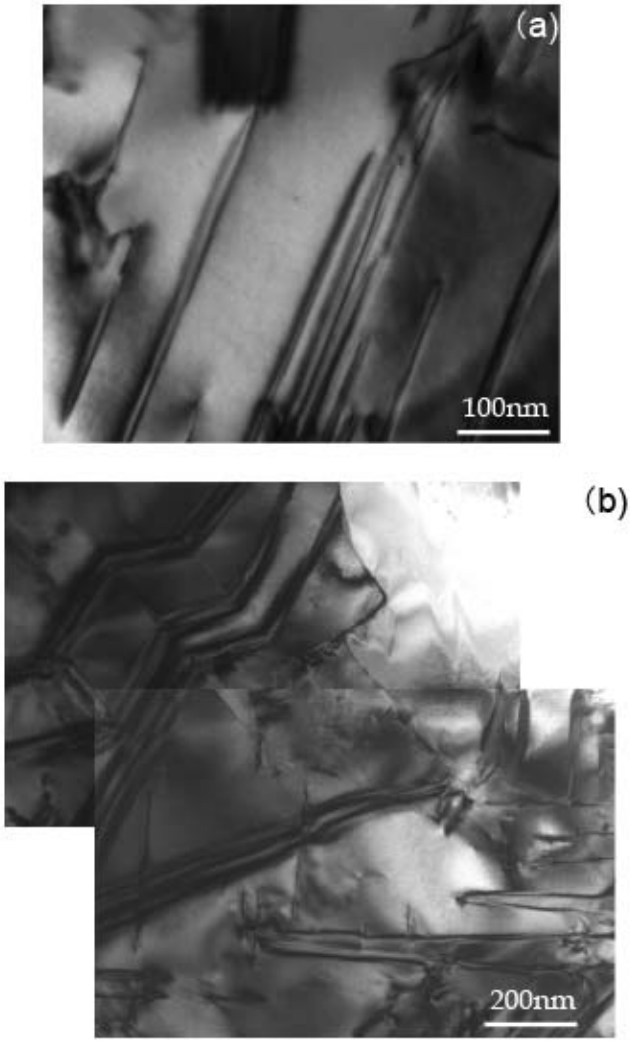

Figure 4.8 Typical domain morphologies of as-received KNN-2%Li textured ceramics in two different regions.

Figure 4.9 shows the domain morphology after poling. Compared with the domain patterns before poling (see Figs.4.8a and 4.8b), notable differences can be seen: zigzag shaped domains accompanied a large number of lamellar domains. These <110> oriented lamellar domains were on the order of 100-200nm in width and micron-meters in length. They were formed during

poling and interacted strongly with existing domains, which changed the morphology of existing domains pronouncedly (as evidenced in the zigzag shape). It can thus be inferred that poling not only drives the motion of domain walls, but also generates a higher density of twin structures. Figure 4.10 show the domain structures after aging, whose inspection will reveal no notable changes with respect to the unaged one before poling (see Figure 4.8). Long regular stripe-like domains were dominant in the regions observed. This shows that aging at 170°C (i.e., T phase field) and subsequent recooling results in the loss of the domain changes that were induced by electric field poling, as evidenced by the loss of the <110> oriented lamellar domains followed by poling. The possibility that regions having these <110> lamellar domains formed by poling cannot be excluded, but we did not find any evidence thereof. Although long stripe-like domains were observed in as-received state, they did not have intersecting twin boundaries, as can be seen in Figure 4.10. This perpendicular orientation of neighboring intersecting domains may be a residual of the elastic boundary conditions of the <110> lamellar domains (poled condition) from which they nucleate on subsequent recooling without E. Thus, the intersecting 90° patterns might be considered to result from consecutive steps of: (i) formation of <110> lamellar domains on poling; (ii) re-nucleation of stripe-like domains on re-cooling within the elastic constraints imposed by the parent domains; and (iii) formation of a stripe-like domain distribution on cooling, which achieves elastic compatibility. Note that the appearance of fine domains during aging has been previously observed in KNN-3%Sb textured ceramics by PFM: thus, the formation of fine domains in aged KNN-2%Li was anticipated, as verified by PFM (images not shown).

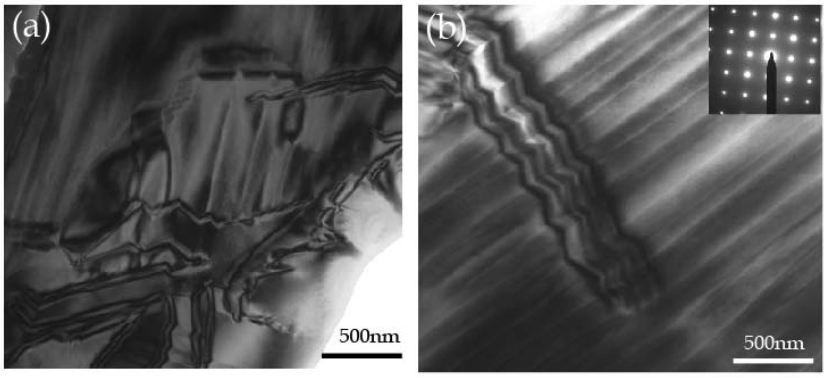

Figure 4.9 Typical domain morphologies of poled on as-received KNN-2%Li textured ceramics in two different regions.

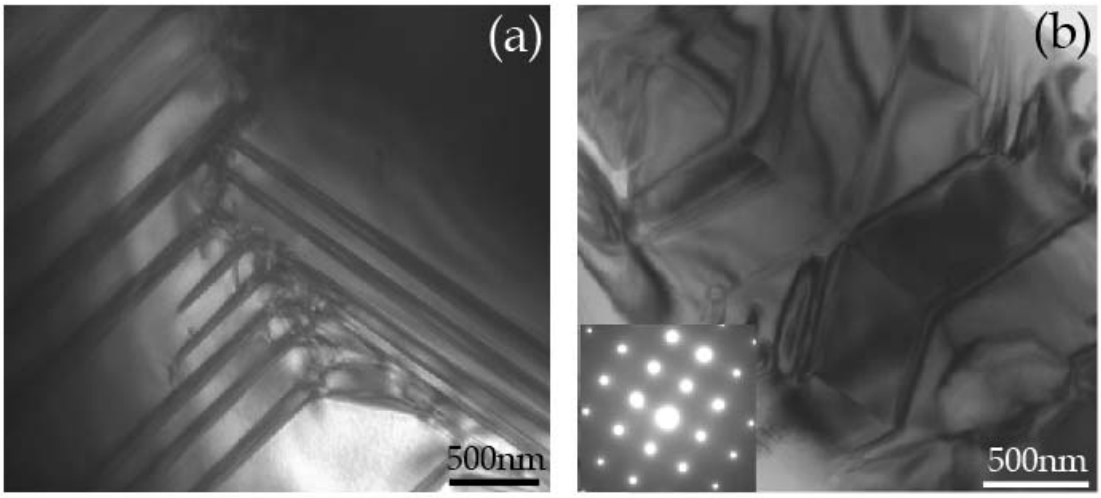

Figure 4.10 Typical domain morphologies of aged KNN-2%Li textured ceramics in two different regions.

Aging makes domain patterns more able to readily respond to applied electric fields, which is confirmed in the following poling experiment as shown in Figures 4.11(a) and (b). In these images, the number of <110> lamellar domains can be seen to be increased, relative to that formed of poling before aging. Please note the change in scale between Figs. 4.9 and 4.11. These lamellar domains are geometrically arranged in a more regular pattern in Figure 4.11, than before the first poling (see Fig.4.9a). In addition, a number of sub-micron lamellar type domains in microdomains were observed, as marked by dashed squares in Fig. 4.11a. These results demonstrate that electric field poling can more effectively and completely rearrange domain structures in the aged condition. Please note that poling was carried out under the same applied E, both before and after aging, and thus external reason for the differences can be excluded. Rather, the enhanced mobility of domain structures during aging account for these notable differences.

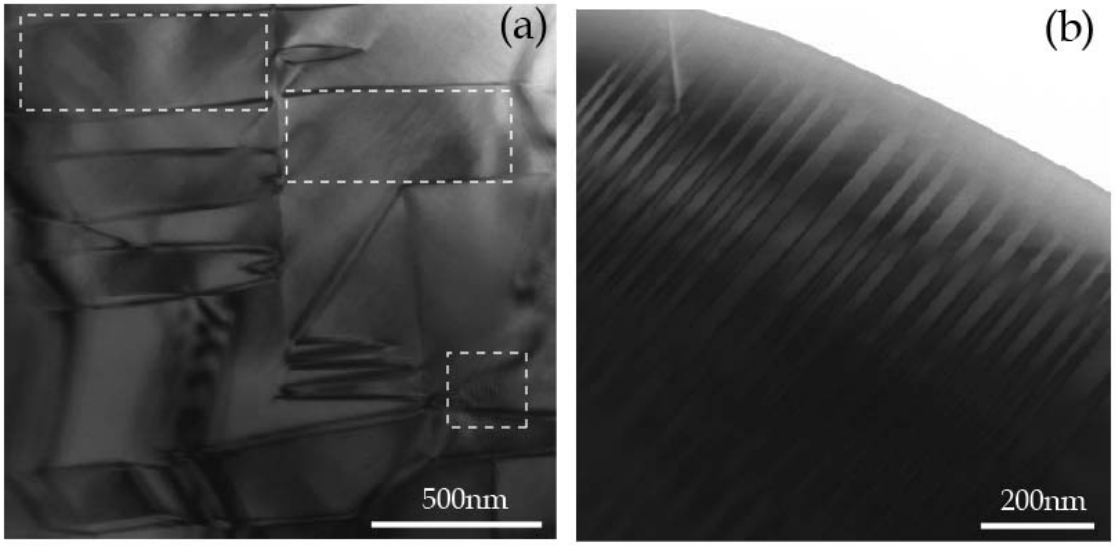

Figure 4.11 Typical domain morphologies of poled on aged KNN-2%Li textured ceramics in two different regions. Large amount of sub-micron lamellar domains within micron-domains can be seen, as marked by dashed squares.

4.3 Summary

Aging associated domain evolution in KNN-3%Sb textured ceramics has been investigated. The results revealed pronounced aging effect is in the orthorhombic single phase field. More uniform and finer domain structures were observed, which are believed to originate from a defect-migration. Large sized domains with smooth boundaries were found in the aged condition after poling.

The domain evolution resulting from aging and poling in <001> textured KNN-2%Li ceramics was studied. No variation of phase structure was found, rather only pronounced changes in domain morphology were observed. Poling resulted in the formation of finer domains of 100-200nm in size that were oriented along <110>. More uniform and finer domain structures were then found with aging. A second poling sequence was found to increase the number of domains. The appearance of sub-micron lamellar domains, in particular within micron-domains, may provide insight into enhanced piezoelectric properties.

Note: this chapter is part of my published work from reference [156]

Chapter 5 Phase identification of Fe-x%Ga alloys

In the present investigation, Fe-x%Ga alloys for x=10, 19, 22.5, 25, and 30 were studied in two different thermal conditions: annealed and quenched. Structural identification, phase distribution and nano-dispersed precipitate morphology were determined by standard TEM and HRTEM methods. It was found that a high density of $D0_3$ nano-precipitates of appropriate size being the critical factor to enhancing the magnetostriction near its first peak; thus, we are able to well-correlate changes in phase structure with prior ones reported for magnetostriction.

5.1 Phase identification for various compositions and thermal treatment

For annealed samples, diffraction patterns along the [001] and [011] zone axes were obtained for the various compositions, as shown in Figure 5.1. For all compositions, (100) super-reflections were observed along both [001] and [011], implying the existence of $D0_3$ or B2 precipitates. Difference between these two structures can be identified by weak (½ -½ ½) super-reflections along the [011] zone, which confirm the presence of $D0_3$. The (½ -½ ½) super-reflections for x=10 and 19 (see Figs.5.1b and d) demonstrated that the $D0_3$ phase is present, coexisting with A2 (as identified by XRD).[147] The intensity of this super-reflection was stronger for x=19 than x=10, revealing significantly increased intensity from $D0_3$ precipitates with increasing x. Please note that this is concurrent with enhanced magnetostriction, as previously reported for x=19.[47] These observations bring prior TEM studies in the same compositional range near x=19 into question, where A2 was identified but $D0_3$ precipitates were not detected.[47] Simulations of structural transformations near this composition range provide insights into our findings: where it was reported that the initial stage of equilibration of the compositionally homogeneous bcc solid solution results in a bcc → B2 congruent ordering, followed by precipitation of Ga-rich B2 particles, which then eventually transforms to particles of the $D0_3$ phase.[148]

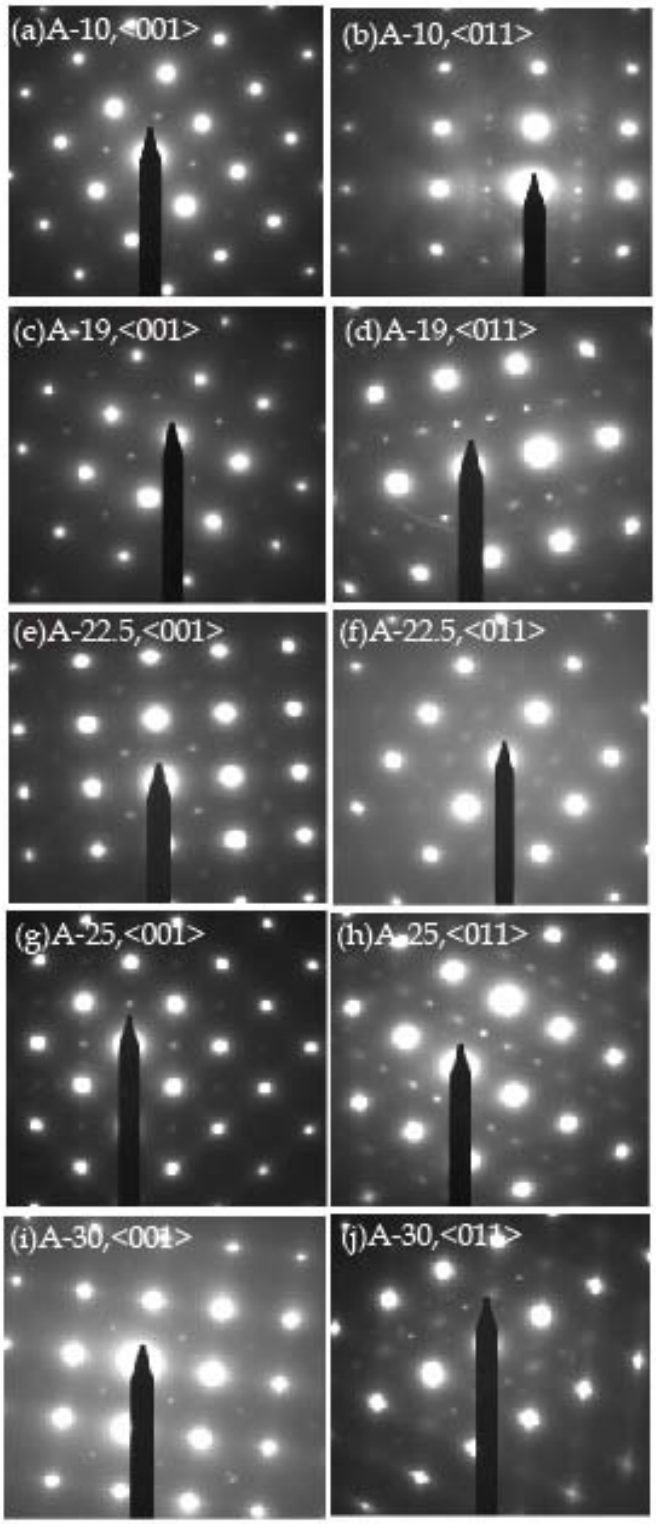

Figure 5.1 SAED patterns taken along along [100] and [110] zones for Fe-x%Ga alloys with x=10, 19, 22,5, 25, and 30 in the annealed condition, where A represents annealing.

When x was increased to 22.5, (100) super-reflections were observed along [001] and [011], however (½ -½ ½) ones were not apparent along [011] (see Fig. 5.1f). This shows that the major contribution to the (100) super-reflections for x=22.5 comes from B2, with little to no volume fraction of $D0_3$. For x=25, the [011] diffraction pattern again exhibited (½ ½ ½) super-reflections, demonstrating A2+$D0_3$+B2 phase coexistence (see Fig.5.1h). Similarly, annealed samples with x= 25 and x=30 showed similar diffraction patterns along the [001] and [011] zones, again indicating A2+$D0_3$+B2 phase coexistence.

For 10<x<19, our results show that the $D0_3$ precipitate volume fraction increased with increasing x. This is consistent with the increase of the magnetostriction in this composition range and a peak value in λ_{100} in the quenched state near x=19.[47] Furthermore, as this peak in λ_{100} was passed, the $D0_3 \rightarrow$ B2 transformation of the nanoprecipitates is consistent with the decreasing value of λ_{100}. With further increasing Ga content to 25<x<30, A2+$D0_3$+B2 phase coexistence was indentified in the compositional range, where the second maximum in magnetostriction was previously reported.

In the quenched state, (100) super-reflections were observed along both [001] and [011] zones for all compositions studied, as can be seen in Figure 5. 2. No (½ ½ ½) superlattice reflections were observed along [011] for x=10 (see Fig.5.2b), which means that the nucleation of $D0_3$ precipitates is strongly suppressed by quenching and that A2 is dominant. For x=19, relatively strong (½ ½ ½) super-reflections were found along [011] (see Fig. 5.2d): again concurrent with prior report of enhanced magnetostriction on quenching. This comparison indicates that a high concentration of nano-size $D0_3$ precipitates accounts for the first peak in λ_{100}. Please note that this finding contradicts prior TEM investigations of quenched x=19, where quenching was believed to extend the A2 phase stability limit to higher x.[47] In addition, a single A2 phase field can not explain the increased λ_{100}. For quenched x=22.5, the (½ ½ ½) superlattice reflection intensity was weaker than for x=19, revealing that the $D0_3$ precipitate concentration was reduced. With further increasing x, in the quenched state, the intensity of the (½ ½ ½) superlattice reflection was again found to increase. This shows that the volume fraction of the $D0_3$ precipitates again increased for 25<x<30, corresponding to the increase of λ_{100} as the second peak in λ_{100} was approached. For quenched x=30, extra reflections become apparent near the fundamental ones, indicative of incoherency of B2 and $D0_3$ phases. Diffraction patterns along

[011] did not reveal the presence of (½ ½ ½) super reflections, indicating that the B2 phase was dominant.

In the quenched state, it can thus be concluded that the intensity of the (½ ½ ½) super-reflection increases when both magnetostriction peaks are approached with increasing x, and correspondingly decreases when these peaks are passed. The intensity was the strongest for quenched x=19, whose peak in magnetostriction was the most pronounced. These results are consistent with a concentration of $D0_3$ precipitates of nano-scale size being the critical factor for the magnetostriction enhancement. Recent theoretical calculation have predicted that the nano-size of the precipitates guarantees a single-domain state, reducing hysteresis and eliminating energy dissipation associated with domain wall motion.[140]

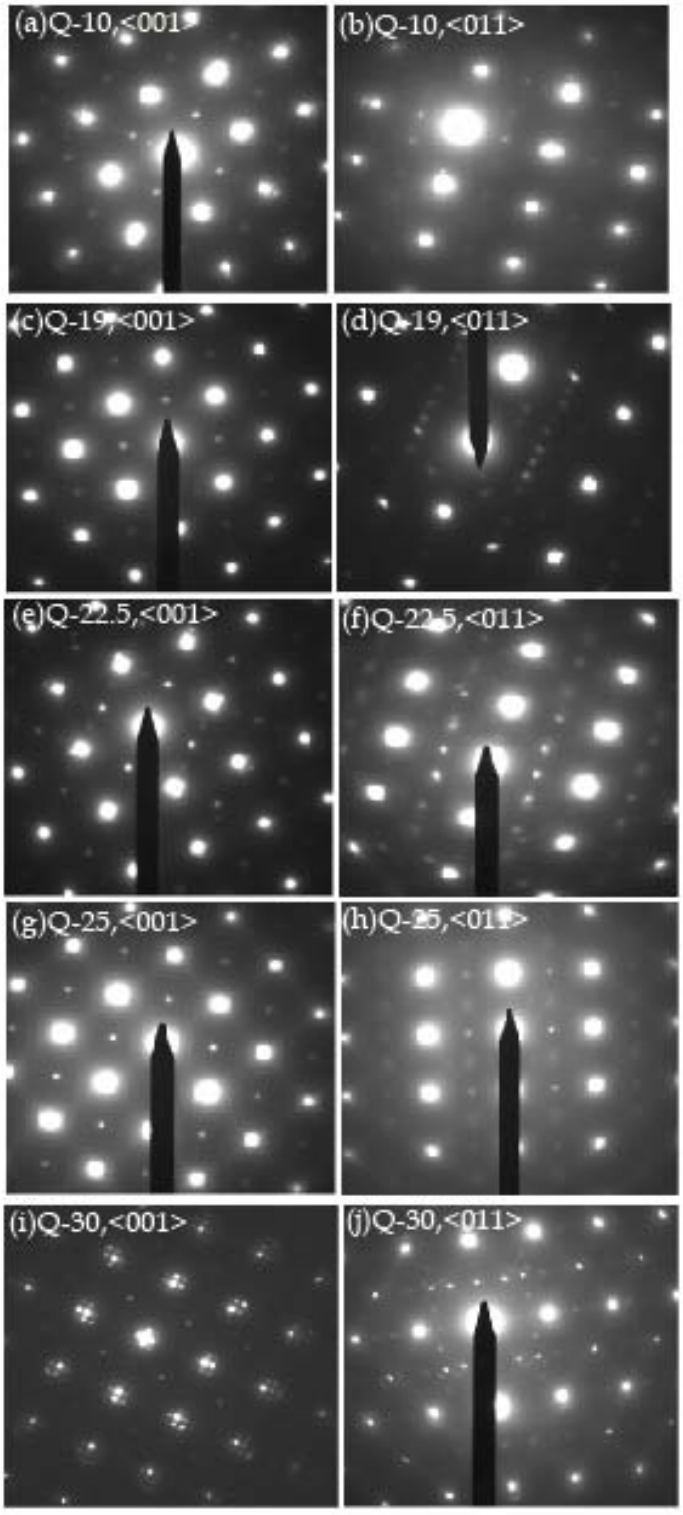

Figure 5.2 SAED patterns taken along along [100] and [110] zones for Fe-x%Ga alloys with x=10, 19, 22,5, 25, and 30 in the quenched state, where Q represents quenching.

5.2 Evolution of nanostructures

Next, dark field images for x=10, 19 and 22.5 were obtained. The studies focused on the (100) super-reflection because (i) for x=19, the intensity contribution comes from only $D0_3$ precipitates and not B2 ones, as identified in the diffraction study (see Fig.5.1); and (ii) the intensity of the (½ ½ ½) super-reflections were weaker than that along (100), and hence it was difficult to obtain clear dark field images using (½ ½ ½).

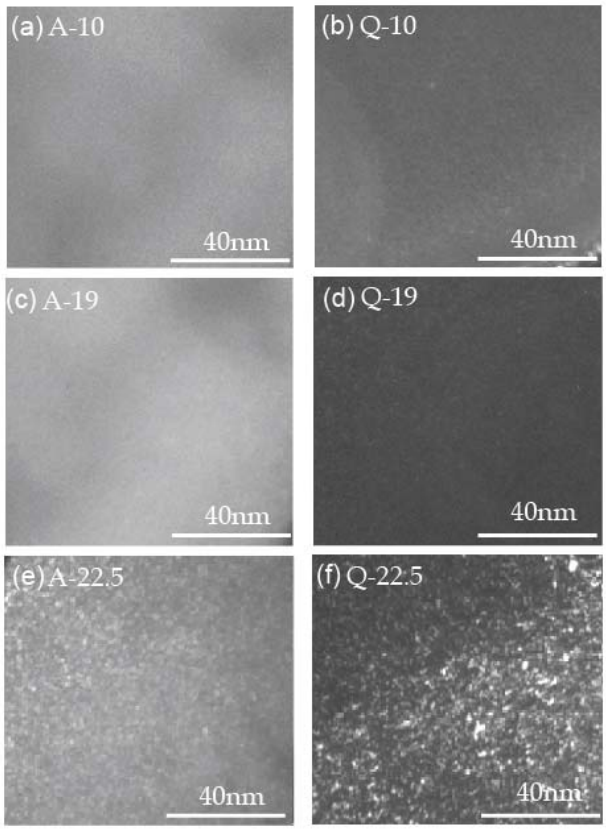

Figure 5.3 Dark field images obtained from (100) superlattice-reflections for Fe-x%Ga alloys with x=10, 19 and 22.5 in annealing and quenching states.

In the images of Figure 5.3, the size of the precipitate can be seen to be small, which limited the characterization of their specific features. Although the precise size cannot be obtained from these dark field images, one can make some general observations: (i) the size of the precipitates in both annealed and quenched conditions for x=10 and 19 was <5nm; (ii) an

increase of size was apparent for x=22.5, where the precipitates were indentified to be B2 instead of $D0_3$ (see previous section).

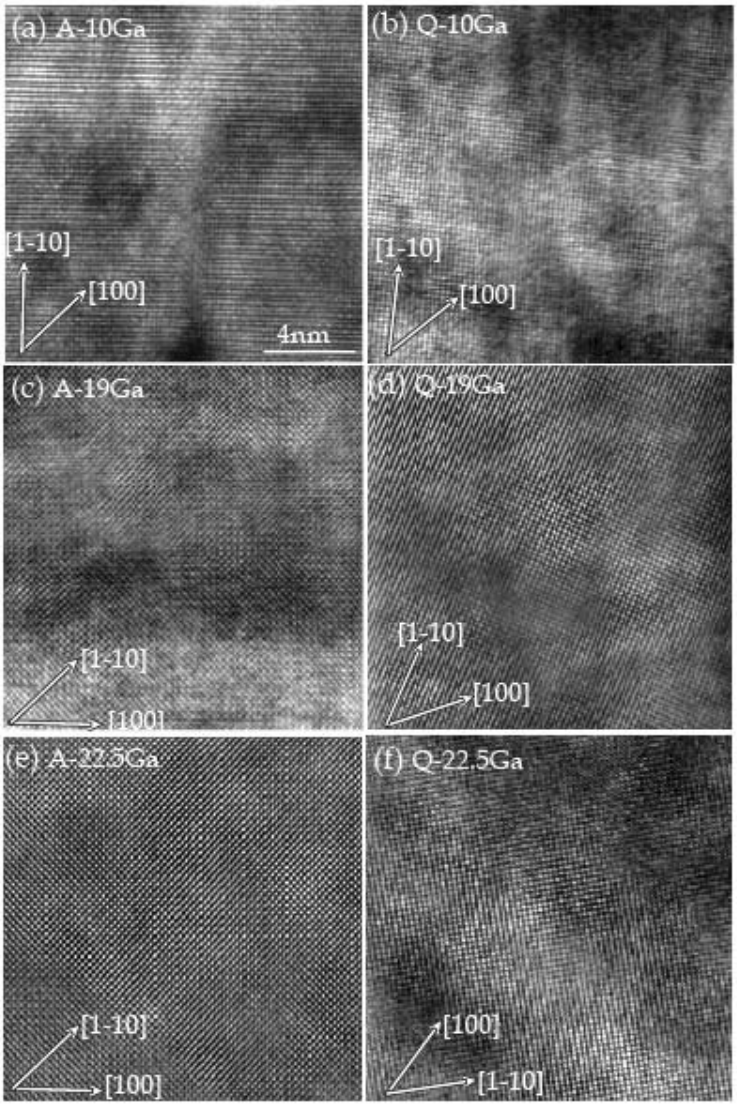

Figure 5.4 HRTEM images for (a) annealed Fe-10 at.%Ga, (b) quenched Fe-10 at.%Ga, (c) annealed Fe-19 at.%Ga, (d) quenched Fe-19 at.%Ga, (e) annealed Fe-22.5 at.%Ga, and (f) quenched Fe-22.5 at.%Ga alloys.

Finally, HRTEM was used to obtain a better understanding of the precipitate features. Again, due to the samples being oriented along <100>, attention was focused on the (100) super-reflections. Samples were studied in both annealed and quenched conditions. Lattice images

obtained along <100> for three compositions (x=10,19 and 22.5) under two different thermal treatments are shown in Figure 5.4. No variations in the lattice fringes were observed for these specimens, indicating a stable mixture of A2 (bcc) and precipitates during decomposition. Corresponding power spectrums of these lattice images are given in Figure 5.5. Strong (110) reflections can be seen in all of these patterns, corresponding to the fundamental lattice fringes common to both the disordered A2 phase and ordered $D0_3$/B2 precipitates. The (100) super-reflections evidence the existence of $D0_3$/B2 precipitates for all specimens studied, consistent with diffraction data in Figs. 5.1 and 5.2. As identified in the diffraction study, contributions to the super-reflection intensity come from only $D0_3$ precipitates for x=19, but from A2+B2 for x>22.5.

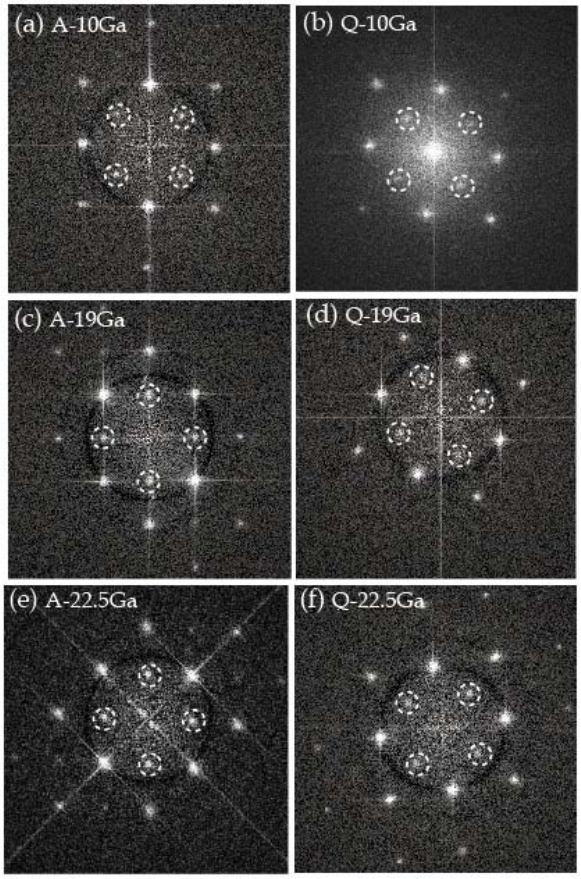

Figure 5.5 Power spectrums of the lattice images (given in Figure 5.4) for (a) annealed Fe-10 at.%Ga, (b) quenched Fe-10 at.%Ga, (c) annealed Fe-19 at. %Ga, (d) quenched Fe-19 at.%Ga, (e) annealed Fe-22.5 at.%Ga, and (f) quenched Fe-22.5 at.%Ga alloys. The spots marked by dotted

circle are (100) super-reflections, which were used to obtain the inverse fast Fourier transformation (in Figure 5.6)

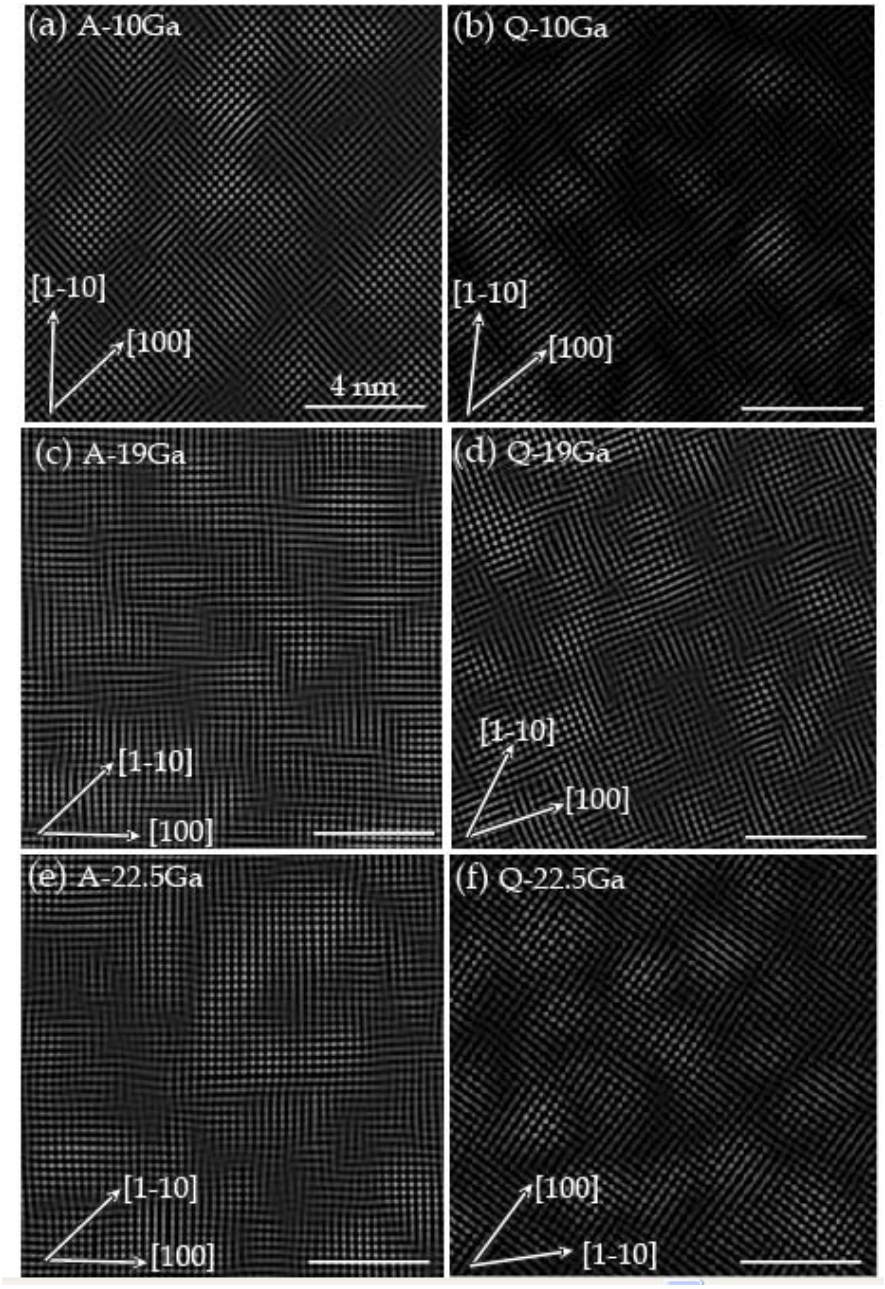

Figure 5.6 Inverse fast Fourier transform of the (100) reflections for (a) annealed Fe-10% at.%Ga, (b) quenched Fe-10 at.%Ga, (c) annealed Fe-19 at.%Ga, (d) quenched Fe-19 at.%Ga, (e) annealed Fe-22.5 at.%Ga, and (f) quenched Fe-22.5 at.%Ga alloys. These images are

interference patterns, which contain only the spatial frequencies around the weak (100) superlattice reflections. The scale bar marked in the figures is 4 nm.

An inverse fast Fourier transform (IFFT) operation was then applied by considering only the (100) super-reflections in the power spectrum images, as shown in Figure 5.6. This operation produces images, that are interference patterns containing only (100) spatial frequencies: thus, these interference patterns contain only (100) g-vector contributions. No attempt was taken to distinguish individual contributions from $D0_3$ and B2 in these interference patterns: but we note that the precipitates were observed by diffraction to be $D0_3$ for x=10 and 19, and $D0_3$+B2 for x=22.5. Nano-size clusters dispersed randomly in a matrix can be seen. Specifically, for x=10, the precipitates were about 2-5nm in length and 2-3nm in width (see Fig.5.6a). An inhomogeneity in size was pronounced, where both the size and its variability were reduced by quenching (see Fig. 5.6b). For x=19, the size of the precipitates was about 2-4nm in length and 1-2nm in width (see Fig. 5.6c): which had a higher volume fraction and were of more uniform size than for x=10. In quenched x=10, (see Fig.5.3b), the size of the precipitates was reduced to 2-4nm in length and 1-2nm in width, and the volume fraction increased. The observation of a larger numer of structurally distorted $D0_3$ precipitates, compared with other compositions, may then account for the first magnetostriction peak observed near x=19.

For x=22.5, in either the quenched or annealed conditions, the size of the precipitates was notably increased compared to x=19. In the quenched condition, the size appeared to be more uniform, but was reduced compared to the annealed one. Such a coarsening of the precipitates with annealing may reflect the formation of the B2 phase, as identified by diffraction above. These data support the proposition that the rapid growth of short-range ordered B2 regions before the onset of long-range ordering could be the reason for the significant suppression of λ_{100} as the first peak in λ_{100} is surpassed for $x > 20$.[149]

It is also noted that a large amount of edge line defects were observed for these precipitates, especially for x=10 and 19, which was consistent with prior studies.[58] According to the work of Bhattacharyya et al., both negative and positive extra half planes that originate inside the $D0_3$ precipitates and the in-plane projection of the Burgers vector of these line defects is a/2[100]. The number of line defects was decreased notably for x=22.5. The decreased number of defects for x=22.5 is consistent with the decreased volume fraction of $D0_3$ precipitates.

5.3 Summary

Alloys of Fe-x%Ga of various compositions and thermal treatments were studied by standard and high resolution TEM. Nano-precipitates were observed in all specimens studied: $D0_3$, B2 and/or unknown phases were found depending on x. Nanoprecipitates of $D0_3$ were found to be dominant for compositions near the magnetostriction peaks in the phase diagram. Quenching was observed to increase the volume fraction of nanoprecipitates for x=19, near the first magnetostriction peak. With increasing x to 22.5, the nanoprecipitates were found to undergo a $D0_3 \rightarrow$B2 transformation. The findings show that a high density of $D0_3$ precipitates of size about 2-3nm is an important factor to enhanced magnetostriction.

Chapter 6

Conclusion and future work

6.1 Conclusions

In this dissertation, I have carried out a systematic investigations of domain and phase structures in highly electrostrictive lead-free NBT-x%BT single crystals and KNN textured ceramics, and highly magnetostrictive Fe-xat.%Ga alloys having various compositions, thermal and field histories, by scanning probe and electron transmission techniques. Many interesting findings have been obtained during the course of this study.

The main findings can be summarized as follows:

6.1.1 NBT-x%BT crystals

- Phase transformation and domain studies of NBT have revealed (i) that a high-temperature tetragonal ferroelastic domain structure is elastically inherited into a lower temperature rhombohedral ferroelectric phase; and (ii) that polar microdomains form within this geometrical constraint on cooling, resulting in a metastable state with attributes of a relaxor ferroelectric.
- Nanoscale domain engineering structure in NBT-x%BT contributes to the high piezoelectric response near the MPB. The addition of $BaTiO_3$ to NBT (i) refines the size of polar nano-regions and enhances their self-organization; and (ii) suppresses formation of proper ferroelastic domains at high temperatures in the paraelectric state, and rather favors the formation of improper ones that form below the ferroelectric Curie temperature that elastically accommodate the ferroelectric ones.
- An increased intensity of the octahedral in-phase tilt ½(ooe) reflections and a decrease in the anti-phase ½(ooo) ones was observed, indicating that the volume fraction of the T phase increases with increasing x as the MPB is approached. This supports that the mechanism of enhanced piezoelectricity for NBT-x%BT near the MPB has both polarization rotation and polarization extension contributions.

❒ Near the MPB, small amount of Mn substituents favor the formation of micro-sized ferroelectric domains in the R phase field, which contains a high density of ½ (ooe) octahedral tilted regions that may have tetragonal distortions of limited spatial lengths.

❒ 10-50nm sized heterogeneous regions were observed within a 200nm sized domain structure, representing isolated polar nanoregions inside of larger domain organizations. It was demonstrated that the distribution of these heterogeneities was not relevant to the domain morphology on the macron-scale indicating that (i) the nanoscale polarization dynamics are not confined by the domain boundaries, and (ii) the disorder originates from polar nanoregions. It is inferred that the high piezoelectricity of NBT-x%BT is due to a polarization dynamics with high sensitivity to electric field and a broadened relaxation time distribution, both of which can be attributed to polar nano-domains.

6.1.2 KNN textured ceramics

Aging effect exists in the O single phase field, not only in the O and T two-phase field as previously reported. No variation of phase structure was detected between before and after aging states. However, pronounced changes in domain morphology were observed. More uniform and finer domain structures were then found with aging, due to defect-migration. These changes were even more pronounced on poling the aged state. The appearance of a large number of sub-micron lamellar domains, in particular within micron-domains, helps explain the improved piezoelectric properties.

6.1.3 Fe-xat.%Ga alloys

Nano-precipitates were observed in all specimens studied: $D0_3$, B2 and/or unknown phases were found depending on x. Nanoprecipitates of $D0_3$ were found to be dominant for compositions near the magnetostriction peaks in the phase diagram. Quenching was observed to increase the volume fraction of nanoprecipitates for x=19, near the first magnetostriction peak. With increasing x to 22.5, the nanoprecipitates were found to undergo a $D0_3 \rightarrow$B2 transformation. The findings show that a high density of $D0_3$ precipitates of nano-size is the critical factor for the first maximum in the magnetostriction.

6.2 Future work

6.2.1 NBT-x%BT crystals

Our TEM studies have revealed compositional dependent octahedral tiltings and preliminarily established the relationship between octahedral tiltings and enhanced piezoelectric properties approaching the MPB. Across the MPB for x>6, it is anticipated that octahedral in-phase tilting would decrease. Then the question arises: how the octahedral anti-phase tilting would evolve? Due to the lack of specimens across the MPB for x>6, we are not able to perform experiments to clarify this issue. Future work needs to be done on these new compositions to observe the evolution of both octahedral in-phase and anti-phase tiltings away from the MPB. In addition, the interaction of octahedral in-phase and anti-phase tiltings under electric field is not clear. Therefore, it would be interesting to continue investigations of field dependent octahedral tilting to obtain a clear correlation between large field induced strain and octahedral tilting. In-situ electric field high-energy transmission XRD experiments along various directions would be suggested as follows:

1. Prepare (100)/(010)/(001) oriented cube samples and apply electric field along [100] direction. Obtain diffraction patterns along [100], [010] and [001] directions with zero and increasing field. Compare the change of in-phase tilting intensity before and after field applied along [100].
2. Prepare (100)/(011)/(01-1) oriented cube samples and apply electric field along [100] direction. Obtain diffraction patterns along [011] and [01-1] directions with zero and increasing field applied along [100].
3. Prepare (100)/(011)/(01-1) oriented cube samples and apply electric field along [011] direction. Obtain diffraction patterns along [011], [100] and [01-1] directions with zero and increasing field applied along [100].

In addition, the valence of Mn still needs to be experimentally clarified and this directly correlates with sites they occupy. Electron energy loss spectrum (EELS) might be one way to study it. The most challenge task is to locate Mn during study due to the small amount of Mn

(1%). If the valence of Mn is obtained, then the site they occupy in the octahedron can be accurately determined.

6.2.2 Fe-x%Ga alloys

Our TEM studies have clarified the phase structures dependent on compositions, in particular for x<19, which provides a good structural explanation for enhanced magnetostriction near the first peak in the diagram. Our HRTEM investigations revealed atomic scale $D0_3$ clusters dependent on composition and thermal treatment. However, a fundamental understanding of ordering in Fe-xat.%Ga alloys through structural evaluations of local atomic environments is needed. A more detailed electron energy loss spectrum (EELS) and diffuse scattering investigation on the electronic state and ordering of Fe and Ga atoms as a function of solute content, annealing temperature, and subsequent cooling rate are needed to gain an in-depth understanding of how ordering influences magnetostriction in these alloys.

References

1. N. A. Spaldin and M. Fiebig, Science, 309, 391 (2005).
2. B. Jaffe, W. R. Cook, and H. Jaffe, Piezoelectric Ceramics. Academic Press, London, 1971.
3. N. J. Donnelly, T. R. Shrout, and C. A. Randall, J. Am. Ceram.Soc., 90, 490 (2007).
4. J. Rodel, W. Jo, K.T. Seifert, E. Anton, T. Granzow, D. Damjanovic, J. Am. Ceram. Soc., 92, 1153 (2009).
5. G. Shirane, R. Newnham, and R. Pepinsky, Phys. Rev. 96, 581 (1954).
6. B. Noheda, D. E. Cox, G. Shirane, J. A. Gonzalo, L. E. Cross, S.-E. Park, Appl. Phys. Lett. 74, 2059 (1999).
7. D. Viehland, J. Appl. Phys. 88, 4794 (2000).
8. Y. Saito, H. Takao, T. Tani, T. Nonoyama, K. Takatori, T. Homma, T. Nagaya, and M. Nakamura, Nature (London) 432, 84 (2004).
9. Y. Guo, K. Kakimoto, and H. Ohsato, Appl. Phys. Lett. 85, 4121 (2004).
10. Y. M. Chiang, G. W. Farrey and A. N. Soukhojak, Appl. Phys. Lett. 73, 3683 (1998).
11. Q. Zhang, Y. Zhang, F. Wang, Y. Wang, D. Lin, X. Zhao, H. Luo, W. Ge, and D. Viehland, Appl. Phys. Lett. 95, 102904 (2009).
12. W. W. Ge, H. Liu, X. Y. Zhao, B. J. Fang, X. B. Li, F. F. Wang, D. Zhou, P. Yu, X. M. Pan, D. Lin, and H. S. Luo, J. Phys. D: Appl. Phys. 41, 115403 (2008).
13. T. Tani, T. Takeuchi, and T. Kimura, Patent Abstracts of Japan, Patent No. 2001261435 (A),Toyota Central Res & Dev, Japan, 2001.
14. Y.F. Chang, S.F. Poterala,Z.P. Yang, S.Trolier-Mckinstry and G.L. Messing, Applied Physics Letters,95,232905 (2009).
15. F.M. Bai, Ph.D dissertation, Virginia Tech, 2006.
16. http://en.wikipedia.org/wiki/File:Perovskite.svg
17. M. F. Chisholm,W.D. Luo, M. P. Oxley, S.T. Pantelides, H. N. Lee, Phy. Rev. Lett. 105, 197602 (2010).
18. H. Fu and R.Cohen, NATURE, 403, 281 (2000).
19. F.M. Bai, J.F. Li, D. Viehland, Appl. Phys. Lett. 85, 2313 (2004).
20. S.-E. Park, T.R. Shrout, J. Appl. Phys. 82, 1804 (1997).

21. H. Cao, F.M. Bai, N.G. Wang, J.F. Li, D. Viehland, G.Y. Xu and G. Shirane, Phy. Rev. B 72.064104 (2005).

22. B. Noheda, D. E. Cox, Shirane, J. Gao and Z. Ye, Phys. Rev. B 66, 054104 (2002).

23. H. Cao, C. Stock, G.Y. Xu, P.M. Gehring, J. F. Li, D. Viehland, Phys. Rev. B 78 104103(2008).

24. T. Takenaka, K. Maruyama and K. Sakata, Jpn. J. Appl. Phys. 30, 2236 (1991).

25. A. Soukhojak, H. Wang, G. Farrey and Y.-M. Chang, J.Phys.Chemis.Solid. 61,301 (2000).

26. V. Dorcet, G. Trolliard, P. Boullay, Chem. Mater. 20, 5061 (2008).

27. V. Dorcet, G. Trolliard, P. Boullay, Chem. Mater. 20, 5069 (2008).

28. F. Cordero, F. Craciun, F. Trequattrini, E. Mercadelli, C. Galassi, Phys. Rev. B 81, 144124 (2010).

29. J. Zvirdzds, P. Kapostins, J. Zvirgzde, and T. Kruzina, Ferroelectrics 40, 75 (1982).

30. S. Vakhrushev, V. Isupov, B. Kvyathkovsky, N. Okeuneva, I. Pronin, G. Smolensky, P. Syrnikov, Ferroelectrics 63, 153 (1985).

31. J. Suchanicz and J. Kwapulinski, Ferroelectrics 165, 249 (1995).

32. J. Kusz, J. Suchanicz, H. Bohm, J. Warczewski, and J. Phase Trans. 70, 223 (1999).

33. G. Jones and P. Thomas, Acta Crystallogr. B58, 168 (2002).

34. K. Hong and S. Park, J. Appl. Phys. 79, 388 (1996).

35. V. Dorcet, G. Trolliard, Acta Mater. 56, 1753 (2008).

36. E. Hollenstein, M. Davis, D. Damjanovic, N. Setter, Appl. Phys. Lett. 87, 182905 (2005).

37. R. Wang, R. Xie, K. Hanada, K. Matsusaki, H. Bando, M. Itoh, Phys. Status Sol, A 202, R57 (2005).

38. S.T. Zhang, R. Xia and T R. Shrout, J Electroceram 19,251 (2007).

39. W.W. Ge, J.F. Li, D. Viehland, Y.F. Chang and G. L. Messing, Phys. Rev. B 83, 224110 (2011).

40. J. Tellier, B. Malic, B. Dkhil, D. Jenko, J. Cilensek, and M. Kosec, Solid State Sci. 11, 320 (2009).

41. K. Wang and J.F. Li, Advanced Functional Mater. 20, 1924 (2010).

42. R. P. Herber, G. A. Schneider, S. Wagner, and M. J. Hoffmann, Appl. Phys. Lett. 90, 252905 (2007).

43. J. Fu, R. Z. Zuo and Z. K. Xu, Appl. Phys. Lett. 99, 062901 (2011).

44. S.J. Zhang, H. J. Lee, C. Ma, and X.L. Tan, J. Am. Ceram. Soc., 94, 3659 (2011).

45. X. B. Ren, Nat. Mater. 3, 91 (2004).

46. Handbook of Giant Magnetostrictive Materials, edited by G. Engdhal ,Academic, San Diego (2000).

47. Q. Xing, Y. Du, R.J. McQueeney, T.A. Lograsso, Acta Mater.56, 456 (2008).

48. Ikeda O, Kainuma R, Ohnuma I, Fukamichi K, Ishida K. J Alloys. Compd. 347,198 (2002).

49. Okamoto H, Subramanian PR, Kacprzak L, editors. Binary alloy phase diagrams. Materials Park (OH)ASM International,1702 (1990).

50. Y. Du, M. Huang, S. Chang, D. L. Schlagel, T. A. Lograsso, and R. J. McQueeney, Phys. Rev. B 81, 054432 (2010).

51. Khachaturyan AG, Viehland D. Metall Mater Trans A 38A,2308 (2007).

52. Khachaturyan AG, Viehland D. Metall Mater Trans A 38A,2317(2007).

53. R. Wu, Z. Yang, J. Hong, J Phys: Condens Matter 15, S587(2003).

54. J. R. Cullen, A. E. Clark, M. Wun-Fogle, J. B. Restorff, and T. A.Lograsso, J. Magn. Magn. Mater. 226, 948 (2001).

55. E. Ruedl, P. Delavign, and S. Amelinck, Phys. Status Solidi **28**,305 (1968).

56. Summers EM, Lograsso TA, Wun-Fogle M. J. Mater. Sci. 42,9582 (2007).

57. H. Cao, P. M. Gehring, C. P. Devreugd, J. A. Rodriguez-Rivera, J. Li, and D. Viehland, Phys. Rev. Lett. 102, 127201 (2009).

58. S. Bhattacharyya, J. R. Jinschek, A. Khachaturyan, H.Cao, J. Li, and D. Viehland, Phys. Rev. B 77, 104107 (2008).

59. R.A. Dunlap, J.D. McGraw, S.P. Farrell, J. Magn. Mag. Mat., 305, 315 (2006).

60. M. Laver, C. Mudivarthi, J. R. Cullen, A. B. Flatau, W.-C. Chen,S. M. Watson, and M. Wuttig, Phys. Rev. Lett. 105, 027202 (2010).

61. E. Aksel, J. S. Forrester, J. L. Jones, P. A. Thomas, K. Page, and M. R. Suchomel, Appl. Phys. Lett. 98,152901 (2011).

62. S. Gorfman, P.A.Thomas, J. Appl. Crystallogr. 43,1409 (2010).

63. M. Hinterstein, M. Knapp, M. Holzel, W. Jo, A. Cervellino, H. Ehrenberg, H. Fuess, J. Appl. Crystallogr. 43, 1314 (2010).

64. J. Kling, X.L.Tan, W. Jo, H.-J. Kleebe, H. Fuess, J. Rödel, J. Am. Ceram. Soc. 93,2452 (2010).

65. H. Simon, J. Daniels, W. Jo, R. Dittmer, A. Studer, M. Avdeev, J. Rödel, M. Hoffman, Appl. Phys. Lett. 98, 082901 (2011).

66. W.F. Rao, M. Wuttig, A.G. Khachaturyan, , Phys. Rev. Lett. 106, 105703 (2011)

67. E.A. Eliseev, Sergei V. Kalinin, S. Jesse, S.L. Bravina, and A.N. Morozovska, J. Appl. Phys. 102, 014109 (2007).

68. S. Jesse, A.P. Baddorf, S. V. Kalinin, Nanotechnology 17, 1615 (2006).

69. S. Jesse, A. P. Baddorf, and S. V. Kalinin, Appl. Phys. Lett. 88, 062908 (2006).

70. S. Jesse, B. J. Rodriguez , S. Choudhury, A. P. Baddorf, I.Vrejoiu, D. Hesse, M. Alexe, E. A. Eliseev, A.N. Morozovska, J.X. Zhang, L-Q. Chen and S. V. Kalinin, Nature Materials 7, 209 (2008).

71. I. Pronin, P. Syrnikov, V. Isupov, and G. Smolenskii, Sov. Technol. Phys. Lett. 8, 563 (1982).

72. Z. Xu, M.C. Kim, Jie-Fang Li, and Dwight Viehland, Phil. Mag. A 74, 395 (1996).

73. F. Bai, J. F Li, and D. Viehland, J. Appl. Phys. 97, 54103 (2005).

74. V. I. Syutkina and E. S. Jakovleva, Phys. Status Solidi 21,465 (1967).

75. Y. Jin, Y. Wang, A. Khachaturyan, J. F. Li, and D. Viehland, Phys. Rev. Lett. 91, 197601 (2003).

76. D. Viehland, M. Wuttig, and L.E. Cross, J. Appl. Phys. 68, 6, 2916 (1990).

77. A. Njiwa, E. Aulbach, T. Granzow, and J. Rödel, Acta Mater. 55, 675 (2007).

78. A.N.Soukhojak, H.Wang, G.W.Farrey, and Y.-M.Chiang, J.Phys.Chems.Solids. 61, 301 (2000).

79. E. Salje, Ferroelectrics, 104, 111 (1990).

80. W.Cao and G.R. Barsch, Phys. Rev. B 41, 4334 (1990).

81. I.-K. Jeong, T. W. Darling, J. K. Lee, T. Proffen, R. H. Heffner, J. S. Park, K. S. Hong, W. Dmowski, and T. Egami, Phys. Rev. Lett. 94, 147602 (2005).

82. S. V. Kalinin, B. J. Rodriguez, J. D. Budai, S. Jesse, A. N. Morozovska, A. A. Bokov and Z.-G. Ye, Phys. Rev. B 81, 064107 (2010).

83. D. Viehland, M.-C. Kim, Z. Xu, and J.-F. Li, Appl. Phys. Lett. 67, 2471 (1995).

84. Y. Wang, X.B. Ren, and K.Otsuka, Phys. Rev. Lett. 97, 225703 (2006).

85. V.A. Isupov, Ferroelectrics 315, 123 (2005).

86. G.Y. Xu, Z. Zhong, Y. Bing, Z.G. Ye, C. Stock, G. Shirane, Phys. Rev. B 70, 064107 (2004).

87. G. Y. Xu, P.M. Gehring, C. Stock, K. Conlon, Phase Transitions 79, 135 (2006).

88. S. Hong, J. Woo, H. Shin, J. Jeon, Y. E. Pak, E. L. Colla, N. Setter, E. Kim, and K. No. J. Appl. Phys. 89,1377 (2001).

89. S.V. Kalinin and D. A. Bonnell. Phys. Rev. B 65, 125408 (2002).

90. F. Johann, Á. Hoffmann, and E. Soergel, Phys. Rev. B 81, 094109 (2010).

91. S. Said, J.P. Mercurio, J. Eur. Ceram. Soc. 21, 1333 (2001).

92. C.-S.Tu, I.G. Siny, and V.H Schmidt, Phy. Rev. B 49, 11550 (1994).

93. Y. Hiruma, Y. Watanabe, H. Nagata, and T. Takenaka, Key Eng.Mater. 350, 93 (2007).

94. W. Ge, H. Liu, X. Zhao, X. Pan, T. He, D. Lin, H. Xu, and H. Luo, J. Alloys Compd. 456, 503 (2008).

95. W. W. Ge, H. Liu, X. Y. Zhao, X. B. Li, X. M. Pan, D. Lin, X.H. Xu, B. J. Fang, and H. S. Luo, Appl. Phys. A 95, 761 (2009).

96. W.W. Ge, H. Cao, J.F. Li, D. Viehland, Q.H. Zhang, and H.S. Luo, Appl. Phys. Lett. 95, 162903 (2009).

97. W. W. Cao and C. A. Randall, J. Phys. Chem. Solids 57, 1499 (1996).

98. E.V. Balashova and A.K. Tagantsev, Phys. Rev. B 48, 9979 (1993).

99. E.V. Balashova,V.V. Lemanov, A.K. Tagantsev, A.B. Sherman, and Sh.H. Shomuradov, Phys. Rev. B 51, 8747 (1995).

100. L.A. Schmitt, M. Hinterstein, H.-J. Kleebe, J. Appl. Crystallogr. 43,805 (2010).

101. L.A. Schmitt, J. Kling, M. Hinterstein, M. Hoelzel, W. Jo, H.-J. Kleebe, H. Fuess, J.Mater.Sci. 46, 4368 (2011).

102. S.T. Zhang, A.B. Kounga, E. Aulbach, H. Ehrenberg, J. Rodel, Appl. Phys. Lett. 91, 112906 (2007).

103. S.T. Zhang, A.B. Kounga, E. Aulbach, W. Jo, T. Granzow, H. Ehrenberg, J. Rodel, J. Appl. Phys. 103, 034108 (2008).

104. W. Jo, T. Granzow, E. Aulbach, J. Rodel, D. Damjanovic, J. Appl. Phys. 105, 094102 (2009).

105. B. Wylie-Van Eerd, D. Damjanovic, N. Klein, N. Setter, J. Trodahl, Phys Rev B 82, 104112 (2010).

106. D. Damjanovic, IEEE Trans. Ultrason. Ferroelectr. Freq. Control 56, 1574 (2009).

107. D. Damjanovic, Appl. Phys. Lett. *97,* 062906 (2010).

108. Z. Xu, X.H. Dai, D. Viehland, Phys. Rev. B 51, 6261 (1995).

109. E. Garcia-Gonzalez, A. Torres-Pardo, R .Jimenez, J. M. Gonzalez-Calbet, Chem. Mater. 19, 3575 (2007).

110. C. J. Cheng, D. Kan, S. H. Lim, W. R. McKenzie, P. R. Munroe, L. G. Salamanca-Riba, R. L. Withers, I. Takeuchi, V. Nagarajan, Phys. Rev. B 80, 014109 (2009).

111. J. Schiemer, R. Withers, L. Noren, Y. Liu, L. Bourgeois, G. Stewart, Chem. Mater. 21, 4223 (2009).

112. W.W. Ge, J.F. Li, D. Viehland, H. Luo, J. Am. Cera. Soc. 93, 1372 (2010).

113. E. Aksel, H. Foronda, K. Calhoun, J. L. Jones, S. Schaab, T. Granzow, Func. Mater. Lett. 3, 45 (2010).

114. C.-S. Tu, S.-H. Huang, C.-S. Ku, H.-Y. Lee, R. R. Chien, H. Schmidt, H. Luo, Appl. Phys. Lett. 96, 062903 (2010).

115. N. Balke, I. Bdikin, S. V. Kalinin, A. L. Kholkin, J. Am. Ceram. Soc. 92, 1629(2009).

116. D. A. Kiselev, I. K. Bdikin, E. K. Selezneva, K. Bormanis, A. Sternberg, A. L. Kholkin, J. Appl. D: Appl. Phys. 40, 7109 (2007).

117. A. Yourdkhani, A. K. Perez, C. Lin, G. Caruntu, Chem. Mater. 22, 6075 (2010).

118. R. C. Munoz, G. Vidal, M. Mulsow, J. G. Lisoni, C. Arenas, A. Concha, Phys. Rev. B 62, 4686 (2000).

119. Y.S. Sung and M. H. Kim, Ferroelectrics, Indrani Coondoo (Ed.), ISBN: 978-953-307-439-9, InTech (2010).

120. Nagata and T.Takenaka, J.Euro.Ceram. Soc. 21, 1299 (2001).

121. Y.K. Gao, K. Uchino, D. Viehland, Jpn. J. Appl. Phys. 45, 9119 (2006).

122. S.J. Zhang, S.M. Lee, D.H. Kim, H.Y. Lee, T.R. Shrout, Appl. Phys. Lett. 93,122908 (2008).

123. D. Viehland, X.H. Dai, J.F. Li, Z. K. Xu, J. Appl. Phys. 84,458 (1998).

124. D. Kan, L. Palova, V. Anbusathaiah, C. J. Cheng, S. Fujino, V. Nagarajan, K. M. Rabe, I. Takeuchi, Adv. Funct. Mater. 20, 2436 (2010).

125. P. M. Woodward, Acta Cryst. B 53, 44 (1997).

126. D. I. Woodward, I. M. Reaney, Acta Cryst. B 61, 387(2005).

127. I.M. Reaney, E.L. Colla, N. Setter, Jan.J.Appl.Phys. 33,3984 (1994).

128. D. Viheland, M. C. Kim, Z. K. Xu and J. F. Li, Appl. Phys. Lett. 67, 2471 (1995).

129. C. Ma, X. Tan, E. Dul'kin, M. J. Roth, J. Appl. Phys. 108, 104105 (2010).

130. C. W. Tai, S. H. Choy, and H. L. W. Chan, J. Am. Ceram. Soc. 91, 3335 (2008).

131. C.W. Tai and Y. Lereah, Appl. Phys. Lett. 95, 062901(2009).

132. S. V. Kalinin, A.N. Morozovska, L.Q. Chen and B.J. Rodriguez, Rep. Prog. Phys. 73, 056502 (2010).

133. D. Viehland, S.J. Jang, L. Eric Cross, M. Wuttig, J. Appl. Phys.68, 2916 (1990).

134. Y.S. Kim, A. Kumar, O. Ovchinnikov, S. Jesse, H. Han, D. Pantel, I. Vrejoiu, W. Lee, D. Hesse, M. Alexe, and S. V. Kalinin, ACS Nano, 6, 491 (2012).

135. S.V. Kalinin, B. J. Rodriguez, A. Y. Borisevich, A. P. Baddorf, N. Balke, H. J. Chang, L.-Q. Chen, S. Choudhury, S.Jesse, P.Maksymovych, M. P. Nikiforov, and S. J. Pennycook, Advanced Materials, 22, 314 (2010).

136. C. L. Jia, K. Urban, Science, 303, 2001 (2004).

137. C. L. Jia, V. Nagarajan, J.-Q. He, L. Houben, T. Zhao, R. Ramesh, K. Urban, R. Waser, Nat. Mater. 6, 64 (2007).

138. B. J. Rodriguez, S. Jesse, A. N. Morozovska, S. V. Svechnikov, D. A. Kiselev, A. L. Kholkin, A. A. Bokov, Z.-G. Ye, and S. V. Kalinin, J. Appl. Phys. 108, 042006 (2010).

139. S. E. Park, S. Wada, L. E. Cross, and T. R. Shrout, J. Appl. Phys. 86, 2746 (1999).

140. W.F. Rao, K.W. Xiao, T.L. Chen, Y. Wang, Appl. Phys. Lett. 97, 162901 (2010).

141. Z.G. Yi, Y. Liu, M. A. Carpenter, J. Schiemer and R. L. Withers, Dalton Trans., 40, 5066 (2011).

142. U. Robels and G. Arlt, J. Appl. Phys. **73**, 3454 (1993).

143. G. Stone, H. Steigerwald, K. Buse, W. Sohler, V. Gopalan, S. Phillpot, V. Dierolf, Lasers and Electro-Optics Europe (CLEO EUROPE/EQEC), 2011 Conference on and 12th European Quantum Electronics Conference , 22-26 May 2011.

144. D. Schrade, R. Mueller, D. Gross, T. Utschig, V.Ya. Shur, D.C. Lupascu , Mechanics of Materials 39,161 (2007).

145. C. T. Nelson, P. Gao, J.R. Jokisaari, C. Heikes, C. Adamo, A. Melville, S. Baek, C. M. Folkman, B. Winchester, Y.J. Gu, Y.M. Liu, K. Zhang, E.G. Wang, J.Y. Li, L.-Q. Chen, C. Eom, D.G. Schlom , X.Q. Pan, Science,334, 968-971 (2011).

146. P. Gao, C.T. Nelson, J. R. Jokisaari, S. Baek, C. W. Bark, Y. Zhang, E.G. Wang, D. G. Schlom, C. Eom, X.Q. Pan, ature Communications,2, 591 (2011).

147. H. Cao, F. Bai, J.F. Li, D. D. Viehland, T. A. Lograsso, P. M. Gehring, J. Alloys Compd. 465, 244 (2008).

148. J. Boisse, H. Zapolsky, A.G. Khachaturyan, Acta Materialia 59, 2656(2011).

149. S. Guruswamy, G. Garside, C. Ren, B. Saha, M. Ramanathan, Process in crystal growth and characterization of materials. 57, 43 (2011).

150. J.J. Yao, W.W. Ge, L. Luo, J.F. Li, D. Viehland, H. Luo, Appl. Phys. Lett. 96, 222905 (2010).

151. J.J. Yao, W.W. Ge, Y.D. Yang, L. Luo, J.F. Li, D. Viehland, S. Bhattacharyya, Q.H. Zhang, and H.S. Luo, J. Appl. Phys. 108, 064114 (2010).

152. J.J. Yao, Y.D. Yang, N. Monsegue, Y.X.Li, J.F. Li, Q.H. Zhang, W.W. Ge, H.S. Luo, D. Viehland, Appl. Phys. Lett. 98, 132903 (2011).

153. J. J. Yao, L.Yan, W. W. Ge, L. Luo, J. F. Li, D. Viehland, Q.H. Zhang, H. Luo, Phys. Rev. B. 83,054107 (2011).

154. J.J. Yao, N. Monsegue, M. Murayama, W.N. Leng, W. T. Reynolds, Q.H.Zhang, H.S. Luo, J.F. Li, W.W. Ge and D. Viehland, Appl. Phys. Lett., 100, 012901 (2012).

155. J. J. Yao, W. W. Ge, L.Yan, William T. Reynolds, Jiefang Li, D. Viehland, D. A. Kiselev, A. L. Kholkin, Qinhui Zhang, and Haosu Luo, J. Appl. Phys. 111, 064109 (2012)

156. J.J. Yao, J.F. Li, D. Viehland, Y.F. Chang and G. L. Messing, Appl. Phys. Lett. 100, 132902 (2012).